

**PROTON BEAM WRITING OF MICRO/NANO  
FLUIDIC DEVICES FOR DNA ANALYSIS AND  
PARTICLE SEPARATION**

**LIU FAN**

*(B.Sc. LanZhou University)*

**A THESIS SUBMITTED  
FOR THE DEGREE OF DOCTOR OF PHILOSOPHY  
DEPARTMENT OF PHYSICS  
NATIONAL UNIVERSITY OF SINGAPORE**

**2014**



## **Declaration**

I hereby declare that this thesis is my original work and it has been written by me in its entirety. I have duly acknowledged all the sources of information which have been used in the thesis.

This thesis has also not been submitted for any degree in any university previously.



---

Liu Fan

11 February 2015

**Supervisor:** Jeroen Aton van Kan

## **Acknowledgement**

It has been a wonderful journey to me for the past four years.

Firstly, I would like to express very great appreciation to my supervisor Associate Prof Jeroen Anton van Kan. All the work was finished under his constantly support and discussion. His kindness to student and altitude to science give me a deep impression. I feel so lucky to meet such a helpful guide during my PhD career. Sincerely, thank you again.

Besides, I would like to offer my thanks to the collaborators for the help in experiment. Thanks Associate Prof Johan and Dr Zhang Ce for the help in the DNA analysis experiment. Thanks Assistant Prof Christian and Mr Jiang Li for the work in solder electrode fabrication. Thanks Mr Yao Yong, the most helpful friend, for teaching me using 20 degree beam line.

As well, I am particularly grateful for the assistance given by all the CIBA members. Thanks Dr Malar and Dr Yinghui for guiding me when I first came to CIBA. Thanks Dr Zhiya for the friendship we have built. Thanks Dr Raman, Mr Huei Ming, Mr Armin and Mr Choo for all the advice and assistance during the progress of my work. Thanks all the other CIBA members, I have enjoyed my time with all of you!

Last but not the least, I would like to express my special thanks to my parents, my brother and my love! You are all the reasons I am fighting for.

## Table of Contents

Acknowledgement .....	i
Summary.....	v
List of Tables .....	vi
List of Figures .....	vii
List of publications .....	xv
Chapter 1. Introduction.....	1
1.1 Introduction to micro and nano fluidics.....	1
1.2 The physics of micro/nano fluidics .....	3
1.2.1 Reynolds Number.....	3
1.2.2 Diffusion.....	4
1.2.3 Surface tension.....	5
1.2.4 Fluidic Resistance.....	6
1.3 Applications .....	6
1.4 Motivation for my work.....	9
1.4.1 Nanochannel fabrication for DNA analysis .....	9
1.4.2 Thermal bonding for imprinted PMMA nanochannel.....	12
1.4.3 Brownian ratchet channel for particle separation.....	15
1.5 Fabricating technology.....	17
1.6 Thesis overview .....	18
Chapter 2. Fabrication techniques.....	19
2.1 UV lithography.....	19
2.2 Electron beam lithography .....	24
2.3 Ion beam lithography .....	26
2.3.1 Focused ion beam .....	26
2.3.2 Proton beam writing .....	29
2.4 Introduction to material used in PBW .....	30
2.4.1 SU-8 resist.....	33
2.4.2 PMMA resist.....	34
2.4.3 HSQ resist.....	36
2.4.4 ma-N.....	37
2.4.5 SML.....	38
2.4.5 PDMS .....	38

2.4.6 OrmoStamp .....	39
Chapter 3. Fabrication of micro/nano fluidic devices.....	41
3.1 Proton beam writing facility .....	41
3.2 $\mu$ PG 101 laser writer.....	49
3.3 UV aligner .....	49
3.4 Plating machine .....	51
3.4 Fabrication of master mold with PBW .....	53
3.4.1 Resist mold fabrication by PBW .....	55
3.4.2 OrmoStamp mold fabrication .....	60
3.4.3 Nickel mold fabrication.....	62
3.5 PDMS casting and plasma bonding .....	65
3.6 PMMA nano imprint lithography (NIL) and bonding .....	66
Chapter 4. Nanofluidic Channels for DNA Analysis .....	69
4.1 SU-8+HSQ resist mold and DNA analysis .....	70
4.1.1 SU-8+HSQ resist mold fabrication result.....	70
4.1.2 DNA analysis with PDMS cross channels .....	78
4.2 OrmoStamp mold and PMMA nanoimprinting .....	82
4.2.1 Thin OrmoStamp mold .....	82
4.2.2 Thick OrmoStamp molds.....	85
4.2.3 PMMA nanoimprinting with OrmoStamp mold .....	87
4.3 Nickel mold and PMMA imprinting .....	89
4.3.1 Nickel mold fabrication results.....	90
4.3.2 PMMA nanoimprinting with nickel mold .....	96
4.4 Summary and future work of the nanochannel fabrication.....	97
Chapter 5. Ratchet fabrication and separation of magnetic particles .....	99
5.1 Introduction to Brownian ratchet .....	99
5.2 Brownian motion.....	102
5.3 Compact Brownian ratchet .....	104
5.4 Ratchet fabrication.....	105
5.4.1 Fabrication process .....	107
5.5 Estimation of the magnetic force .....	110
5.6 Experimental result .....	112
5.7 Summary and comparison of ratchet separation .....	125
Chapter 6. Conclusion and future work .....	127

Bibliography.....	132
-------------------	-----

## **Summary**

The fabrication of micro/nano fluidic devices has been an emerging field of research in recent years. A growing number of applications are found in biology, chemistry, and medicine such as biosensors, micro chemistry systems, drug discovery and delivery systems. Si/glass was first used in micro/nano devices fabrication due to the highly matured technique. The disadvantages for Si/glass machining are that the fabrication process is complicated and the high materials cost involved. To overcome those shortcomings, more and more attention is turning to fabricate polymer materials like polydimethylsiloxane (PDMS) through soft lithography, polymethylmethacrylate (PMMA) through nanoimprinting. In this thesis, different types of molds (resist mold, OrmoStamp mold and nickel mold) were fabricated for PDMS and PMMA fluidic devices molding with proton beam writing (PBW). The fluidic devices were further used for the study of DNA configuration using a nanochannel confinement and particle separation using a ratchet structure. PBW is a relative new 3D direct write technique. MeV proton can be focused down to sub 30 nm spot size. In PBW, protons mainly interact with the substrate electrons, the energy transfer in every collision is very small and thousands of collisions will occur before a proton comes to rest. So, proton beam writing can penetrate a photoresist very deep with minimal proximity effects. These features allow us to fabricate 3D high aspect ratio molds with smooth and vertical sidewalls by PBW.

## **List of Tables**

Table 1. 1 Bonding dimension of different method using PMMA or PC .....	15
Table 3. 1 Example for ‘emc’ file definition.....	45
Table 3. 2 Compositions of Ni electroplating solution.....	52
Table 3. 3 HSQ resist thickness with different dilution with MIBK .....	56
Table 5. 1 Comparison of gravity and magnetic force based separation.....	125

## List of Figures

Figure 1. 1 Two streams meet and diffuse in one microchannel.....	5
Figure 2. 1 UV exposure for positive and negative resist: (1) UV exposure of the photoresist with mask; (2) Chemical development for positive/negative resist ....	20
Figure 2. 2 Schematic diagram of optical shadow printing (a) Contact mode; (b) Proximity mode .....	21
Figure 2. 3 Schematic diagram of projection printing .....	23
Figure 2. 4 Relative resist thickness vs exposure dose for positive resist .....	32
Figure 2. 5 Relative resist thickness vs exposure dose for negative resist.....	32
Figure 2. 6 SU-8 molecule structure .....	34
Figure 2. 7 PMMA polymer structure.....	35
Figure 2. 8 HSQ monomer structure.....	37
Figure 2. 9 PDMS polymer structure .....	39
Figure 3. 1 Accelerator in Centre for Ion Beam applications (CIBA) (a) X/Y steerers; (b) 90° analyzing magnet; (c) Object slits; (d) Switching magnet.....	42
Figure 3. 2 Organization 10 degree beam line: (a) Collimator slit; (b) Magnetic scanning system; (c) Quadrupole focusing lenses; (d) Vacuum chamber .....	44
Figure 3. 3 scan file produce from example code .....	46
Figure 3. 4 (a) Optical image of the Ni grid; line scan is labeled at the edge of nickel edge for both X and Y directions. (b) Secondary electron collect from the line scan for X and Y directions (estimation of beam size is FWHM) .....	48
Figure 3. 5 UV aligner for micro structure fabrication .....	50
Figure 3. 6 Schematic of the RD.50 Electroplating cell: (1) Anode basket; (2) Electrolyte; (3) Spindle drive; (4) Cathode and sample holder; (5) Tunnel battle; (6) nickel pallets.....	51
Figure 3. 7 Schematic designs of nanolines (a) Straight nanolines; (b) Cross nanolines .....	53

Figure 3. 8 Schematic designs of micro structures (a) and (b) are used to align with straight configuration design; (c) and (d) are used to align with cross configuration design.....	54
Figure 3. 9 Schematic cross-section view of the PDMS micro/nano channels, DNA buffer are filled in the channels.....	55
Figure 3. 10 Fabrication process for HSQ/SU-8 resist mold (1) PBW of nanolines on HSQ resist; (2) UV alignment of microlines with nanolines on SU-8 resist; (3) final resist mold .....	56
Figure 3. 11 Thickness of HSQ dilute with MIBK (a) 220 nm thick HSQ (dilute at 1:3); (2) 100 nm thick HSQ (dilute at 1:6) .....	56
Figure 3. 12 Thickness of XR1541 (6%) spin coated at 4000 rpm for 30 s .....	57
Figure 3. 13 UV mask fabrication process with $\mu$ PG 101 laser writer .....	58
Figure 3. 14 (a) Water droplet on a plain silicon wafer (b) Water droplet on a silicon wafer coated with 0.02% Teflon solution (c) Water droplet on a silicon wafer coated with 0.04% Teflon solution .....	59
Figure 3. 15 Fabrication process for OrmoStamp mold: (1) Pour OrmoStamp and cure with UV; (2) Peel off the OrmoStamp mold from the resist mold; (3) repeat all the procedure to get the final OrmoStamp mold .....	61
Figure 3. 16 Fabrication of nickel mold using PBW and electroplating: (1) PBW and UV lithography for the resist mold; (2) Electroplating for the resist mold; (3) Peel off nickel mold and oxide with $H_2O_2$ ; (4) Plating with the nickel mold.....	63
Figure 3. 17 Schematic demonstration of PDMS casting and fabrication: (1) Fabrication of master mold by PBW or UV; (2) Pour PDMS on mold and solidify PDMS in oven; (3) Release PDMS from the mold; (4) Punch holes for inlets; (5) Treat PDMS and glass with plasma; (6) Bond the PDMS and glass together.....	66
Figure 3. 18 PMMA imprinting and bonding process: (1) Fabrication of master mold, nickel mold or OrmoStamp mold; (2) Imprint PMMA nano structures by applying high pressure and temperature; (3) Releasing the PMMA structure from mold; (4) Bonding with another PMMA thin film .....	67
Figure 3. 19 Temperature and pressure evolution with time for PMMA imprinting and bonding process: (1) before $t_1$ , increase and stable the temperature to certain value; (2) $t_1 \sim t_2$ , apply a high pressure to imprint or bond; (3) after $t_2$ , cool the sample down and release the pressure. ....	68
Figure 4. 1 DNA molecule confine in a nanochannel.....	70

Figure 4. 2 (a) Straight design nanolines fabricated on HSQ (Fox 17/MIBK at the ratio of 1:3); (b) Higher magnification of the Straight nanolines with 90 nm × 220 nm.....	71
Figure 4. 3 XR 1541 nanolines with different dosage (a) 110 nm × 220 nm with a dosage of 50 nC/mm <sup>2</sup> ; (b) 150 nm × 220 nm with a dosage of 100 nC/mm <sup>2</sup> ; (c) 170 nm × 220 nm with a dosage of 150 nC/mm <sup>2</sup> ; (d) 190 nm × 220 nm with a dosage of 200 nC/mm <sup>2</sup> .....	72
Figure 4. 4 SEM image of cross nanolines fabricated with HSQ (Fox17 dilute with MIBK for 3 times).....	73
Figure 4. 5 SEM images of cross lines with different Y & X dimension (a) 280 nm × 730 nm; (b) 250 nm × 540 nm; (c) 100 nm × 300 nm; (d) 150 nm × 250 nm .....	74
Figure 4. 6 Contrast curve change for a 850 nm thick HSQ, expose with a 2 MeV proton beam.....	75
Figure 4. 7 (a) Montage of microlines with reservoirs; (b) Optical image of four microlines aligned with nanolines; (c) Optical image of V shape microlines aligned with nanolines; (d) Schematic layout of how DNA molecules and buffer were brought into PDMS nanochannel.....	77
Figure 4. 8 (a) Montage of four microlines connect with reservoirs; (b) SEM image of the 150 nm × 250 nm nanolines .....	79
Figure 4. 9 Integrated fluorescence intensity as a function of elapsed time .....	80
Figure 4. 10 T4 DNA/1xT buffer inside 250 nm channel and flushed with 1, 3, 5 µM protamine/1×T from 150 nm channel .....	80
Figure 4. 11 DNA molecules unpacked by flushing 1 mM NaCl/1 × T buffer and different concentration of protamine (1, 3 or 5 µM) to the 250 nm DNA channels .....	82
Figure 4. 12 Resist mold and OrmoStamp copy: (a) HSQ ridge (left) and OrmoStamp channel (right); (b) PMMA channel (left) and OrmoStamp ridge (right); (c) SML channel (left) and OrmoStamp ridge (right). .....	84
Figure 4. 13 OrmoStamp copy and nickel ridge: (a) and (b) OrmoStamp ridge copy from SU8 after 2 times (c) and (d) OrmoStamp ridge copy from PMMA..	86
Figure 4. 14 (a) SEM image of a 220 nm thick HSQ master, patterned with a 2 MeV proton beam; (b) 1st generation OrmoStamp copied from the HSQ mold; (c)	

2 <sup>nd</sup> generation OrmoStamp copy; (d) PMMA imprint obtained using the 2nd generation OrmoStamp from (c) .....	88
Figure 4. 15 (a) Micro/nano PMMA bonded channels (b) Higher magnification of the bonded channel.....	89
Figure 4. 16 (a) Resist mold nanolines (ma-N 2410) connected with microlines (ma-P1240); (b) ma-N 2410 nanoline .....	90
Figure 4. 17 (a) and (b) are reverse Ni molds after first time plating .....	91
Figure 4. 18 Final nickel mold after re-electroplating (tilt 20 °).....	91
Figure 4. 19 SEM image of ma-N 2410 resist nanolines (tilt 30°).....	92
Figure 4. 20 SEM image of reverse Ni molds (a) Before oxidation with hydrogen peroxide; (b) After the oxidation process; (c) After plating process .....	93
Figure 4. 21 Resist nanoline fabricated with ma-N 2401, 180 nm × 100 nm (width × depth).....	94
Figure 4. 22 Final nickel mold after two time plating with ma-N 2401 .....	94
Figure 4. 23 SEM image of ma-N 2401 resist nanolines (tilt 30°).....	95
Figure 4. 24 (a) Optical image (dark field) of PMMA bonded nanochannels imprinted with nickel mold (b) Fluorescence image T4 DNA molecules inside the PMMA nanochannels .....	97
Figure 5. 1 Schematic depiction ratchet and pawl system: ratchet controlled by a soft elastic pawl (left) and connected to wheel paddles (right) .....	100
Figure 5. 2 DNA molecules separate by ratchet structure .....	101
Figure 5. 3 Schematic depiction of Brownian particle driven by a periodical sawtooth potential .....	103
Figure 5. 4 Schematic illustration of the channel separator .....	104
Figure 5. 5 (a) Ratchet ‘bmp’ file before tilt correction (b) Ratchet ‘bmp’ file after tilt correction.....	108
Figure 5. 6 Schematic illustration of the separation device with separation channel and two electrode channels (purple: electrode channel; red: ratchet channel) ....	108

Figure 5. 7 (a) SEM image a 10 $\mu\text{m}$ tall ratchet mold fabricated with PBW, (b) Optical image of PDMS device with solder electrodes (top view) .....	109
Figure 5. 8 (a) Optical image of the PDMS chip (b) Current applied to these two electrodes .....	112
Figure 5. 9 Current control system used to control and switch the current.....	113
Figure 5. 10 On/off voltage profile control by the labview program.....	114
Figure 5. 11 Illustration of glass slide sputtered with four Cr/Au electrodes and bonded with PDMS channels (purple: electrode channel; red: ratchet channel) .....	115
Figure 5. 12 Schematic figure of PDMS chip with one extra top PDMS channel connected with the separation channel.....	115
Figure 5. 13 Schematic describe of polymer and silica particles movement in one cycle of experiment .....	117
Figure 5. 14 Displacement of polymer particles and silica particles under $T = 50$ s, $I = 0.4$ A .....	118
Figure 5. 15 Displacement of polymer and silica particles under $T = 63$ s, $I = 0.4$ A.....	119
Figure 5. 16 Displacement of polymer and silica particles under $T = 50$ s, $I = 0.5$ A.....	120
Figure 5. 17 Displacement of polymer and silica particles under $T = 63$ s, $I = 0.5$ A.....	121
Figure 5. 18 Summary of mean displacement under different experiment conditions, from left to right (current, period): (0.34 A, 83 s); (0.4 A, 63 s); (0.4 A, 50 s); (0.4 A, 63 s); (0.5 A, 50 s); (0.5 A, 63 s); (0.5 A, 63 s) .....	122
Figure 5. 19 Comparison of the mean displacement between experimental results and calculated values .....	123
Figure 5. 20 (a) Probability distribution of silica particle without the affection of sawtooth, (b) Probability distribution of silica particle slide along the sawtooth .....	124
Figure 5. 21 Mean displacement of silica and polymer particles under a fluid drift under conditions (current, period): (0.4 A, 63 s); (0.4 A, 50 s); (0.4 A, 66 s); (0.4 A, 63 s).....	124

Figure 6. 1 Illustration of the new design for continuous separation..... 130

## List of Abbreviations

BSE	Backscattered electrons
CIBA	Center for Ion Beam Applications
CE	Capillary Electrophoresis
CEM	Channeltron Electron Multiplier
COC	Cyclic Olefin Copolymer
DOF	Depth of Focus
DNA	Deoxyribonucleic acid
DI	De-ionized
DUV	Deep Ultraviolet
EBL	Electron Beam Lithography
EUV	Extreme Ultraviolet
FCVA	Filtered Cathodic Vacuum Arc
FIB	Focused Ion Beam
FWHM	Full Width at Half Maximum
HSQ	Hydrogen Silsesquioxane
IPA	Isopropanol
IC	Integrated circuit
LMIS	liquid metal ion source
MEMS	Micro-electromechanical Systems
mRNA	Messenger Ribonucleic Acid
NIL	Nano Imprint Lithography

PBW	Proton Beam Writing
PC	Polycarbonate
PDMS	Polydimethylsiloxane
PEB	Post Exposure Bake
PMMA	Polymethyl Methacrylate
POC	Point of Care
PS	Polystyrene
RBS	Rutherford Back Scattering
RF	Radio Frequency
SE	Secondary Electrons
SEM	Scanning Electron Microscopy
STIM	Scanning Transmission Ion Microscope
TMAH	Tetramethylammonium Hydroxide
UV	Ultra Violet

## List of publications

- [1] **F. Liu**, Y. Yao, J. A. van Kan, OrmoStamp mold fabrication for DNA micro/nano fluidics applications, *Nuclear Instruments & Methods in Physics Research Section B*, DOI 10.1016/j.nimb.2015.01.067.
- [2] **Fan Liu**, Kheng Boon Tan, P. Malar, S.K. Bikkarolla, J. A. van Kan, Fabrication of nickel molds using proton beam writing for micro/nano fluidic devices, *Microelectronic Engineering*, 102 (2013) 36-39
- [3] Ce Zhang, Kai Jiang, **Fan Liu**, Patrick S. Doyle, J. A. van Kan, and Johan, R. C. van der Maarel, A nanofluidic device for single molecule studies with in situ control of environmental solution conditions, *Lab on Chip*, 13 (2013) 2821-2826
- [4] Ce Zhang, Durgaraao Guttula, **Fan Liu**, Piravi P. Malar, Siow Yee Ng, Liang Dai, Patrick S. Doyle, J. A. van Kan, and Johan R.C. van der Maarel, Effect of H-NS on the elongation and compaction of single DNA molecules in a nanospace, *Soft Matter*, 9 (2013) 9593-9601

# **Chapter 1. Introduction**

In this chapter, micro/nano fluidics and its applications in different areas are briefly introduced in the first place. Following that, the main topics of this thesis will be explained. Firstly, I will discuss several types of molds for nanochannel fabrication. Secondly, I will introduce PMMA thermal bonding for DNA analysis. Finally, I will present a ratchet structure for particle separation.

## **1.1 Introduction to micro and nano fluidics**

When Richard Feynman first give a talk about “There is plenty of room at the bottom!”, in 1959, people started to look at things at micro and nano scale [1]. In the late 1980s, with the development of integrated circuit (IC) fabrication process, micro-electromechanical systems (MEMS) technology emerged [2]. Remarkable progress has been achieved in MEMS since then due to strong support of governments and industries. MEMS make the system faster, cheaper, more reliable, and capable of integrating more complex function. The experience gained from this development has led to applications in various fields such as microfluidics, aerospace, biomedical, chemical analysis, communication, data storage, and so on [3, 4]. Microfluidics or lab on chip has gained a great deal of interests in potential applications’ market in the last twenty years and is one of the fast growing areas in MEMS [5, 6, 7, 8, 9].

Micro/nano fluidics, originates from micro-electro-mechanical-systems (MEMS) technologies, it deals with the study of behavior, handing, and analysis of fluids at

micro/nano scale. Micro/nano fluidics is a combination of many different disciplines such as biology, physics of fluids, chemistry, micro/nano engineering, and so on [10]. The ideal dream for this micro/nano fluidics science is to integrate many different laboratory functions into one single lab-on-chip [11]. Recently, micro/nano fluidics have received more and more interest and attention, as we can see lots of work has been done in this area [12, 13, 14, 15]. The increasing interest is due to the availability of micro- and nanotechnologies allowing mass production of well-defined structure [16]. Micro/nano fluidics has opened a new way for chemical analysis, as well as discovery of medicine [17, 18 , 19]. Compared to conventional large-scale systems, micro/nano fluidics has several advantages in biological and chemical analysis. One of the most obvious advantages is reduced reagent consumption. It becomes appealing for many of the biological applications where the reagents are expensive (e.g. antibodies), or where the quantity of the sample volumes are limited [20]. Another appealing aspect is that it is able to carry out separation and detection with high resolution and sensitivity [21]. Thirdly, the small size and large integration of different functionalities make micro/nanofluidics a portable analytical technology. Lastly, the fluid stream will be always laminar due to the size of micro/nano fluidics [22, 23]. So, fluids can be accurately controlled and predicted. One consequence of laminar flow is that two streams flowing in contact will mix only by diffusion. This has been widely used for performing assays and sorting particles [24,25].

## 1.2 The physics of micro/nano fluidics

In order to gain a better understanding of micro/nano fluidics, we need to understand the physical phenomena that dominate this regime. At micro/nano scale, the forces that dominate are different from those that we experience in daily life [26]. At these scales, viscous force becomes more and more important, turbulence is nonexistent. Characteristics like diffusion, fluidic resistance, surface to volume ratio and surface tension play a major role [27]. Those differences compared to the macro scale give micro/nano fluidics its unique new features, advantages as well as some disadvantages.

### 1.2.1 Reynolds Number

The Reynolds number ( $Re$ ) determines whether the flow in a channel is in the laminar or turbulent flow regime. It is defined as the ratio of inertial forces to viscous forces and quantifies the relative importance of these two types of force in a fluid. The Reynolds number can be calculated by:

$$Re = \rho v D_h / \mu \quad (1.1)$$

Where  $\rho$ ,  $v$ ,  $D_h$  and  $\mu$  are the fluid density, characteristic fluid speed, channel diameter and fluid viscosity respectively. At low Reynolds number ( $Re < 2300$ ), viscous force plays an important role. It generally indicates a laminar flow which means the velocity of a particle in a fluid stream can be easily predicted. For micro/nano fluidics system, a typical fluid speed of  $10 \sim 100 \text{ } \mu\text{m/s}$  and channel size of  $10 \text{ } \mu\text{m}$  will give a  $Re = 10^{-3}$ . This means that for micro/nano fluidic systems, the flow will always be laminar. One disadvantage for laminar flow is that mixing

of two streams will happen at the interface area by diffusive effect. This provides a challenging task producing a homogenous flow. Therefore, mixing at the microscale should always aim to maximize the interface to allow fast diffusion [28]. At the high Reynolds number ( $Re > 4000$ ), inertial force tends to play an important role. The flow is considered to be turbulent, chaotic and unpredictable. As  $Re$  is between  $2300 \sim 4000$ , laminar and turbulent flows are both possible and are called transition flow.

### 1.2.2 Diffusion

Diffusion is a process in which particles or ions with higher concentration diffuse to areas with lower concentration undergo Brownian motion. Figure 1.1 shows two streams flowing into one micro channel and diffuse along this channel. Diffusion can be simplified as  $\langle d^2 \rangle = 2Dt$  in one dimension [27], where  $d$  is the mean square displacement (MSD),  $D$  and  $t$  are the diffusion coefficient and time respectively. Diffusion can be neglected for particle/ion movement at macroscale. In a dilute aqueous solution, the diffusion coefficients of most ions are similar and have values around  $10^{-5} \text{ cm}^2\text{s}^{-1}$  at room temperature [29]. It takes around  $10^4$  s to diffuse 1 cm while less than 1 s to diffuse 10  $\mu\text{m}$ . Diffusion is widely applied in microfluidics for particle or biomolecule separation. Particles with different size tend to diffuse with different speed. One idea is to use a ratchet structure to drive particles in one direction and particles with different size can be separated because of the different driving speed [89].

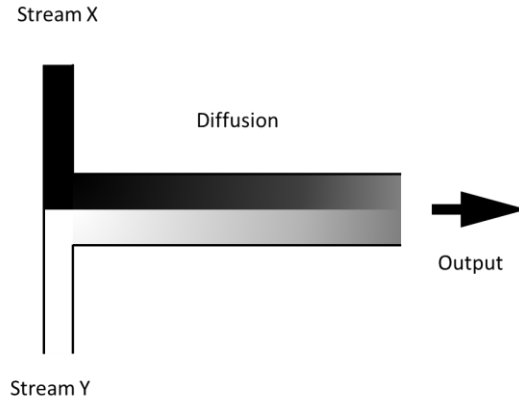


Figure 1. 1 Two streams meet and diffuse in one microchannel

### 1.2.3 Surface tension

Surface tension is the result of cohesion of liquid molecules at a liquid/gas interface. At the interface, the attraction of water molecules to each other is bigger than to the molecules in the air. So, it causes the water surface to behave like a stretched elastic membrane. Surface tension is significant at capillary length scale (around 2 mm for water and air at room temperature and standard pressure) and below. As an example, a water spider can stand on top of water surface because the surface tension is big enough to support its weight. Capillary action is another example of surface tension. There it is not only the interaction of liquid/air interface, but also the interface of liquid/container. As a consequence, liquid is able to draw up in a narrow capillary tube against external force like gravity. The height of a liquid column is given by [30]:

$$h = \frac{2\gamma \cos\theta}{\rho g r} \quad (1.2)$$

where  $\gamma$ ,  $\theta$ ,  $\rho$ ,  $g$ , and  $r$  are liquid/air surface tension, contact angle, density of liquid, local acceleration of gravity, radius of the tube.

It may not be so obvious for this phenomenon at large dimension. For a glass tube with a diameter of 4 cm, the water lever would just rise about 0.7 mm according to equation 1.2. While for a glass tube with diameter of 400  $\mu\text{m}$ , the water lever would rise about 70 mm. And it has been widely used for capillary electrophoresis (CE) for chemical analysis [31]. CE made it possible to achieve high sensitivity and high resolution for mass spectrometry with small amount of sample [32].

#### **1.2.4 Fluidic Resistance**

For the fluids inside a tube, the fluidic resistance is defined as  $R=\Delta P/Q$ , while  $\Delta P$  is the pressure difference and  $Q$  is the flow rate. For a laminar flow, the fluidic resistance can be easily calculated with equation 1.2. Circular tube is the most common geometry used, because of its presence in blood transport. The resistance of a circular channel can be calculated using the formula [27]

$$R = 8\mu L/\pi r^4 \quad (1.3)$$

Where  $\mu$  is fluid viscosity,  $L$  is the channel length, and  $r$  is the channel radius. We can see that the resistance is greatly affected by the channel diameter. It will increase rapidly when the diameter goes down. This is consistent with the fact that the viscous force plays a major role at micro/nano scale.

### **1.3 Applications**

Micro/nano fluidics has plenty of applications in different disciplines, like biology (*cell/DNA manipulation and analysis, biosensor*), chemistry (*micro chemical systems*) and medicine (*drug discovery and delivery systems*). Some of the

applications are widely used in our daily life. One of the most successful products is the inkjet nozzle for printers. Invented in 1979 by Hewlett-Packard, inkjet printers use a series of nozzles fabricated with silicon to spray ink droplets on paper or another medium. And the idea is still used by companies like Canon and Epson nowadays.

Another application that shows great potential for micro fluidics is the point-of-care (POC) diagnostic device. POC enables disease diagnostics faster and easier for the patient even without the need to go to hospital. One of the most successful examples of POC diagnostics using microfluidic device is the iSTAT device [33]. The iSTAT device is lightweight with a portable size allowing patient-side blood testing. It consists of a disposable silicon thin-film electrode for detection of blood chemistries (sodium, potassium, chloride, glucose, and gases), coagulation and cardiac markers. As well, very small sample amount (~ 65 to 100  $\mu$ L) and no pretreatment are needed for the iSTAT analyzer. Testing result can be accessed in just few minutes, which allows us to make fast treatment decisions.

Conventional bioanalytical technology relies mostly on the measurement of large group of cells [34]. For example, mRNA (messenger ribonucleic acid) is extracted from a large number of cells (typically  $10^7$  cells) during transcription profiling. This can give average information (genetic contents, length distribution) of the whole population. The information of individual cell/DNA (Deoxyribonucleic acid) can't be discerned.

It is not easy to manipulate a single cell or single biomolecule using conventional technology. Recent advance in micro/nano technology makes it possible to

fabricate structures at micro/nano dimension that can directly interact with single cells and DNA molecule. Devices can easily be made on these length scales, thus enabling manipulation and analysis of biomolecules for cell biology, clinical research, and gene sequencing applications [ 35 , 36 , 37 ]. The cellular/DNA environment can be precisely controlled with micro/nano fluidic technology. It is also possible to fabricate a parallel group of the same structures that can analyze multiple cells or DNA molecules at the same time [38, 19]. Micro/nano fluidics will help to gain a better understanding for those fundamental processes in biology that occur at tens of micrometer to tens of nanometer scale, such as information storage, transcription and translation [39].

Various cell manipulation techniques for cell focusing, trapping, separation have been investigated based on different types of force used. Optical tweezers were used to sort yeast cells and human embryonic stem cells by Wang *et al* [40]. The cells were detected and recognized through key characteristics eg size and fluorescence, employing a digital imaging system. The cells were deflected away from the original flow by optical tweezers. This cell sorter exhibits very high accuracy and causes less damage to the cells. Magnetic force was also used for cell manipulation, called magnetic-activated cell sorting (MACS). The cells were labeled with magnetic nanoparticles conjugated with antibodies [ 41 ]. The dielectrophoretic technique is another way of manipulating cells. The moving speed depends on the magnitude of electrical charge of cells and mostly depends on their size. It has been used for the clinical cell separations. Report shows that circulating tumor cells and malignant cancer cells could be isolated from

heterogeneous blood sample [42, 43]. Few other applications such as observing cell behavior and response under physical chemical stimulation were also investigated by Eriksson *et al* [44].

DNA is a linear molecule and a huge amount of information is organized linearly along the DNA (length, sequence, epigenetic and genetic modifications). It is extremely important for medical applications because genetic contents are the underlying factor for many diseases [45]. With micro/nano fluidic techniques, we can purify, separate and even visualize the length of a single DNA molecule. Different work has been performed for the analysis of DNA molecules using micro/nano fabricated structure. Dekker *et al* [46] used a biological nanopore ( $\alpha$ -haemolysin) for the single stranded DNA translocation. By monitoring the current difference when DNA passes a nanopore, it can give some information about the sequence of the DNA molecule. They also came up with an experiment, using solid-state nanopores fabricated on Si for RNA unfolding.

## 1.4 Motivation for my work

### 1.4.1 Nanochannel fabrication for DNA analysis

In my thesis, the first topic we focus on is the nanochannel fabrication for DNA analysis. Si/glass was first introduced for micro/nano fluidic device fabrication due to the highly matured fabrication technology [ 47 , 48 , 49 ]. Usually, UV/electron beam lithography is used to define structure on a sacrificial resist layer. And reactive ion etch or chemical etch is conducted to pattern the

silicon/glass substrate. Finally, the structure is bonded with SiO<sub>2</sub>/glass to seal the structure. A typical bonding using high voltage or temperature can provide a rigid seal. One problem is that the surface of the bonding structure needed to be defect free. So, other bonding processes were optimized such as by anisotropic sputtering the silicon nanochannel with SiO<sub>2</sub> or by thermal oxidation [50, 51]. The enclosed channel can be as small as 10 nm. The advantages for Si/glass structures are high resolution, robust, compatible with organic solvent and high bonding strength. The disadvantages are the fabrication process is complicated and the materials cost is relatively high. To overcome those shortcomings, more and more attention is turning to polymer materials like polydimethylsiloxane (PDMS), polymethylmethacrylate (PMMA) and polycarbonate (PC) by using soft lithography and thermal imprint lithography. Since the introduction of PDMS casting by Xia & Whitesides in late 1990s [52], PDMS has been extensively used in micro/nano fluidic applications [53 ,54]. PDMS is becoming more and more important, not only because of the simplicity of the fabrication process but also because of the flexibility PDMS offers over other polymer materials. PDMS was chosen for manufacturing micro/nano fluidic devices for the following reasons. (1) PDMS is transparent at optical wavelength (240 nm ~ 1100 nm), this allows optical microscopy to be used in biological experiments. (2) PDMS has a low auto fluorescence [55] and is biocompatible. (3) Two pieces of PDMS can be easily bonded together, facilitating multilayer device fabrication. (4) PDMS is deformable, which allows PDMS to serve as a microfluidic valve to control the flow [56]. (5) A PDMS device is inexpensive, easy to fabricate and relatively high

resolution. PDMS with dimension around 100 nm channels have been widely used for DNA analysis in CIBA [57]. One disadvantage for PDMS is its low Youngs' modulus. This makes it challenging to replicate PDMS structures below 1 micron, especially when trying to fabricate sub 100 nm details in PDMS. A hard PDMS material with much higher price was reported to be able to copy structures with dimension around 20 nm [58].

A harder material like PMMA is another alternative for micro/nano fluidic devices fabrication. PMMA is a widely used thermoplastic that exhibit softening behavior at around its glass temperature ( $T_g$ ), and return to solid state after cooling down. The cost of PMMA polymer is much less than silicon/glass based chips. PMMA devices can be rapidly fabricated by using NIL and the surface can be easily modified for particular reagent molecules. PMMA also exhibits very high optical transmission at both visible and ultraviolet (UV >250 nm) wavelength. The low cost and easy fabrication make PMMA very popular for micro/nano fluidic devices fabrication [59]. Compared with traditional material such as silicon and glass, PDMS and PMMA offer both lower materials and lower manufacturing costs. So these two materials are mainly used in our experiments and tests. Micro/nano fluidic chips will get easily contaminated during experiments, requiring new samples for next experiment testing. Therefore, a high throughput fabrication technology is important for micro/nano fluidic development [60]. Nano imprint lithography and PDMS soft lithography are two promising technologies that can fabricate structures with high resolution and throughput.

To perform PDMS casting and PMMA nanoimprinting, a high quality master mold is needed. The mold can be a Si/SiO<sub>2</sub>, polymer or metal mold, depending on the requirement. In our experiment, resist molds (HSQ & SU-8), hybrid polymer mold (OrmoStamp) and metal mold (nickel) were fabricated for either PDMS casting or PMMA nanoimprinting. These PDMS and PMMA LOC devices were used by our collaborators for single DNA experiments.

#### **1.4.2 Thermal bonding for imprinted PMMA nanochannel**

Sealing of micro/nano fluidic devices is a critical step for thermoplastic based devices to form enclosed structures. Unlike silicon and glass, thermoplastics open an extensive way of substrate bonding options as well as the unique challenges to achieve optimal bonding result due to the material properties.

There are two types of bonding process for thermoplastics micro/nano fluidic devices, indirect bonding and direct bonding. Indirect bonding involves the use of an adhesive layer to seal two substrates, while direct bonding seals those two substrates without any interface layer.

The indirect adhesive bonding is widely used because of the simple bonding process. A UV curable liquid adhesive is filled between two substrates and cured by UV irradiation [61]. A big concern using this method is deformation and clogging of microchannels. Few ways have been investigated to control and guide the adhesive layer [62, 63]. Using the UV curable adhesive bonding, PMMA channels with a few hundred of micron dimension can be fabricated. Another indirect bonding process is done via lamination of a thin film. This is attractive

also because of the simple bonding process and suitability for mass production.

Lamination films are commercially available with tens of micron thickness. Two types of lamination films, pressure sensitive film and thermal-activated film, are usually used to seal thermoplastic microfluidics. Structures down to tens of micron dimension can be achieved for PMMA or PC bonding [64, 65].

For the direct bonding, several ways like thermal fusion bonding, solvent bonding, and surface treatment/modification have been investigated [ 66, 67 ]. During thermal fusion bonding process, the thermoplastics are heated above or near the  $T_g$ , while applying a uniform pressure to increase the contact of two polymer layers. Thermal bonding is widely used because of its simple process, homogenous surface properties when using identical material, and relatively high bond strength. Different materials including PMMA, PC, and COC (Cyclic olefin copolymer) have been bonded successfully by different groups [68, 69, 70, 71]. One of the biggest challenges in thermal bonding is channel collapse because of the high temperature and pressure used during bonding. So for bonding temperature above  $T_g$ , a low bonding pressure is preferred to prevent structure collapse [72]. By properly optimizing the temperature and pressure, cross sections of few hundred nanometer have been reported in thermal bonded PMMA channels [73, 74]. Pressure uniformity is a very critical factor to get a uniform bonded chip. To get a better control of temperature, pressure and bonding time, a programmable hot press is generally preferred for the thermal bonding process. Another direct bonding process can be achieved via increasing the surface energy of polymer, which will in turn increase the polymer bonding strength. Several

methods to increase the surface energy have been reported by using acid treatments, UV or UV/ozone exposure and plasma treatment [75, 78, 79]. Plasma treatment is commonly used for PDMS microfluidic device bonding. Silanol groups will be generated at PDMS surface by energetic ions, electrons and UV photons during plasma treatment [76]. Covalent and hydrogen bonds can be formed at the interface to enhance the bond strength [59]. This technique has been widely used for thermoplastics based microfluidics as well. Research performed by Johansson *et al* shows that the plasma treatment can greatly reduce water contact angle for commonly used plastics, such as PMMA, PC and PS [77]. Other works show that plasma activation is able to reduce the bonding temperature as well as increase the bond strength for PMMA, PC, COC, and PS [78, 79, 80, 81].

Bhattacharyya *et al* reported that the bonding strength of COC and PS can be enhanced by two to three orders by 10 W air plasma treatment [82].

Another way to increase the surface energy is to expose the polymer with UV or UV/ozone to create photo-oxidation and scission of polymer chains. One work done by Truckenmuller *et al* shows that the glass temperature ( $T_g$ ) of the UV exposed PMMA is reduced by 60 K as a result of polymer scission [83]. In their experiment, around 3  $\mu\text{m}$  PMMA top layer was exposed through UV irradiation (248 nm). This is unacceptable when dealing with nanochannels. The thickness of the surface layer can be further controlled by the irradiation dose, spectrum of UV radiation and incidence angle of radiation. The thickness might be further adjusted to nano dimensions. In general, plasma treatment, UV or UV/ozone can significantly improve the bond strength and reduce channel collapse by

controlling the bonding temperature.

Most of the work on thermoplastics polymer bonding was done at tens of microns, few studies were carried out at around 200 nm or even smaller feature size (table 1.1). In our experiment, PMMA was chosen as candidate to imprint with nanochannels fabrication. The bonding process was optimized by adjusting the bonding temperature, pressure, and surface plasma activation. DNA analysis was also conducted test with the nanochannels.

Table 1. 1 Bonding dimension of different method using PMMA or PC

Method	Material	Dimension (width × depth)
UV-curable adhesive bonding	PMMA	250 μm × 100 μm [63]
Laminate film bonding	PC	70 μm × 40 μm [65]
Thermal bonding	PMMA	2 μm × 0.2 μm [74]
Plasma/UV bonding	PMMA	200 μm × 20 μm [83]

#### 1.4.3 Brownian ratchet channel for particle separation

The separation of DNA fragments and proteins play a central role in molecular biology. Separation of DNA by size is at the heart of genome mapping and sequencing and is likely to play an increasing role in diagnostics [ 84 ]. Gel electrophoresis is a traditional simple way of separating DNA and proteins [ 85, 86, 87 ]. Gels like agarose, agar and polyacrylamide are polymers consisting of different size of nanopores. By applying an electric field, DNA molecules or proteins with different size will move with different speeds through the nanopores. The disadvantage of gel electrophoresis is that the gel will generate heat during

the process. Separation of chromosome-size DNA will take days by using pulsed-field gel electrophoresis.

With the help of micro/nano fabrication technology, people can fabricate micro/nano structures used for particle separation very easily. Huang *et al* [88] fabricated a DNA prism (approximately 3 mm × 9 mm) used for relatively large size DNA separation (from 61 to 209 kilobases). The design consists of an array of 2 μm size pillars with 2 μm space from each other. In their experiment, two electric fields were switched alternatively. That is a stronger electric field is applied diagonally, and a smaller electric field is applied horizontally. DNA molecules with different length were separated in less than a minute using this design.

A ratchet structure was first used as a particle motor. It was shown that particles subjected to an asymmetric potential or spatial structure (zigzag structure) can be driven in a specific direction [89]. The driving speed depends on parameters like diffusion coefficient, viscosity of the buffer and diffusion time. So the ratchet structure (3 cm × 4 cm) was also applied to separate biomolecules, such as DNA molecules [90]. Separation methods like gel electrophoresis, DNA prism and ratchet structure carry a chip dimension from tens of centimeters for Gel electrophoresis to millimeters for DNA prism and ratchet structures. To integrate a separator on a lab on chip device, a smaller and compacter ratchet separation design was introduced by Simon *et al* for micro particle separation [91]. The device dimension (500 μm × 200 μm) is about one order of magnitude smaller compared with the smallest separator (DNA prism). This is a great advantage over

the other separation methods in chip dimension. In Simon's experiment, gravity was used to drive the micro beads which is time consuming and complicated to operate. To improve this ratchet design with a better performance, a stronger force using a magnetic field will be used in our experiment for particle separation. A two time smaller ratchet design will be fabricated with proton beam writing (PBW) for smaller particle separation.

## 1.5 Fabricating technology

Electron beam lithography (EBL), focused ion beam lithography (FIB) and UV lithography are commonly used micro/nano fabrication technologies. In our experiments, a relative new fabrication technology proton beam writing (PBW) was used to fabricate high quality master molds for PDMS and PMMA fluidic devices. Usually MeV protons are focused to a sub 100 nm beam spot and used for fabricating structure on resist or silicon [92]. Proton beam writing offers some interesting and unique advantages compared with EBL and FIB. In PBW, the protons mainly interact with the substrate electrons and penetrate almost in a straight path except at the end of range. Since the mass of a proton is about 1800 times larger than the mass of an electron, the energy transfer in every collision is very small and thousands of collisions will occur before a proton comes to rest. So, proton beam writing can penetrate a photoresist very deep with minimal proximity effects and maintain an even energy deposition along the proton path. These features allow us to fabricate 3D high aspect ratio molds with smooth and vertical sidewalls by PBW [93]. PBW and other fabrication technologies will be

discussed in more detail in the second chapter.

## 1.6 Thesis overview

**Chapter 2** compares different fabrication techniques for micro/nano fluidics. UV, electron beam lithography, focused ion beam, and proton beam writing will be briefly introduced. Another topic in this chapter will talk about the materials used for micro/nano fluidics.

**Chapter 3** discusses the facilities of PBW in the Center for Ion Beam Applications. The fabrication process for different molds (resist mold, OrmoStamp mold and nickel mold) with PBW will be discussed in detail. PDMS casting and nano imprint lithography for micro/nano fluidic devices fabrication will be discussed as well.

**Chapter 4** discusses the fabrication and characterization result for PDMS and PMMA nanochannels. The fabrication results for resist mold, nickel mold and OrmoStamp mold will be shown in the first place. Further, the characterization for PDMS crosschannels with DNA analysis will be presented. Another topic is the fabrication results of PMMA nanochannels with nickel and OrmoStamp molds.

**Chapter 5** presents the particle separation using Brownian ratchet. We will first give a brief description of the ratchet design and show the fundamental theory of separating particles with this design. Following that, fabrication result with PBW and characterization with micro particles will be presented.

**Chapter 6** gives a general discussion of all the research projects and the future work.

## **Chapter 2. Fabrication techniques**

In this chapter, I will give a brief comparison of few technologies that are used for fabricating micro/nano fluidic devices. UV lithography, electron beam lithography, and ion beam lithography (focus ion beam, Proton beam) will be discussed because they are widely used for micro/nano fluidics fabrication. Following that, different photoresists (ma-N, ma-P, SU8, PMMA and HSQ resist) and other material (PDMS, OrmoStamp) that were used in our experiment will also be covered.

### **2.1 UV lithography**

UV (ultraviolet) lithography, or optical lithography, is the most commonly used photolithography technique today [94]. The main advantage of UV lithography is high throughput, which allows economical mass production and is suitable for large area fabrication. The wavelength of UV light ranges from 13.4 nm for extreme UV to 436 nm for g-line, corresponding to photon energies approximately from 91.8 eV to 2.8 eV. During the fabrication, a pattern from a photomask is transferred to light sensitive photoresist (see fig 2.1). The reaction of UV light with photoresist is through photoelectric effect with inner or outer atomic electrons, which depends on the energy of UV light [95]. Electrons generated by photoelectric effect will cut or crosslink polymer chains in the photoresist. After chemical development, the exposed photoresist will be removed for positive photoresist or remain for negative resist. The fabrication process for UV lithography is shown in fig 2.1.

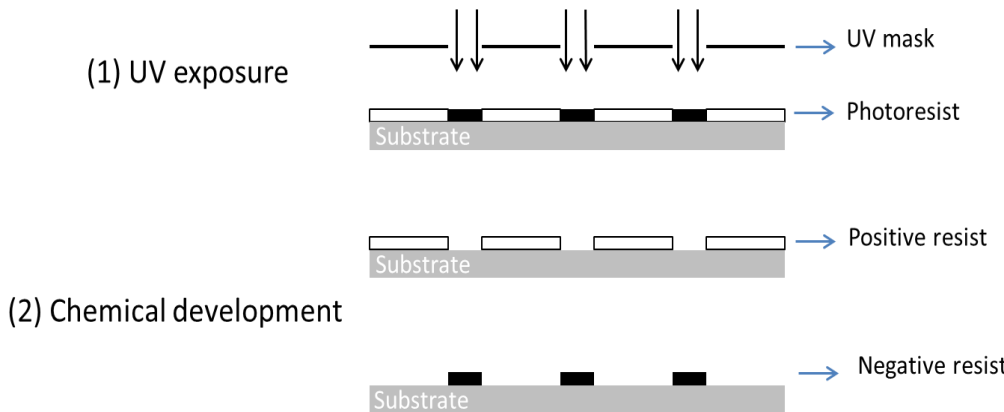


Figure 2. 1 UV exposure for positive and negative resist: (1) UV exposure of the photoresist with mask; (2) Chemical development for positive/negative resist

The mask is typically commercially available and consists of a substrate covered by a thin Cr film (around 100 nm). The substrate can be soda lime glass for typical UV light generated by Hg lamps or quartz for deep ultraviolet (DUV) generated by excimer light source. This is because soda lime has a poor transparency to DUV. The Cr layer is patterned to selectively block the UV light. The glass serves as a substrate for the Cr pattern and should have a good transparency to UV light. In such case, the pattern on the Cr layer will be transferred to the photoresist. There are two different ways for the optical exposure methods: shadow printing and projection printing. For shadow printing, contact mode and proximity mode are included (see fig 2.2). It is just like transferring the shadow of a pattern on the mask to the photoresist sample. Contact and proximity mode are usually used by most laboratories because of the simple fabrication process. For contact mode, the mask is in contact with the surface during the exposure. One disadvantage is that dust particles on sample can be embedded into the mask and cause damage or contaminate the UV mask. To

minimize mask damage, proximity exposure is used. The proximity mode is similar to contact except there is a small gap (10 - 50  $\mu\text{m}$ ) between mask and sample. The small gap will degrade the resolution caused by optical diffraction at mask's feature edges. In shadow printing, the critical dimension (CD) or the minimum line width can be calculated approximately by the following equation.

$$\text{CD} \sim \sqrt{\lambda g} \quad (2.1)$$

Here  $\lambda$  is the wavelength of UV light,  $g$  is the gap between UV mask and sample. For a deep UV spectrum around 250 nm and gap of 10  $\mu\text{m}$ , the CD will be around 1.6  $\mu\text{m}$ .

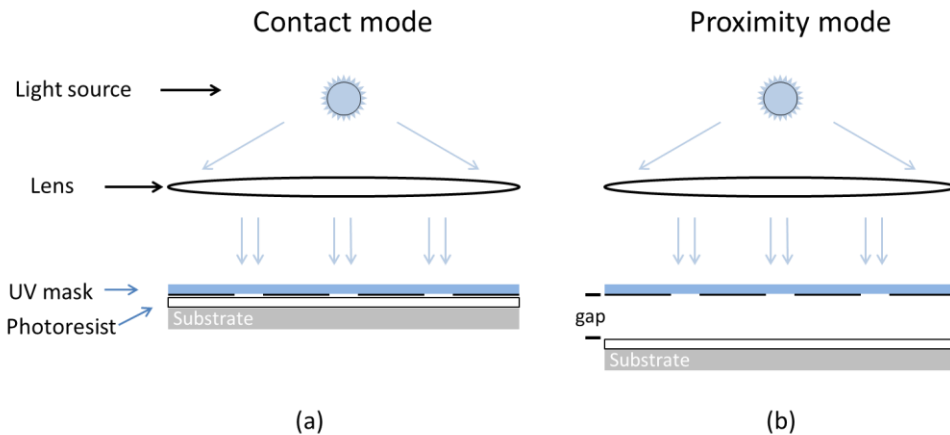


Figure 2. 2 Schematic diagram of optical shadow printing (a) Contact mode; (b) Proximity mode

To avoid mask damage and increase features resolution, projection mode has been developed by placing a group of projection lenses in between the mask and resist sample (see fig 2.3). A simple metaphor of the projection mode is photography process, light of an object passes through a lens and forms an image on a screen. So the object and image ratio can be adjust by the moving the lens in between. The resolution of a projection system can be calculate by the Rayleigh equation.

$$HP = k_1 \frac{\lambda}{NA} \quad (2.2)$$

Where  $HP$  is the half-pitch or critical dimension of periodical structures,  $k_1$  is a parameter determined by illumination conditions (usually around 0.4),  $\lambda$  is the wavelength of light, and  $NA$  is the numerical aperture. The numerical aperture is related to the refractive index of the medium and angle of the converging beam to the sample.

$$NA = n \sin \theta \quad (2.3)$$

Equation 2.2 shows that resolution of the projection system can be increased either by reducing the wavelength or increasing  $NA$ .

Another parameter that is important for projection printing is the depth of focus (DOF). It describes the range of lengths for which the image is in focus on the sample. The depth of focus can be expressed as:

$$DOF = k_2 \frac{\lambda}{(NA)^2} \quad (2.4)$$

To fabricate structures on thick resist, a large DOF is preferred to achieve a uniform resolution from the top to bottom of the resist. And this can be achieved by either increasing the wavelength or reducing the numerical aperture.

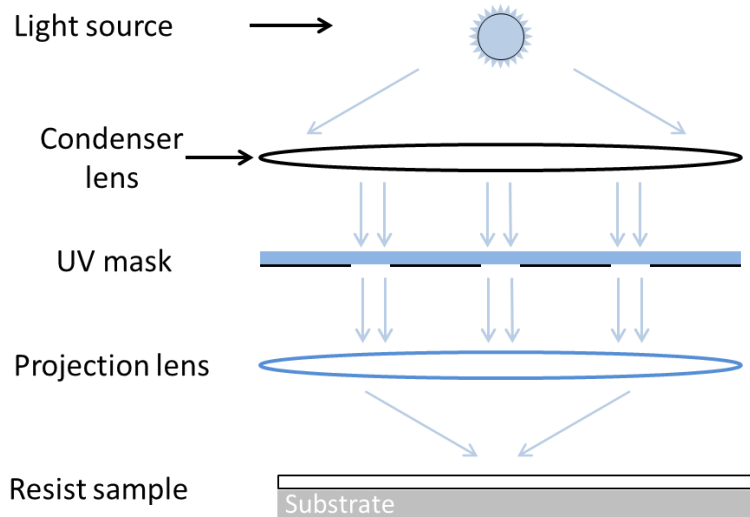


Figure 2.3 Schematic diagram of projection printing

Until the late 1980s, high power mercury lamps had been mainly used in lithography for their spectral lines at first 436 nm (“g-line”), then 405 nm (“h-line”), and finally 365 nm (“i-line”). With the need for higher resolution and throughput in semiconductor industry, excimer laser lithography was proposed and demonstrated at IBM by Kanti Jain [96]. The krypton fluoride ( $\text{KrF}_2$ , 248 nm) excimer lasers were first used and then upgraded to argon fluoride ( $\text{ArF}$ , 193 nm). Excimer laser lithography has played a major role in the last 20 years [97]. With the help of 193-nm lithography, a 65 nm processor was realized by Intel in 2006. To get a better resolution, it is natural to consider the 157 nm molecular fluorine lasers. The problems for introducing 157-nm lithography were it was too slow to develop suitable pellicles (thin membranes to protect photomask) and the cost of lens material was too high [98, 99, 100]. Luckily, a new technology was developed that is liquid-immersion lithography. In this liquid-immersion lithography, a fluid is introduced between the last optical element and photoresist.

By adding high purity water, the refractive index can increase from 1.0 to 1.44 [101]. By 2010, the 32 nm half-pitch processor became available on the market by using liquid-immersion lithography. In 2012, 22 nm half-pitch processor was realized by using liquid-immersion lithography and double patterning. During the last 20 years, the minimum feature size for UV lithography has shrunk from 500 nm in 1990 to 22 nm in 2012. In the future, 13.4-nm lithography will succeed as extreme ultraviolet (EUV).

## 2.2 Electron beam lithography

Optical lithography is widely used by researchers in the lab because of the high throughput, good resolution, low cost, and easy operation. However, UV lithography is not suitable for thick resist fabrication when resolution is very high (see equation 2.2 and 2.4). Due to deep sub micrometer IC process requirements, electron beam lithography (EBL) serves as an alternative for optical lithography to fabricate high aspect ratio nanometers features. Electron beam lithography is a nanofabrication technique in which a focused electron beam exposes a resist in a direct write manner, 4.5 nm wide structures have been achieved by Yang *et al* [102]. Electron beam (typical energy of 20 keV) has a much smaller de Broglie wavelength compared to UV light (equation 2.3).

$$\lambda = \frac{h}{\sqrt{2meU}} \quad (2.3)$$

According to equation 2.3, the wavelength of a 20 keV electron is around 0.062 nm. So, there is practically no diffraction limit for electron beam as a lithography methodology. The advantages of EBL include very high resolution, highly

automated and precisely controlled operation, as well as suitability for relatively thick resist fabrication. With electron beam lithography, dense grating lines down to 10 nm can be fabricated in a 250 nm HSQ [103]. For a 2  $\mu$ m thick SML resist, 200 nm structures can be fabricated with an aspect ratio of 10 [104]. For commercial EBL systems, the beam spot can be easily focused down to a few nanometers [105, 106]. However, it is not so easy to write such a small structure especially for thick resist or high density features. This is because various type of radiation, such as secondary electrons (SE) and backscatter electrons (BSE), will be generated when an electron beam strikes a specimen. The SE possess very high energy that can penetrate the sample with a range of 10 to 100 nm [107]. Even higher energy BSE contribute to backscatter events and will expose the resist as well. The resulting region over which the incident electrons interact with the sample is known as pear shape interaction volume. The resolution of electron beam is greatly limited by this proximity effect. The proximity effect is more obvious for thick resist layers, effectively making electron beam lithography a two dimensional process and therefore not suitable for 3D fabrication.

The major disadvantage for EBL is its low throughput. For a commonly used direct writing EBL system, the focused beam is scanned on wafer one pixel at a time. This imposes a limitation on the exposure speed to be transferred onto the wafer. Other projection EBL system such as SCSLPEL and PREVAIL were developed to meet the need of higher throughput in 1990s by Bell Laboratories and IBM respectively [108, 109]. Both concepts project a shaped beam on a small field image of a 4 times mask onto wafer. Those projection systems make a

compromise between pattern flexibility with pattern writing speed, and are efficient in the exposure of repetitive patterns. However, special requirement for the membrane mask and other issues like space charge limitation, stitching a great number of sub patterns into a single overall pattern and excessive thermal absorption eventually prevented the projection EBL from being a practical tool for nanofabrication [110, 111]. Apart from projection EBL system, another attempt such as parallel beams was also largely investigated recently by different company such as Advantest, IMS Nanofabrication, and Mapper Lithography [112, 113, 114]. The idea is to integrate a large number of multi electron beams (MEB) into a system to realize high enough throughput. Various applications have been realized with MEB such as mask writing, prototyping, writing critical layers in high volume manufacturing [115]. The single beam system is now under a great pressure of Moore's Law for mask writing. The writing time for most recent advanced nodes can be days. With a multi electron beams, the time can reduce to hours [116].

## 2.3 Ion beam lithography

### 2.3.1 Focused ion beam

Focused ion beam (FIB) is a technique widely used in semiconductor industry for the site-specific analysis, material deposition, and sample milling. FIB is very successful in failure analysis for semiconductor technology as well [117]. For FIB, gallium ions are usually accelerated to 10 keV to 50 keV and focused down to 5 nm. Ions are generated from a liquid metal ion source (LMIS) consisting of a

tungsten needle mounted below a liquid gallium reservoir. The tungsten tip is coated with a thin film of gallium and situated above a high voltage extractor (~6 keV) [118]. This will produce an intense electric field to ionize the gallium and draw the liquid metal into a fine tip called Taylor cone. As the electric field is strong enough to overcome the surface tension of liquid gallium, ion emission will occur due to field evaporation and accelerated down to the column. The current that is used for FIB can be varied from 1 pA to 10 nA for different type of applications. The primary mechanism of FIB is the slow heavy ions collide with the atoms on the surface of a sample, resulting in sputtering of surface atoms. At low primary beam currents (pA), very little material is sputtered and the morphology of a sample is obtained by collecting secondary electrons or ions. However, FIB imaging is limited in its applications due to several reasons. First, the energetic ion beam will sputter and damage the sample even at the lowest beam current. Second, the ion beam does not generate signals such as characteristic X-rays that can be easily captured and used to analyze the specimen chemistry. Lastly, the secondary electrons generated are too weak to be used. So, FIB is usually incorporated with another SEM column to overcome the imaging issues [119].

Another application for FIB is to fabricate structures by sputtering surface atoms with a high beam current (nA). The FIB instrument has been utilized for site-specific specimen preparation such as TEM sample. FIB has practically no proximity effect due to the low secondary electron energy, sub 10 nm features can be obtained relatively easy on different material [120, 121]. One issue for the

milling process is the redeposition of the sputtered ions [122]. This effect is increased when FIB milling is performed in a confined or high aspect ratio trench, or when using a higher sputter beam current [123]. FIB is quite unique because it can be used for practically any material [124]. However, the material removal rate is relatively slow. To speed up the milling process, an etching gas can be introduced that can significantly enhanced the etching rate, such as bromine and iodine. The chemical bond of those reactive gas is cut the by the high energy Ga ions and formed powerful etching agents. The etch rate can be enhanced about 20 times compared to absence of etching gas [125]. Another benefit of introduce etching gas is that the sputtered materials tend to be volatilized and reduce the likelihood of material redeposition. FIB is also widely applied for metallic or dielectric film deposition such as platinum, tungsten, and  $\text{SiO}_2$  film. The mechanism for deposition is the adsorption of volatile precursor molecules onto the sample surface and decomposition of the molecules by energetic ions. The metal deposition can be used in integrated circuit for metal line repairmen as well as for device modifications [126]. Compared to EBL, photoresist is more sensitive to FIB due to the higher mass of the Ga ions [127]. It was found that PMMA resist was about a factor of 300 more sensitive for Ga ions than electrons [128]. This allows FIB a faster exposure of resist and higher processing speed, comparable to optical laser writer lithography. One more advantage is that it has a negligible proximity effect. As a consequence, FIB can have a high resolution that is roughly equal to the beam spot. Currently, new ion sources have been

developed for lithography and imaging, such as helium ion source. So, FIB deserves more attention for future nanofabrication.

### **2.3.2 Proton beam writing**

Proton beam writing (PBW) is a relatively new 3D direct writing process that is developed at the Center for Ion Beam Applications (CIBA). Usually, a proton is accelerated to a high energy (2 MeV) and focused to tens of nanometer by a group of quadruple magnetic lenses [92]. Many photoresists have been optimized for proton beam writing like SU-8, HSQ, and PMMA. Nanostructures in HSQ resist can be fabricated down to 20 nm in dimension [129]. The primary interaction of a proton with resist material is the ion/electron collisions for most of its path [130]. Because of the high mass ratio of proton with electron ( $m_p/m_e \approx 1800$ ), protons will maintain a straight path and thousands of collisions will occur before they stop. This provides PBW few advantages over other lithographic processes. Firstly, a proton beam shows very little spread except at the end of the proton path. A Monte Carlo study shows that for a 10  $\mu\text{m}$  thick PMMA resist, the lateral displacement is around 50 nm using 2 MeV protons [131]. This can guarantee a vertical and straight sidewall, result in high aspect ratio nanostructures [132]. Also, the exposure dose when protons penetrate a material is relatively even except at the end of proton range [133]. Lastly, the penetration depth of protons can be controlled by varying the proton energy. This allows multilevel structures to be fabricated in one layer of resist [134]. PBW is a direct write process, which is considered too slow for mass production. However, the throughput will be

greatly amplified if combined with soft lithography and nanoimprint lithography. The current performance and the experimental setup of proton beam writing will be discussed in detail in the next chapter.

## 2.4 Introduction to material used in PBW

In this section, I will give a brief introduction to photoresists and the resists that are mainly used in our experiments. Photoresists SU-8, PMMA, HSQ and ma-N will be discussed first. Following this, materials like Polydimethylsiloxane (PDMS) and OrmoStamp that are used for nanofluidics chip fabrication will also be introduced.

Photoresist is a radiation-sensitive polymer that is widely used in micro/nano lithography process. Photoresists can be classified in two groups, positive resist and negative resist. When a positive resist is exposed to light or ions, the exposed part will become soluble to photoresist developer. After exposure, the long polymer chains of positive resist will be cut by photoelectric electrons or secondary electrons. So, the exposed structures will be removed by developer during chemical development process. On the contrary, for negative photoresist the polymer will be cross-linked by photoelectric electrons or secondary electrons. So, the regions that have been exposed will be insoluble to developer. Generally positive resists were more preferred for IC industry. Because positive resists get higher resolution and they do not swell during the development process. Nowadays, more and more negative resists are developed such as SU-8 and HSQ with very high resolution that is comparable with positive resist.

Photoresist usually consists of four parts: polymer, solvent, sensitizers and additives. Polymer is the main component of a photoresist. During the lithography process, polymer will crosslink or scission to form different type of structures. The solvent is used to dissolve the polymer, allowing spin coating of a thin layer of photoresist on a substrate. Sensitizers are used to control and modify photochemical reactions (crosslink and chain scission) of resist during exposure. The additives used in photoresist are to change certain properties, such as to enhance the etch resistance and to reduce the reflection of light.

The performance of a photoresist can be compared through these parameters such as sensitivity, contrast, resolution and shelf life. Sensitivity is a measurement of exposure speed. The definition of sensitivity for positive and negative resist is different. For positive resist, the sensitivity is the exposure dose needed to completely remove the resist after chemical development ( $D_c$ , see fig 2.4). While for negative resist, it is defined as the exposure dose to keep half of the original resist thickness after chemical development ( $D_h$ , see fig 2.5). Figure 2.4 and 2.5 show the development curve (remaining resist thickness) with the exposure dose for positive and negative resists.

The contrast of a photoresist (see definition of  $\gamma$  in fig 2.4 & 2.5) defines the develop rate as a function of the exposure dose [135]. A photoresist with high contrast can be used to fabricate vertical sidewalls and high aspect ratio structures.

Figure 2.4 shows a comparison of high contrast and low contrast positive resist. For an ideal positive resist, the developing curve is a step function (contrast = infinity).

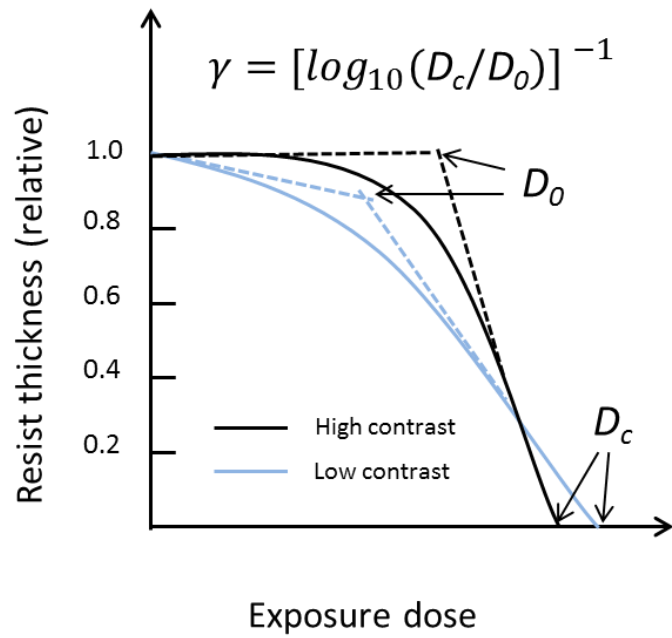


Figure 2.4 Relative resist thickness vs exposure dose for positive resist

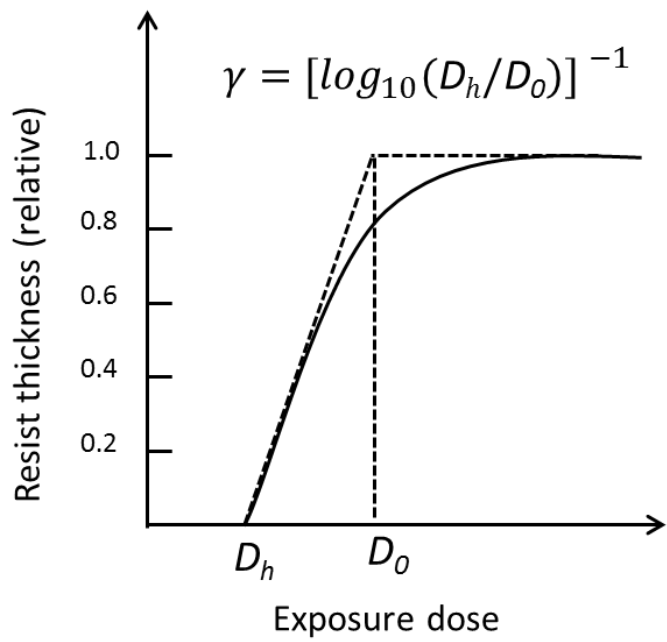


Figure 2.5 Relative resist thickness vs exposure dose for negative resist

The resolution of a photoresist depends on many factors. For the resist itself, molecular weight, resist contrast and sensitivity can affect the resolution. Other outside factors like exposure system and exposure dose, soft and post bake, developer can also affect the resolution.

In our experiments, few types of positive and negative resists were used for fabricating micro/nano structures. SU-8 and HSQ resists were used to fabricate micro/nanolines for PDMS casting. The reason is because HSQ has a very good resolution and is very stable during the PDMS casting process. Resist ma-N and ma-P were used to fabricate structure for nickel mold electroplating because they can be removed easily after plating down to 200 nm. A brief introduction will be given for several of these resists.

#### **2.4.1 SU-8 resist**

SU-8 is a widely used epoxy-based negative photoresist (fig 2.6). SU-8 has thickness ranging from sub-micron to hundreds of microns. It is most commonly processed with UV radiation (365 nm). It is also suitable for electron beam lithography and proton beam writing. The process of SU-8 resist is different for UV and PBW. The crosslinking process for UV irradiation takes two steps (1) formation of a strong acid during the exposure process, followed by (2) thermal post exposure bake (PEB) to crosslink the photoresist. For PBW, SU-8 can be crosslinked by directly expose with protons. The SU-8 developer can be used to develop the resist that being exposed either by UV or PBW. SU-8 shows very good resolution for PBW. With proton beam writing, 60 nm lines can be

fabricated on a 10  $\mu\text{m}$  thick SU-8 resist [132]. SU-8 has been widely used for MEMS for micromachining and microelectronic applications. Nowadays it is mainly used for the fabrication of microfluidics chip via soft lithography. In our experiment, different SU-8 molds were fabricated by PBW and UV lithography for PDMS casting process. The introduction of OrmoStamp in NIL applications make SU-8 a more attractive alternative.

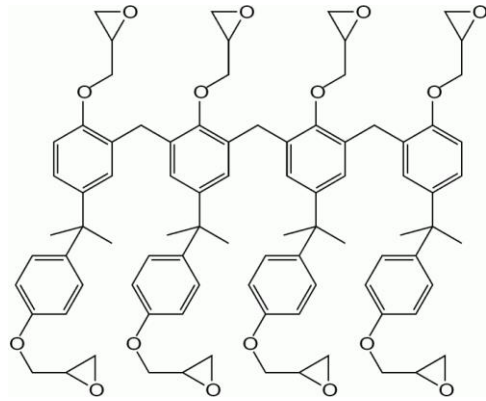


Figure 2. 6 SU-8 molecule structure

#### 2.4.2 PMMA resist

Polymethyl Methacrylate (PMMA) is a positive resist composed of methyl methacrylate polymer ( $\text{C}_5\text{O}_2\text{H}_8$ ). The molecular structure of PMMA is shown in figure 2.7. PMMA is commonly used as a resist for electron beam lithography (EBL), deep UV (248 nm) and proton beam writing. Standard PMMA products cover a wide range of film thickness from about 100 nm to 5  $\mu\text{m}$  allowing fabrication of micro/nano features. PMMA has a very high resolution, sub 10 nm ridge can be achieved with EBL [136]. PMMA is also a superior resist for PBW, features size down to 30 nm can be achieved with smooth sidewall [137]. One

more advantage for PMMA is that it can be easily removed by acetone. These characteristics make PMMA a very good candidate for nickel mold fabrication. A high aspect ratio (about 69 times) 72 nm nickel ridge has been fabricated with PMMA at CIBA [138]. For structures fabricated with PBW, PMMA can be developed by a mixer of isopropanol (IPA) with DI water or GG developer. GG developer contains 60% diethyleneglycolmonobutyl ether, 20% morpholine, 5% ethanolamine and 15% water [139]. GG developer is suitable for thick resist development and causes almost no swelling of the resist. The down side is its relatively long development time for thick resist layers. In our lab, a less viscous IPA/DI mixer at the ratio of 7:3 was usually used for PMMA development. PMMA is also a transparent thermoplastic, often used as an alternative to glass. The optical transparency and biocompatibility make it suitable for lab on chip devices fabrication. PMMA was not only used for PBW of nano structures, but also used for thermal imprinting in our experiment.

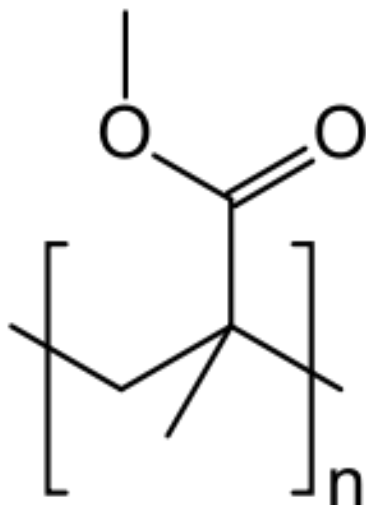


Figure 2. 7 PMMA polymer structure

### 2.4.3 HSQ resist

Hydrogen silsesquioxane (HSQ, from Dow Corning) is a negative tone resist and consists of  $\text{H}_8\text{Si}_8\text{O}_{12}$  monomer (see fig 2.4). It is suitable for electron beam lithography, extreme ultraviolet (EUV), and proton beam writing. HSQ shows a high resolution for electron beam lithography, less than 5 nm features can be fabricated with EBL [140]. For proton beam writing, resolution down to 20 nm has been achieved [129]. In our experiments, HSQ was mainly used to fabricate mold for PDMS casting with PBW. During the exposure with PBW, the crosslinking of HSQ is formed by scission of either Si-H bond (bond strength 8.95 eV) or the Si-H bond (bond strength 4.08 eV) with secondary electrons. Besides the lithography process, the development plays an important role in the patterning of high resolution HSQ. Usually, HSQ is developed with aqueous solutions of different developers, 2.38% tetramethylammonium hydroxide (TMAH) being the one most frequently used for proton beam writing [141]. To serve as a resist mold, a good adhesion with substrate is very important. In most proton beam writing experiments, HSQ is directly spin coated on Si substrate without using a primer to improve the resist adhesion to the substrate. To fabricate a high aspect ratio structure, a thin Ti film (2-4 nm) can be sputtered on the substrate to increase the adhesion of HSQ and substrate [142]. In the last decade, HSQ has shown to be a promising negative resist for PBW. However, the fabrication with HSQ resist gives non-reproducible results with PBW. This is due to the contrast and sensitivity of HSQ resist, which deteriorate over time. A report shows that the contrast of HSQ resist (850 nm thick) drops from 3.2 to 1.7 after about 9 month

[129, 143]. The sensitivity changes about 5 times to fully crosslink the same type of resist [144]. HSQ resist has a limited shelf life which makes it important to fabricate the resist in time to get nano sized high aspect ratio structures.

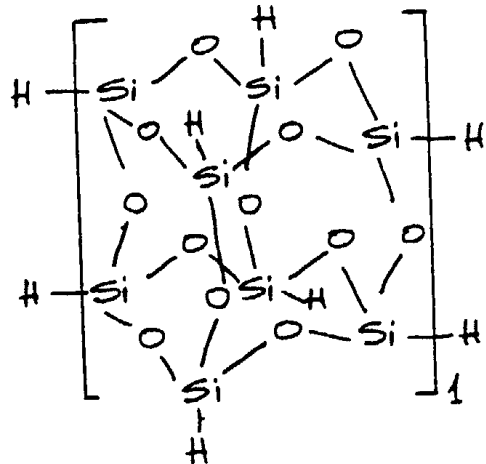


Figure 2. 8 HSQ monomer structure

#### 2.4.4 ma-N

Resist ma-N is a negative tone photoresist developed by Microresist Technology. In our experiments, ma-N 2400 series were used for fabricating nano structures because of the higher resolution compared to other ma-N series. It covers a thickness from 100 nm to about 1  $\mu\text{m}$ . ma-N resist exhibits high wet and dry etch resistance so that it can be used as an etch mask. ma-N 2400 shows a high resolution for both PBW and EBL. With PBW, a feature size down to 60 nm can be fabricated at CIBA which is comparable to EBL [145, 146]. The developer for ma-N 2400 resist can be alkaline based developer such as ma-D 331, ma-D 332 and ma-D 552. After exposed by PBW, the resist can be easily removed down to

500 nm [149]. So in our experiments, nickel plating was conducted to fabricate nickel mold with this resist.

#### **2.4.5 SML**

SML resist is a positive organic resist, it has been recently been introduced by EM Resist Ltd. The resist has a thickness ranging from 50 nm to 2  $\mu\text{m}$ , designed for high aspect ratio nano structure fabrication. SML has been test by EBL, aspect ratio of 10 : 1 and 50 : 1 have been obtained using 10 keV and 100 keV electron beam energy [147]. This represents an improvement of more than two times over the traditional PMMA resist [148]. Similar with PMMA, IPA/DI mixture and MIBK/IPA mixture are both suitable for SML development. SML is a new resist to PBW and has similarities with PMMA. It can be easily removed after Ni electroplating and could be a useful resist for nickel mold fabrication via PBW and electropainting [149]. PBW was conducted with SML resist for OrmoStamp mold fabrication.

#### **2.4.5 PDMS**

Polydimethylsiloxane (PDMS) is silicon based organic polymer, known as silicones (see fig 2.9). Different from the resist polymers, PDMS is most used for copying structures from a master mold called soft lithography. In our experiment, the Sylgard 184 Silicone Elastomer Kit (Dow corning) was used to fabricate PDMS fluidic devices. The PDMS kit consists of a bottle of elastomer base and curing agent. By mixing these two chemicals, the PDMS monomer will be cross

linked by thermal curing. The mass ratio of elastomer base to curing agent usually used is 10 : 1. It can be varied accordingly to satisfy different requirement on elastic and mechanical properties [150]. The fabrication process for PDMS chip is simple and usually a master mold fabricated with PBW can be used for hundreds of times without deterioration [57]. PDMS has very good optical transparency, and is inert, non-toxic. So PDMS has been widely applied for bio-MEMS experiments. The easy fabrication process and low cost compared with Si/glass make PDMS more and more popular in micro/nano fluidics device fabrication. In our experiment, PDMS was mainly used for DNA analysis and ratchet separation chips.

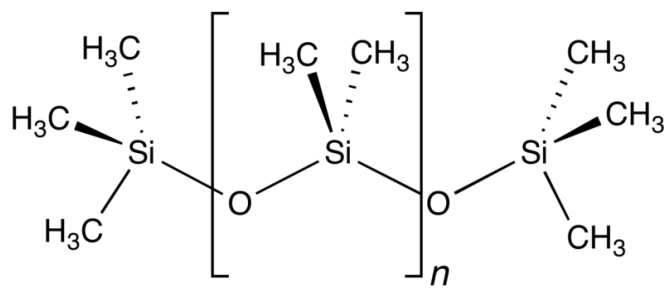


Figure 2. 9 PDMS polymer structure

#### 2.4.6 OrmoStamp

OrmoStamp (Micro resist technologies) is an inorganic-organic hybrid polymer used for fabricating of master molds. It is a solvent free resin with high viscosity. OrmoStamp can be cured by UV (365 nm or above) exposure. After crosslinking, OrmoStamp will be solidified reaching high physical and mechanical stability. So OrmoStamp can be used as a thermal or UV based nano imprint lithography (NIL) stamp. The advantage compared with other NIL stamps (quartz, Si, or nickel mold)

is the simple fabrication process. OrmoStamp mold can be easily fabricated by copying other types of mold with high fidelity. It is claimed that OrmoStamp has an ultra-high resolution (sub 10 nm) and good physical stability enables the imprinting temperature to be as high as 160 °C [151]. Iren *et al* have reported that feature size for OrmoStamp structures can go down to 30 nm [152]. In our experiment, OrmoStamp was mainly used to fabricate molds for PMMA thermal imprinting.

## **Chapter 3. Fabrication of micro/nano fluidic devices**

In this chapter, proton beam writing and other experimental facilities in the Center for Ion Beam Applications (CIBA) are introduced. After that, the fabrication process of making several master molds (resist, nickel, and OrmoStamp molds), PDMS casting for micro/nano fluidics experiment, PMMA nanoimprinting and bonding are discussed in detail.

### **3.1 Proton beam writing facility**

Proton beam writing is a direct write process developed by Frank Watt and his colleagues at Center for Ion Beam Applications (CIBA), Department of physics, National University of Singapore [153]. A schematic overview of proton beam writing facility is shown in figure 3.1. The CIBA facility consists of a 3.5 MeV Singletron accelerator with five different beam lines. The accelerator was obtained from High Voltage Engineering Europa (HVEE) with higher energy stability and brightness compared with the old Van de Graaff accelerator used in CIBA [132]. With this new accelerator, a higher beam resolution and uniform exposure dose can be guaranteed. In between the accelerator and beam lines, few components are organized in order: (a) High voltage X/Y steerers used to steer the beam in X and Y direction; (b) 90° analyzing magnet used for filtering ions with a very stable energy of 2 MeV (+/- 20 eV) for experiment; (c) Object slits used for cutting and defining the ion beam size; (d) Switching magnet used for tuning the beam into a desired beam lines. Different applications are developed for those

five beam lines. From left to right they are: (1) Proton beam writing for micro/nano lithography on photo resist and silicon (10 degree beam line); (2) Second generation proton beam writing aimed at sub 10 nm lithography (20 degree beam line); (3) Bioimaging beam line for whole cell imaging (30 degree beam line); (4) Nuclear microprobe and broad beam exposure for material characterization (45 degree beam line); (5) High resolution RBS (90 degree beam line).

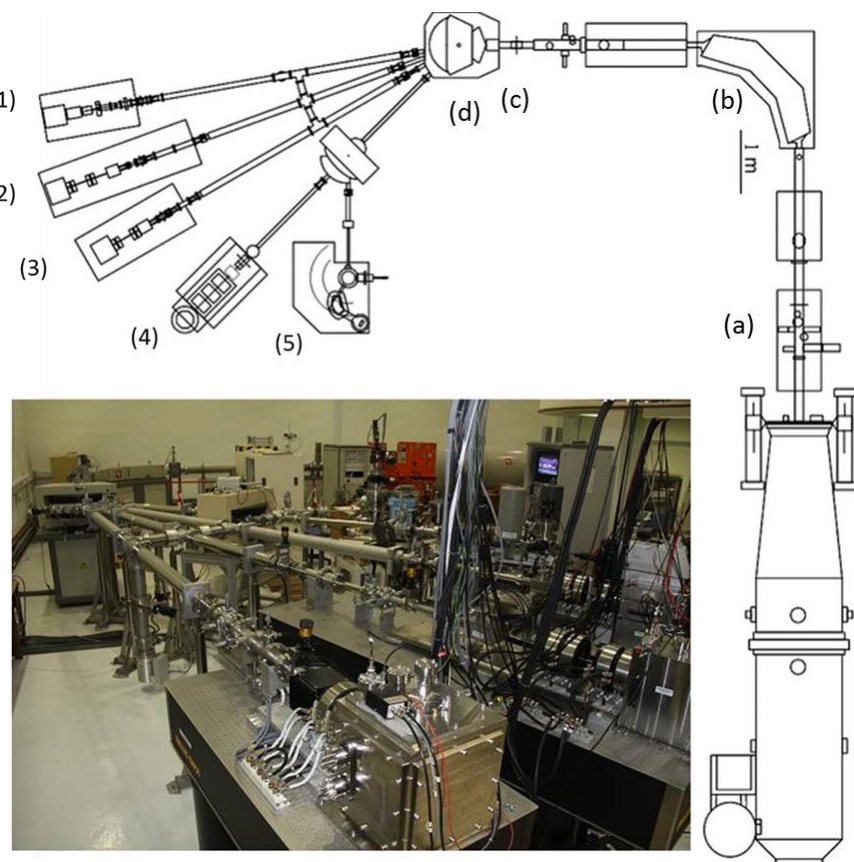


Figure 3. 1 Acelerator in Centre for Ion Beam applications (CIBA) (a) X/Y steerers; (b) 90° analyzing magnet; (c) Object slits; (d) Switching magnet

Different beamlines: (1) Proton beam writing (PBW); (2) Second generation PBW; (3) Bioimaging; (4) Nuclear microprobe and broad beam exposure; (5) High resolution RBS

The accelerator is used to generate high energy ions (proton,  $H_2^+$ , or  $He^+$ ). Ions are generated from a high brightness RF (radio frequency) source excited by an RF oscillator. Usually protons or  $H_2^+$  are chosen for proton beam writing. The ions (proton or  $H_2^+$ ) are first generated in the RF ion source, and then accelerated to certain energy (2 MeV for proton beam writing). At this energy, protons/  $H_2^+$  can penetrate sample very deep while maintaining a relatively straight path. After this, proton or  $H_2^+$  ions are filtered by the 90 degree analyzing magnet, and further tuned into a desired beam line by the switching magnet.

The 10 degree and 20 degree beam line were mainly using for my experiments. I will show more details of this two beam lines. Figure 3.2 shows a photo and schematic diagram of 10 degree beam line.

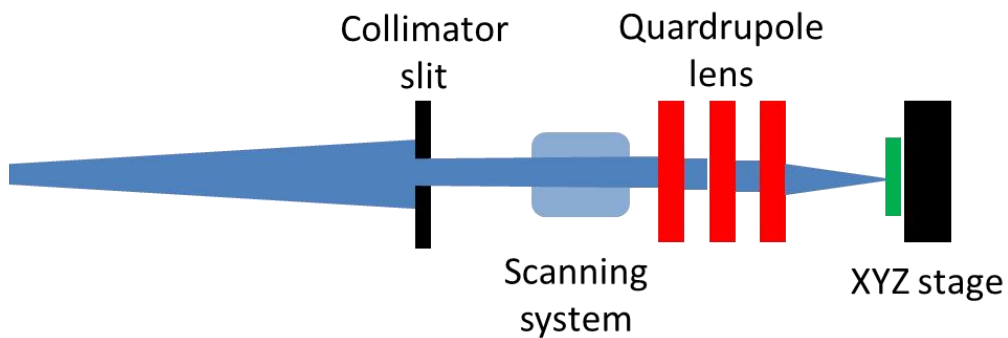
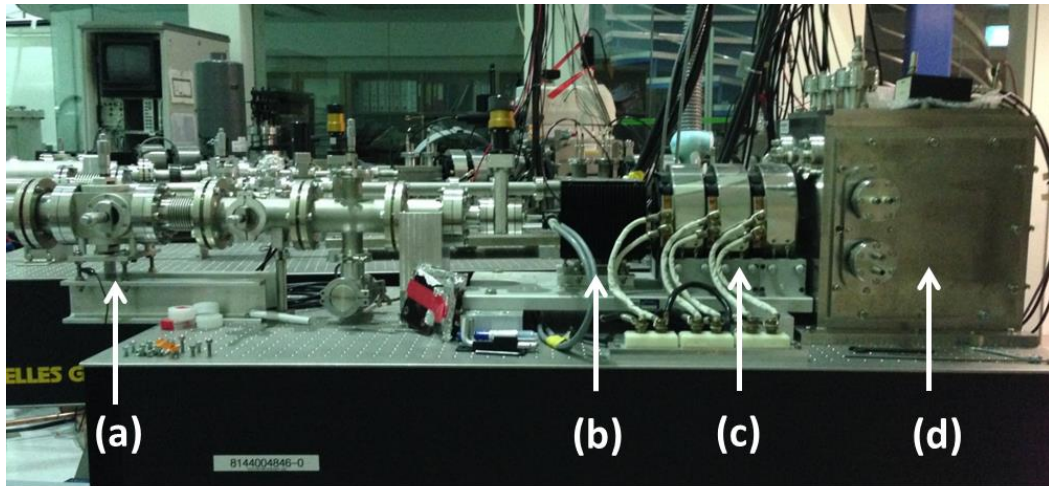


Figure 3. 2 Organization 10 degree beam line: (a) Collimator slit; (b) Magnetic scanning system; (c) Quadrupole focusing lenses; (d) Vacuum chamber

The 10 degree beam line consists of collimator slits, magnetic scanning coils, quadrupole focusing lenses, and target chamber. Collimator slits are defined by four Tungsten carbide cylinders organized in X and Y directions. By cutting the large angle scattered ions from the object slits, the shape of ion beam can be adjusted into a well-defined square with uniform intensity. Magnetic scanning is used in this beam line which consists of a scan coils. The scan software named ‘Ionscan’ was developed at CIBA, NUS [154]. Several types of files can be input into the software and converted to final ‘epl’ PBW files. The first one is the ‘bmp’

file (monochrome bitmap in  $2^n$  resolution) can be operated from 512 to 4096 resolution. BMP file allows us to scan arbitrary shapes. The second one is ‘emc’ file (the emc file is an ASCII file with an .emc extension) that allows us to define several basic shapes (see table 3.1 and fig 3.3).

Table 3. 1 Example for ‘emc’ file definition

!EMC1	.....	Header for emc version 1.0
!RES	.....	Resolution keyword
1024	.....	Resolution value(512, 1024....2048)
!SSQU	.....	Spiral square keyword
340	.....	centre x-coord
340	.....	centre y-coord
101	.....	Side width
!SCIR	.....	Spiral circle keyword
680	.....	centre x-coord
340	.....	centre y-coord
50	.....	Inner radius
120	.....	Outer radius
!RREC	.....	Raster rectangle keyword
0	.....	Scan direction
620	.....	First x-coord
620	.....	First y-coord
740	.....	Last x-coord
840	.....	Last y-coord
!SREC	.....	Raster rectangle keyword
1	.....	Scan direction
220	.....	First x-coord
740	.....	First y-coord
400	.....	Last x-coord
800	.....	Last y-coord

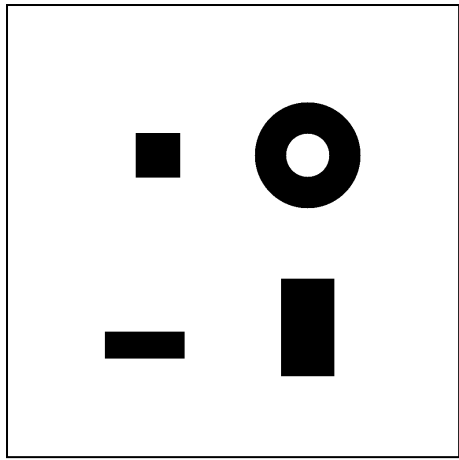


Figure 3. 3 scan file produce from example code

With the magnetic scanning system, a maximum scan size of  $500 \mu\text{m} \times 500 \mu\text{m}$  in one single writing field can be achieved. The ‘ionscan’ software is also able to perform combined stage and magnetic scanning. This allows us to fabricate micro/nanolines up to 25 mm long.

At the right of the scanning system is a triplet configuration magnetic quadrupole lenses (OM52) [155]. The lens system operates at an object distance of 7 m and focusing image distance of 70 mm [156]. This system gives a demagnification of  $228 \times 60$  in the X and Y directions respectively and a minimum beam focus of 35 nm  $\times$  75 nm can be achieved [157].

Inside the target chamber, there is an EXFO Burleigh Inchworm® XYZ stage used to mount a sample holder. The stage has a 25 mm travel distance for all axes with 20 nm closed loop resolution. In addition, an annular Rutherford Backscattering (RBS) detector and a channeltron electron multiplier (CEM) detector are mounted inside the target chamber. The RBS detector is used to calibrate proton

exposure dose for a large beam current (typically  $> 1$  pA). For small beam current, a silicon PIN photodiode will be used to measure the count of protons. The CEM detector is used to collect the proton induced secondary electrons for beam imaging and focusing.

The fabrication of nanometer structures relies on the beam focus. A high quality nickel grid is used to focus the beam to sub 100 nm size. In our experiment, a free standing nickel grid was fabricated with PBW and electroplating [158]. This nickel grid carries a smooth and vertical sidewall ( $89.6^\circ$ ) that is suitable for scanning transmission ion microscope (STIM) and sub 100 nm beam focusing. Figure 3.4a shows an optical image of the nickel grid fabricated with PBW. When a proton beam scans over the nickel grid, the secondary electrons are generated and collected by the CEM detector. To estimate the beam size in X and Y directions, horizontal and a vertical line scans at the nickel edge are performed. Figure 3.4b shows an approximate beam size of  $90\text{ nm} \times 250\text{ nm}$  in X and Y directions respectively. Here, the opening of object slits for X and Y directions are around  $12\text{ }\mu\text{m}$  and  $8\text{ }\mu\text{m}$  using a 2 MeV proton beam.

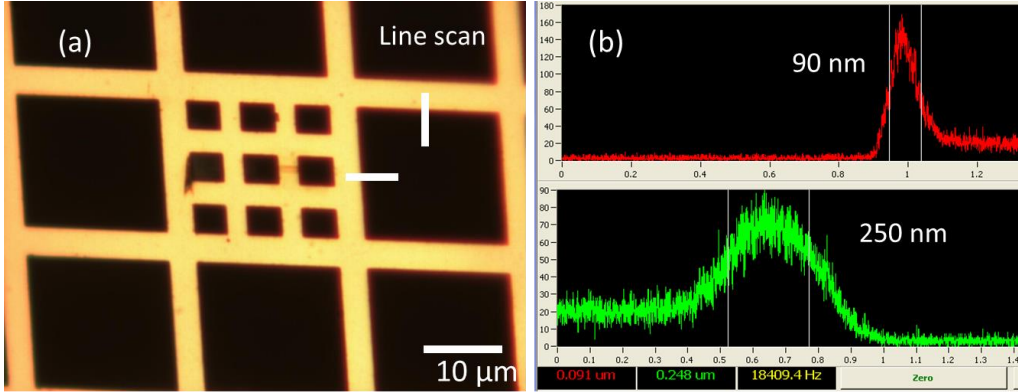


Figure 3.4 (a) Optical image of the Ni grid; line scan is labeled at the edge of nickel edge for both X and Y directions. (b) Secondary electron collect from the line scan for X and Y directions (estimation of beam size is FWHM)

There are several major differences between 10 degree and 20 degree beam line.

In the second generation beam line (20 degree beam line), a new triplet quadrupole lens configuration (demagnification  $857 \times 130$ ) is used which gives a higher resolution of  $19 \text{ nm} \times 30 \text{ nm}$  in X and Y directions respectively [92]. One disadvantage for this high demagnification is that the scan size (maximum about  $120 \mu\text{m} \times 120 \mu\text{m}$ ) is rather small compared to 10 degree. With the newly built autofocus system in the 20 degree beam line, a high resolution beam can be easily achieved and a beam focus of sub 10 nm has been realized [159]. Another big difference with 20 degree beam line is the electrostatic scanning system with X and Y scanning plates. The scan system can be one or two orders faster compared with the magnetic scan system. Also, the scanning plates are accurately aligned so that X and Y directions are orthogonal. While in 10 degree beam line, the X and Y scan is not orthogonal due to misalignment.

### **3.2 μPG 101 laser writer**

Laser writer ( $\mu$ PG 101) is used in our experiments for UV mask fabrication. The  $\mu$ PG 101 is an economical and easy to use micro pattern generator for direct writing and mask fabrication. The laser writer is equipped with a diode laser at 405 nm and is mainly used for direct writing of AZ resist. This laser writer is suitable for large area fabrication (up to 100 mm  $\times$  100 mm) with a speed of 30 mm<sup>2</sup>/min and 100 nm address grid [160]. The minimum structure size can go down to around 1  $\mu$ m. ‘BMP’ and ‘DXF’ files are usually used to design the structures and these files can be easily modified with Photoshop and AutoCAD. The blank photomasks used for UV lithography are obtained from Nanoflim (3”  $\times$  3”  $\times$  1.5 mm). The UV mask consists of three layers (Soda lime/Cr/AZ 1518) in a sandwich configuration. The thickness for Cr and AZ resist are 100 nm and 530 nm respectively.

### **3.3 UV aligner**

In CIBA, we have built a class 1000 cleanroom used for sample preparation and chemical development. Several facilities are installed inside the cleanroom such as spin coater, UV aligner, plasma cleaner, plating machine and nano imprinter to keep a clean experimental environment.

PBW is mainly used in my experiment for nano structure fabrication. To fabricate multilevel structures, it is not so convenient to use only PBW. A simple UV aligner was built to align micro structures with nano structures (see fig 3.5). The UV aligner consists of three parts which are UV system, stage system and camera

system. Two UV systems (i-line, DUV) are installed in this UV aligner which allows us to fabricate with both SU-8 and PMMA resists. The stage system is used for mounting and moving samples in X/Y/Z directions. The camera system consists out of a camera, a light source and a monitor. When aligning sample with UV mask, the camera system is used to observe the relative position of micro patterns on the UV mask with respect to nano structures on the sample. By moving the sample mounted on the stage, micro/nano structure can be aligned. With this UV aligner, we can align micro and nano structures with around  $10 \mu\text{m}$  accuracy. This is more than enough for us to do the simple alignment.

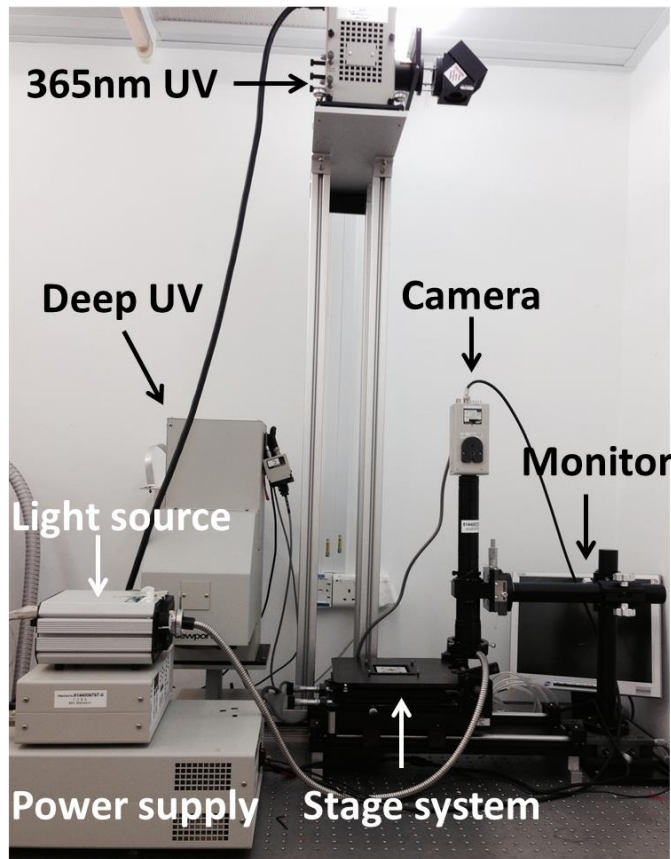


Figure 3. 5 UV aligner for micro structure fabrication

### 3.4 Plating machine

Electroplating has a very long history. It is a process that uses electrical current to deposit metal on an electrode. Electroplating has been widely used in industry for changing the surface properties of an object such as corrosion protection, lubricity and abrasion resistance.

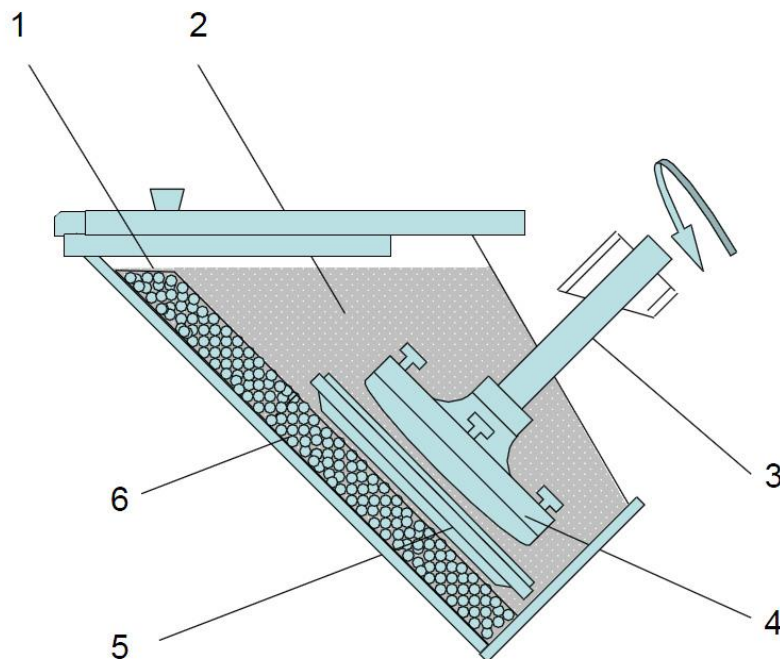


Figure 3. 6 Schematic of the RD.50 Electroplating cell: (1) Anode basket; (2) Electrolyte; (3) Spindle drive; (4) Cathode and sample holder; (5) Tunnel battle; (6) nickel pallets

In our experiment, nickel electroplating was conducted with Technotrans AG, RD. 50 plating machine to produce high quality nickel stamps. The electroplating cell consists of 6 parts which are shown in fig 3.6. The sample is mounted on a titanium plate connected to a spindle drive which serves as cathode. The

electroplating bath consists of Ni sulfamate, Ni chloride, boric acid and wetting agent (see table 3.2).

Table 3. 2 Compositions of Ni electroplating solution

Composition	Density
Ni sulfamate $\text{Ni}(\text{SO}_3\text{NH})_2$ (g/L)	370~390
Ni chloride $\text{NiCl}_2$ (g/L)	10
Boric acid $\text{H}_3\text{BO}_3$ (g/L)	40~55
Wetting agent      (mL/L)	0.05~0.1

Nickel sulfamate solutions are widely used for electroplating with the capability of high plating rate, low residual stress and good ductility [161]. During the plating process, hydrogen bubbles may form at the surface of the cathode. This will deteriorate the plating structure. So, wetting agent is used in the Ni bath to reduce the surface and interfacial tension [162]. When currents are applied through the electrodes, nickel ions from the bath will deposit on the cathode sample. The chemical reaction is shown below.



There are several factors influencing the plating process and the plated structures. The operating temperature and pH of the electrolyte need to be constantly controlled and adjusted. The temperature should be around 50 ~ 52 °C and is controlled by a thermostat-controlled porcelain heater. The pH value is about 3.5~3.7 and is adjusted by a pH meter together with a liquid pump. Boric acid will

be added by this pump if the pH value is too high. The total electrolyte is about 90 L and is continuously cycled through a 10  $\mu\text{m}$  and then a 0.5  $\mu\text{m}$  filter to maintain a low particle concentration.

### 3.4 Fabrication of master mold with PBW

Two types of designs were fabricated in my experiments for DNA analysis. They are straight nanoline configuration shown in figure 3.7a and cross nanoline configuration shown in figure 3.7b. These two designs were digitized to 2048  $\times$  2048 pixels using IonScan software [ 163 ]. The 13 nanolines of straight configuration at the center part are single pixel lines. The 13 horizontal and vertical nanolines for the cross configuration at the center part are also single pixel lines.

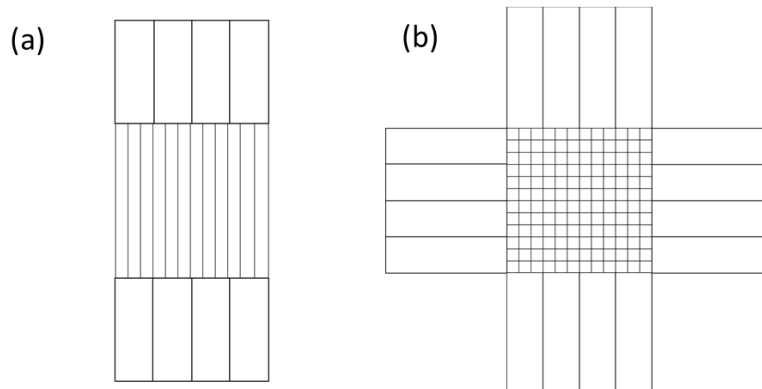


Figure 3. 7 Schematic designs of nanolines (a) Straight nanolines; (b) Cross nanolines

After the nanolines were patterned by PBW, a multi-level structure was usually fabricated on another thick resist (few microns) with UV lithography. And the UV

patterns we have used are shown in figure 3.8. The micro lines are around tens of microns in width and connect to circular reservoirs.

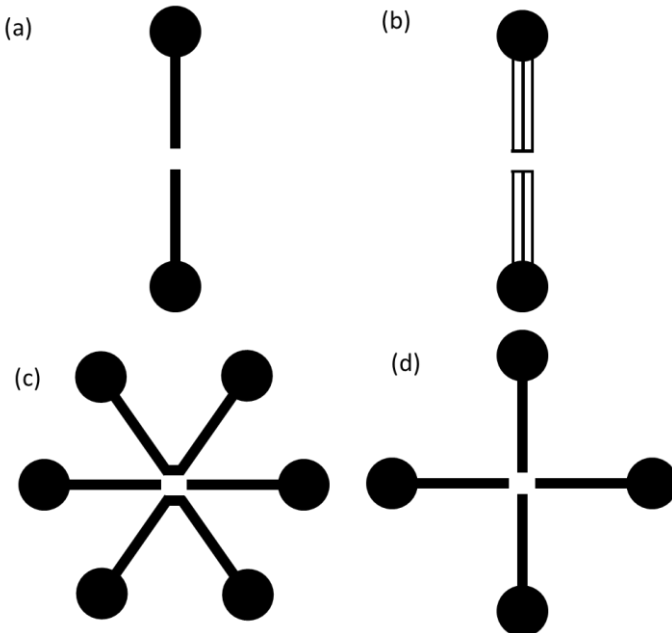


Figure 3. 8 Schematic designs of micro structures (a) and (b) are used to align with straight configuration design; (c) and (d) are used to align with cross configuration design

The microlines here serve as protein or DNA buffer feeding channels for nanochannels after PDMS casting and bonding (see fig 3.9). The buffer was first introduced into these PDMS microchannels by capillary action. After that, the buffer was supposed to cover all the reservoirs to maintain a pressure balance so that the DNA molecules will be motionless (except Brownian motion) inside the micro/nano channels. Usually DNA molecules tend to stay in the microchannels. So a current is applied to drive DNA molecules into the nanochannels from the reservoirs.

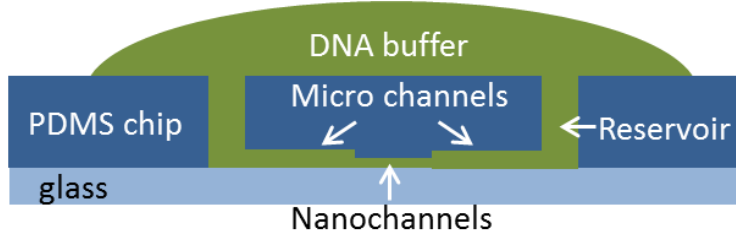


Figure 3. 9 Schematic cross-section view of the PDMS micro/nano channels, DNA buffer are filled in the channels.

In our experiment, three types of molds (resist mold, nickel mold and OrmoStamp mold) were fabricated using these two designs for PDMS LOC devices casting.

### 3.4.1 Resist mold fabrication by PBW

Here we introduce the first resist mold fabricated with HSQ and SU-8 for nanolines and microlines respectively. The fabrication process is shown in fig 3.10.

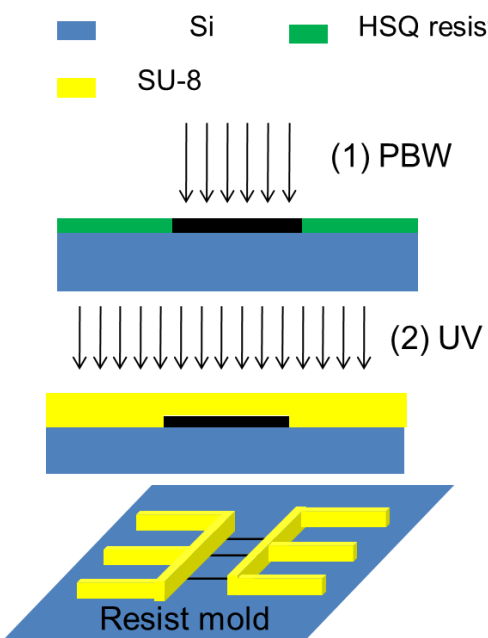


Figure 3. 10 Fabrication process for HSQ/SU-8 resist mold (1) PBW of nanolines on HSQ resist; (2) UV alignment of microlines with nanolines on SU-8 resist; (3) final resist mold

A Si substrate was heated at 150 °C for 10 minutes to remove any water vapor on the surface. After the Si substrate was cooled down. A layer of HSQ was spin coated on the Si substrate at different spin speed. Resist thickness was calibrate by scan electron microscope (SEM) for HSQ at different dilution rates with MIBK (table 3.3).

Table 3. 3 HSQ resist thickness with different dilution with MIBK

Resist	Spin speed and time	Thickness
HSQ (Fox 17) dilute with MIBK at 1:3	3000 rpm and 30s	220 nm (figure 3.11a)
HSQ (Fox 17) dilute with MIBK at 1:6	3000 rpm and 30s	100 nm (figure 3.11b)
HSQ (XR 1541, 6%)	4000 rpm and 30s	220 nm (figure 3.12)

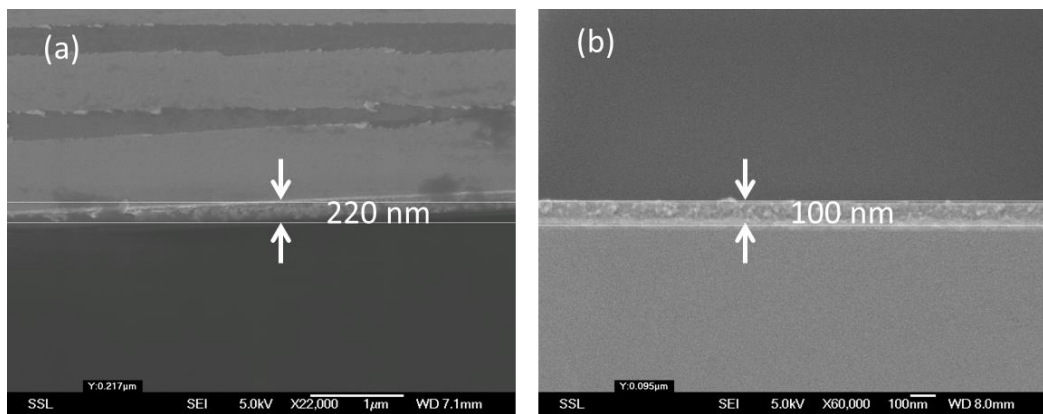


Figure 3. 11 Thickness of HSQ dilute with MIBK (a) 220 nm thick HSQ (dilute at 1:3); (2) 100 nm thick HSQ (dilute at 1:6)

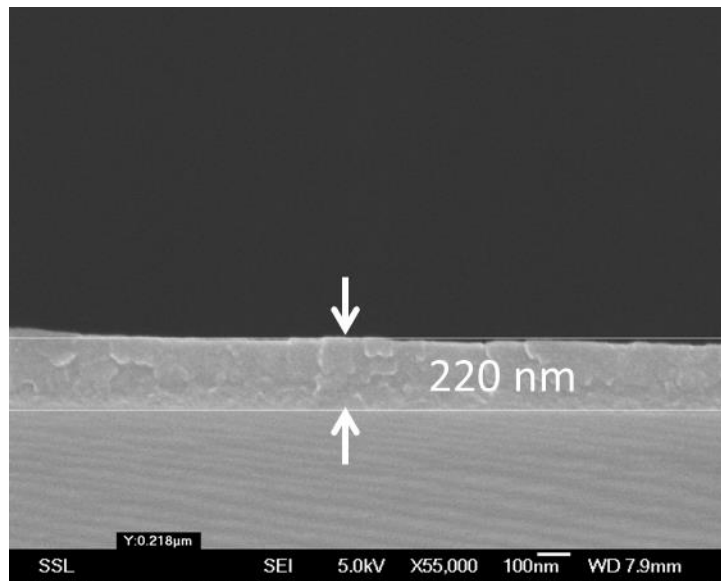


Figure 3.12 Thickness of XR1541 (6%) spin coated at 4000 rpm for 30 s

After the spin coating, all the resist samples were baked at 150 °C for 1 min. Proton beam writing was conducted at CIBA for the nanoline fabrication (see design fig 3.8 a and b). A scan size of 100  $\mu\text{m} \times 100 \mu\text{m}$  or 160  $\mu\text{m} \times 160 \mu\text{m}$  was employed in 20 and 10 degree respectively (see discussion in section 3.1). After PBW, the sample was developed at 2.38% tetramethylammonium hydroxide (TMAH) for about 1 min. During the development process, slight agitation of the developer facilitates the development. Then the sample was rinsed with DI (de-ionized) water and dried with clean nitrogen.

Secondly, SU-8 micro feeding lines (see design fig 3.8) were patterned with UV lithography. A UV mask is first fabricated using the  $\mu\text{PG}$  laser writer following the fabrication process shown in figure 3.13. (1) Expose the design with laser writer with optimal energy (20 mW, 35 % of the pixel pulse duration). (2)

Develop with diluted AZ developer (dilute with DI water at the ratio 1:4) for about 1 minute and rinse with DI water. (3) Etch the Cr layer with Chromium Etch 1020AC for about 2 minutes and rinse with DI water. (4) Remove the AZ resist layer with acetone.

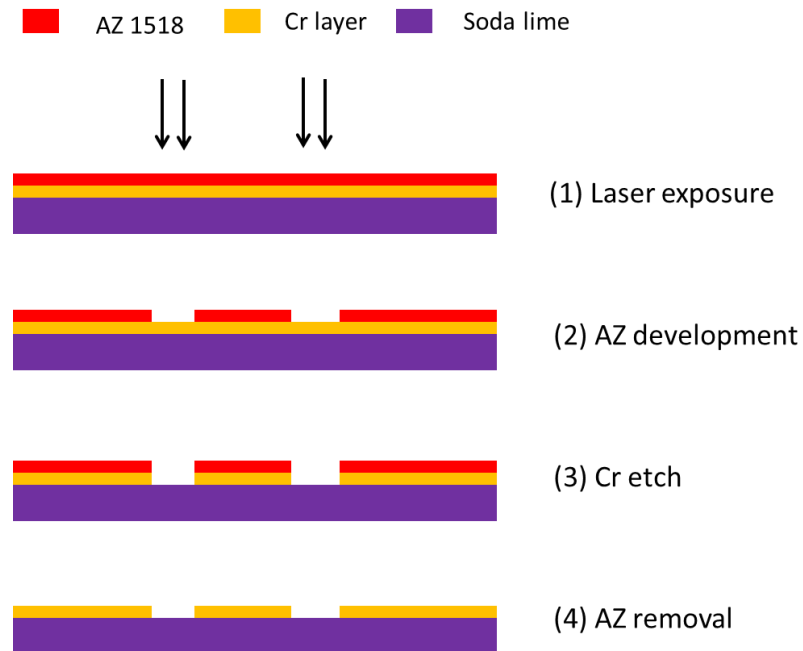


Figure 3. 13 UV mask fabrication process with  $\mu$ PG 101 laser writer

After the UV mask fabrication, the samples with nanostructures were spin coated with SU-8 2005 for 30s at 4000 rpm and baked at 95 °C for 2 min. Before SU-8 resist coating, a few nm Pt (platinum) metal layer was sputtered on the sample to increase the adhesion between SU-8 and HSQ resist. Without Pt layer, we found the micro SU-8 lines can be easily peeled off during the PDMS casting process. A JFC1600 coater was used to coat the sample at the conditions of 5 Pa and 20 mA. A Pt thickness around 2 nm can be achieved for 30 s coating.

UV lithography was performed for 20 min using UV aligner (365 nm, i-line). A post bake is needed to crosslink SU-8 polymer for UV exposure. The samples were baked on a hotplate at 95 °C for 3 min. Following that, the samples were developed by SU-8 developer for 1 to 2 min. To protect the HSQ/SU-8 molds during PDMS casting, another Teflon layer was coated on those samples to help the release of PDMS structures [164]. A thin Teflon film was reported to promote the release of PDMS replica from the Ni mold [165]. We adopted this process for polymer mold coating.

Teflon coating is widely used in our experiments as a release and protection layer for resist molds and OrmoStamp molds (section 3.4.2). The release layer was formed by spin coating a solution of amorphous fluoropolymer (Teflon AF 1600, DuPont Fluoroproducts) diluted with perfluorinated solvent (FC-40). Teflon has a very low surface energy and can be used to modulate the adhesion force between two sample layers [166]. In our experiment, Teflon AF 1600 copolymer was diluted at concentration of 0.02 % and 0.04 %. A comparison of the contact angle was made by putting a water droplet on a Teflon coated Si wafer (fig 3.14).

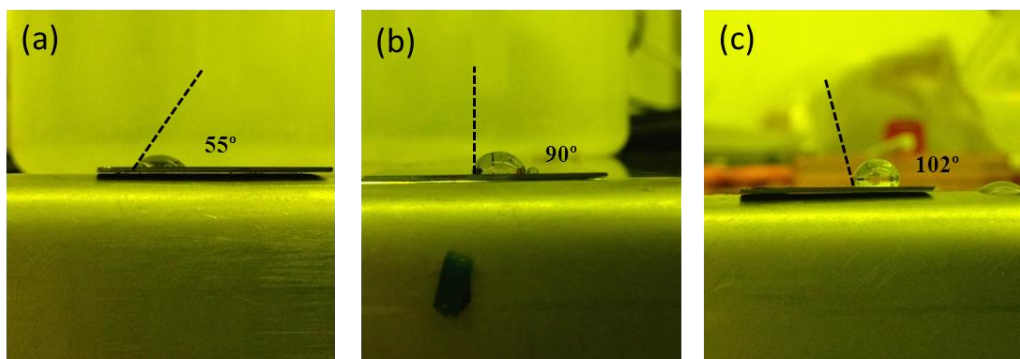


Figure 3. 14 (a) Water droplet on a plain silicon wafer (b) Water droplet on a silicon wafer coated with 0.02% Teflon solution (c) Water droplet on a silicon wafer coated with 0.04% Teflon solution

Result shows that a plain silicon wafer is hydrophilic with a contact angle of 55°.

After Teflon coating, the silicon surface changes to hydrophobic while the contact angle increase to 90° and 102° for 0.02% and 0.04% concentration respectively.

With Teflon coating, PDMS or OrmoStamp structures can be easily released from sample molds. In the experiments, Teflon was spin coated at 1500 rpm for 30 s on the resist molds and baked at 120 °C for 12 h.

### **3.4.2 OrmoStamp mold fabrication**

The second mold we fabricated is OrmoStamp mold for PMMA nano imprint lithography (NIL). HSQ/SU-8 resist mold is suitable for PDMS casting, while it is not strong enough to stand the high pressure and temperature during NIL. OrmoStamp is organic-inorganic hybrid polymer with high mechanical stability that can be used as a mold for nano imprint lithography [151]. In this experiment, different resist (HSQ, SU-8, PMMA and SML EM Resist Ltd) were patterned by PBW (see section 4.2 for PBW with these resist fabrication) and then transferred to OrmoStamp (Microresist GmbH) molds.

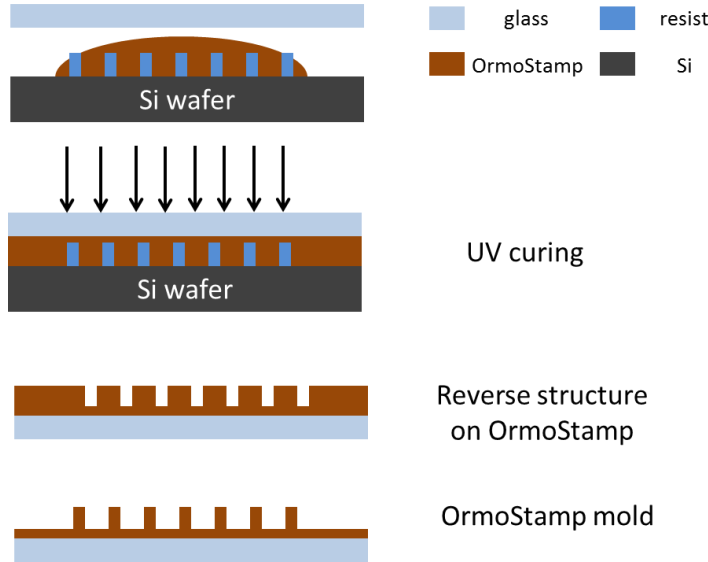


Figure 3. 15 Fabrication process for OrmoStamp mold: (1) Pour OrmoStamp and cure with UV; (2) Peel off the OrmoStamp mold from the resist mold; (3) repeat all the procedure to get the final OrmoStamp mold

The fabrication process of OrmoStamp molds are as follows (see fig 3.15). In the experiment, a glass slide was used as the substrate for the OrmoStamp structure. Firstly, a thin Ormoprime layer was spin coated on a glass slide to enhance the adhesion of OrmoStamp structures. Without Ormoprime coating, OrmoStamp can be easily peeled off during the nano imprint process. The glass slide was cleaned via plasma treatment (300 mTorr, 18 W for 30 s) and then coated with Ormoprime 08 (Micro resist technology GmbH) at 4000 rpm for 1 min. Then the glass slide was baked at 150 °C on a hot plate for 5 min. At the same time, a resist mold was coated with a thin layer of Teflon to protect the resist mold [167]. Following that, a drop of OrmoStamp was poured on the resist mold. The glass slide prepared previously was pressed on top of the sample gently by hand. Next, UV exposure (i-line 365 nm for 45 min) was conducted to crosslink the OrmoStamp. After UV exposure, the OrmoStamp was peeled off from the resist

mold, to obtain the reverse structure in OrmoStamp. If required, a 2<sup>nd</sup> generation OrmoStamp copy was made using the 1<sup>st</sup> generation OrmoStamp copy. This is called two-time copy. This final OrmoStamp copy carries the same geometry as the resist mold. Before the second copy, Teflon was coated on the first OrmoStamp copy to facilitate demolding of those two OrmoStamp structures. To solidify the OrmoStamp structure, UV exposure was again performed for 45 min.

### **3.4.3 Nickel mold fabrication**

Another mold we fabricated is nickel mold for PMMA nanoimprinting. Compared to other molds such as silicon, silicon dioxide and various metals that are used for NIL, nickel mold is the most durable mold [168]. Molds fabricated with silicon and silicon nitride can be easily broken under non-uniformed pressure.

In our experiment, nickel mold was fabricated by PBW followed by electroplating. To fabricate the nickel mold, a sacrificial resist mold is first fabricated. The sacrificial resist needs to be easily removable. In our experiment, ma-P and ma-N were chosen to fabricate the micro and nano structures. The reason is they can be removed by acetone or dedicated removers after plating [145]. However, we found that when dimension goes down to about 200 nm, the ma-N resist tend to be difficult to remove. The design fabricated for micro and nano structures follows the design of fig 3.8b and fig 3.7a. A schematic representation of the nickel mold fabrication process is shown in Fig 3.16.

The fabrication process starts by coating a clean Si wafer with 30 s Cr and 60 s Au consecutively using the magnetron sputter machine (see later discussed in

section 4.2.2). The Cr and Au layer ensure adhesion as well as electrical conductivity for electroplating. The Au/Cr/Si wafer was prebaked to dehydrate before coating with resist. After that, two resist samples were used for the nanochannel fabrication separately. They are ma-N 2401 (100 nm thickness, 3000 rpm) and ma-N 2410 (600 nm thickness, 6000 rpm). A 2 MeV  $H_2^+$  beam was focused to about  $130\text{ nm} \times 200\text{ nm}$  to scan the nanoline design (see fig 3.7a) over an area of  $160\text{ }\mu\text{m} \times 160\text{ }\mu\text{m}$  for these two samples. After the PBW, ma-N 2401 and ma-N 2410 was developed in ma-D 331 for 25 s and ma-D 525 for 130 s respectively.

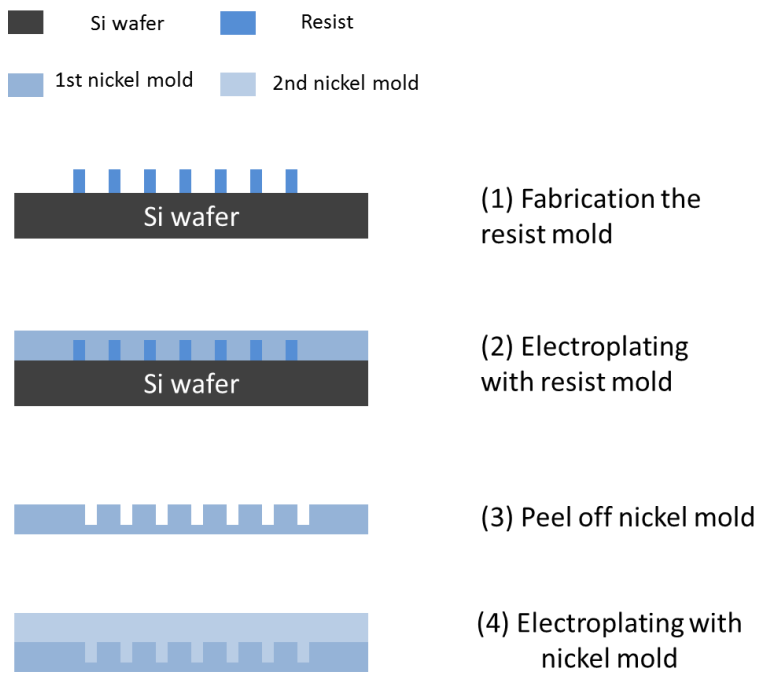


Figure 3. 16 Fabrication of nickel mold using PBW and electroplating: (1) PBW and UV lithography for the resist mold; (2) Electroplating for the resist mold; (3) Peel off nickel mold and oxide with  $H_2O_2$ ; (4) Plating with the nickel mold

In this experiment, ma-P was used for both of these two samples for fabricating microlines with UV lithography. ma-P (Microresist Technology) is a positive

resist for UV lithography. Reports show that the resist will crosslink under PBW and therefore it is a negative resist for PBW. This feature allows us to fabricate some interesting structure with PBW together with UV lithography [169].

A 4  $\mu\text{m}$  thick ma-P resist was first spin coated on these two samples with a speed of 3000 rpm. After baking at 120 °C for 2 min, we found that the nanolines don't show enough contrast under the camera system in the UV aligner. This is probably because the ma-N and ma-P resist allow light of similar wavelength to pass through while other length being scattered. So, a thin Ti seed layer (1.5 nm) was deposited using filtered cathodic vacuum arc (FCVA) onto these samples before coating of ma-P resist. The micro pattern (see fig 3.8b) on a UV mask was first fabricated with laser writer (see section 3.4.1). The nano structures were then aligned with the micro pattern and exposed with UV for 2 min. After UV exposure, these samples were developed in 2.38 % TMAH for 2 min.

The resist molds need to be electrically conductive for electroplating. So another Ti layer (1.5 nm) was deposited on the resist molds using FCVA. Two times electroplating was conducted for fabricated the same configuration of nickel molds with resist molds. So we electroplated on the resist mold and re-electroplated on the first Ni mold. Before the second time plating, the first Ni mold need to be immersed into hydrogen peroxide for 90 s. This procedure enables the first Ni stamp to be able to separate from the final Ni stamp without damage to the structure. The fabricated Ni stamp will be used for PMMA nanoimprinting which will be discussed in section 3.6.

### **3.5 PDMS casting and plasma bonding**

In our experiment, PDMS casting is the most commonly used technology to fabricate the lab on chip devices. The PDMS used in experiment is PDMS Sylgard 184 (Dow Corning). It consists of elastomer base and curing agent. The fabrication process is as follows (see fig 3.17): (1) A master mold is fabricated by PBW and UV lithography for PDMS casting. The mold can be either resist mold, OrmoStamp mold or nickel mold. (2) PDMS base was first mixed with the curing agent at a ratio of 10 : 1. Following that, PDMS was poured on the mold and then degased for about 15 min to remove all the air bubbles. Then PDMS was cross-linked by curing at 65 °C in oven for 4 hours. (3) and (4) The cured PDMS was released from the master mold and inlets were punched with a hole-puncher. (5) Treat the PDMS sample and a glass slide with air plasma (Harrick plasma cleaner, 300 mTorr, 18 W for 30 s). Oxidation with plasma will change the surface of PDMS and produce silanol terminations (SiOH). (6) The final bonding is conducted by putting the oxidized PDMS in contact with the glass. Covalent Si-O-Si bonds will form in between PDMS and glass slide to form a permanent bonding. After plasma bonding, we found that a post bake at 95 °C for 1 min can enhance the bonding strength.

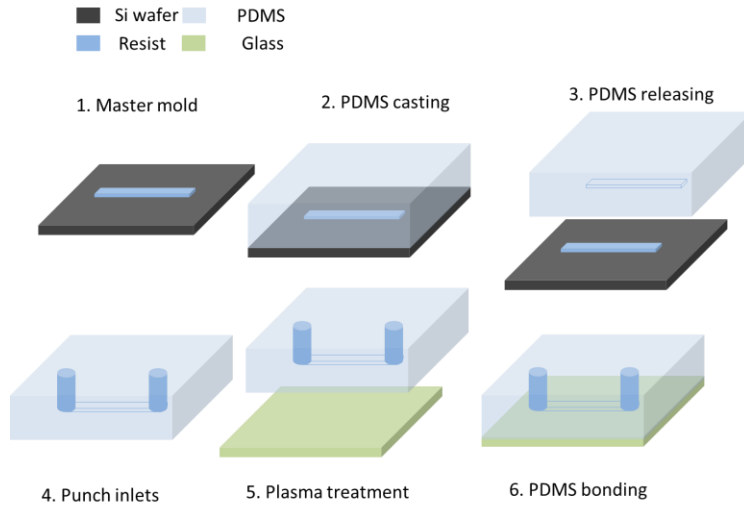


Figure 3. 17 Schematic demonstration of PDMS casting and fabrication: (1) Fabrication of master mold by PBW or UV; (2) Pour PDMS on mold and solidify PDMS in oven; (3) Release PDMS from the mold; (4) Punch holes for inlets; (5) Treat PDMS and glass with plasma; (6) Bond the PDMS and glass together

### 3.6 PMMA nano imprint lithography (NIL) and bonding

Nano imprint lithography (NIL) is a promising technology that can fabricate structures with high resolution and throughput. This technology was first introduced by Stephen *et al* who reported sub 25 nm holes can be imprinted on PMMA polymer [170]. Since then NIL has undergone huge development. There are two types of nanoimprinting they are thermal NIL and UV based NIL. In our experiment, thermal NIL was conducted for PMMA nanoimprinting. For the thermal NIL, a high temperature and pressure are applied to transfer structures from a mold to thermoplastics (PMMA, PC, PS). The advantages are high efficient and low material cost. For thermal NIL, the mold should be capable to stand high pressure and temperature without significant wear. Here, OrmoStamp molds (section 3.4.2) and nickel molds (section 3.4.3) were both used to imprint

PMMA structures. The imprinting and bonding of PMMA structure was conducted with a commercial nano imprinter (Obducat Technologies AB, NIL-2-PI 2.5 in. nano imprinter). The fabrication process of PMMA micro/nano fluidic devices is shown in fig 3.18.

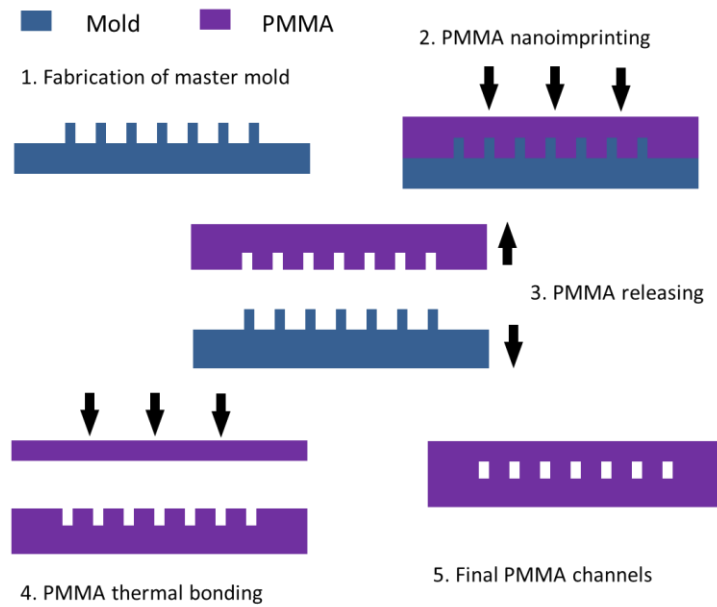


Figure 3. 18 PMMA imprinting and bonding process: (1) Fabrication of master mold, nickel mold or OrmoStamp mold; (2) Imprint PMMA nano structures by applying high pressure and temperature; (3) Releasing the PMMA structure from mold; (4) Bonding with another PMMA thin film

First, PMMA structures were imprinted by applying a high temperature and pressure. The imprinting process includes three steps (fig 3.19). (1) Bring the sample and mold into contact and heat the sample to a certain temperature. The temperature must be higher than the polymer glass transition temperature ( $T_g$ ). In our experiment, the imprinting temperature was set at 150 °C. (2) Apply high pressure to imprint the structure for certain time. To protect the master mold, a relatively low pressure (6 bars) was used. According to our experiment, this

doesn't affect the quality of the imprinted structure. And we found 300 s is long enough for the imprinting. (3) Cool the sample down to certain temperature, and release the pressure.

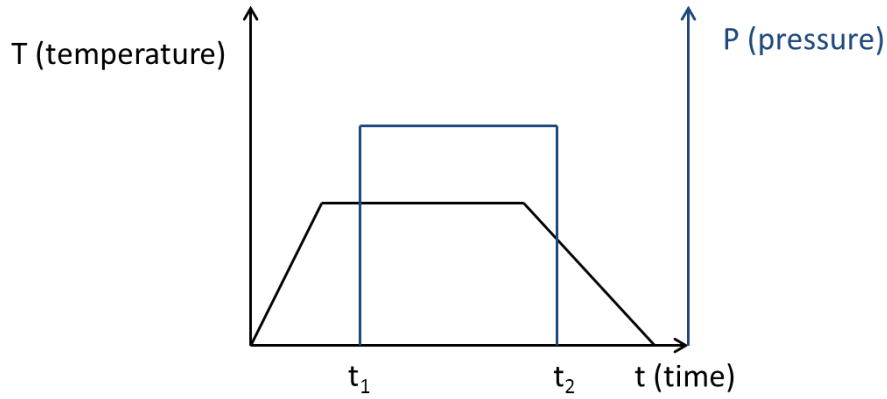


Figure 3. 19 Temperature and pressure evolution with time for PMMA imprinting and bonding process: (1) before  $t_1$ , increase and stable the temperature to certain value; (2)  $t_1 \sim t_2$ , apply a high pressure to imprint or bond; (3) after  $t_2$ , cool the sample down and release the pressure.

After the imprinting, the PMMA chip was peeled off from the master mold. Then it was bonded to another 2  $\mu\text{m}$  PMMA film. The thin PMMA film was first coated on a 50  $\mu\text{m}$  kapton film by spin coating [74]. Before the bonding, those two samples were treated with plasma for 30 s (Harrick plasma cleaner, 300 mTorr, 18 W). The plasma can increase the surface energy of PMMA and reduce the bonding temperature. Without plasma treatment, PMMA sample can be bonded at around 105 °C [74]. The problem is PMMA nanochannels will be deformed easily at this temperature. After plasma treatment, the bonding temperature can be optimized to 100 °C ( $< \text{Tg}$ , 105 °C). The bonding process follows the same process with the PMMA imprinting process. The bonding temperature and pressure are 100 °C and 6 bars respectively for 500 s.

## **Chapter 4. Nanofluidic Channels for DNA Analysis**

In this chapter, the fabrication results of PDMS and PMMA fluidic channels and characterization with DNA molecules will be discussed in detail. Firstly, the fabrication result of SU-8/HSQ resist mold is described. The resist mold was applied for DNA molecule analysis. Secondly, another two OrmoStamp and nickel molds will be presented. Lastly, PMMA imprinting results with using OrmoStamp and nickel molds is shown.

DNA is a long negatively charged polymer and huge amount of genetic information is organized linearly along its long chain. Most DNA molecules consist of two biopolymer strands coiled around each other to form a double helix. Within cells, DNA is organized into long structures (1.8 m long for human) and condensed in a very compact form by proteins to fit into small cell (few micrometers). Varies proteins (histone and H-NS), multivalent ions ( $Mg^{2+}$ ,  $Ca^{2+}$ ), macromolecules (dextran) have been investigated for the packaging process of DNA molecule in a condensed form [171, 172, 173, 174]. Protamine is a highly positively charged and arginine rich protein that will replace histone during the spermatogenesis process for DNA compaction [ 175 ]. During the DNA compaction process, protamine can bind with a DNA molecule forming tight interlocks. This results in a very condensed toroid conformation of the DNA molecule. DNA condensation is considered essential for the minimization of DNA damage by mutagens and reactive oxidizing species [ 176 ]. Protamine was investigated in our experiment for the DNA molecule condensation. The reaction of DNA molecules under biological conditions is difficult to be observed by

fluorescence microscopy at bulk phase because of the diffraction limitation. When DNA molecules are confined in a nanochannel, the conformational responses is easy to be visualized due to the elongation of DNA molecule by nanochannel. DNA conformation confined inside a nanochannel depends on the channel dimension. When the persistence length of DNA is smaller than the channel dimension, the molecule will behave like a group of DNA blobs (see fig. 4.1). These blobs trend to repel each other because of the negative charge. The final DNA contour length inside a nanochannel is dependent on the channel dimension and persistence length [ 177 ]. In our experiment, different types of PDMS nanochannels were fabricated and used for DNA analysis. The fabrication results of those fluidic DNA chips are as follows.

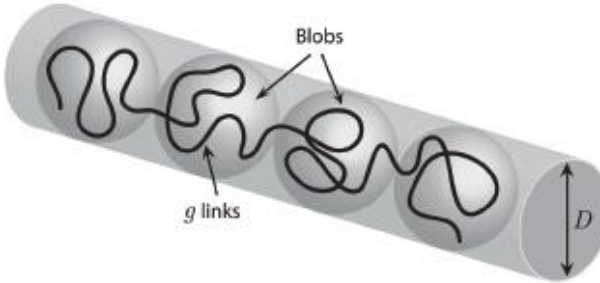


Figure 4. 1 DNA molecule confine in a nanochannel

## 4.1 SU-8+HSQ resist mold and DNA analysis

### 4.1.1 SU-8+HSQ resist mold fabrication result

Few PBW experiments were conducted with HSQ resist for different nanolines geometries. In the first experiment, a 220 nm thick HSQ resist (Fox 17/MIBK at the ratio of 1:3) was spin coated and patterned by PBW. A 2 MeV proton beam

was focused to  $80 \text{ nm} \times 250 \text{ nm}$  and magnetically scan over a size of  $100 \mu\text{m} \times 100 \mu\text{m}$  using 10 degree beam line ( $200 \text{ nC/mm}^2$ ). Fig 4.2a shows 13 straight parallel nanolines linked to 5 larger connecting lines, the whole pattern was digitized to  $2048 \times 2048$  pixels with a pixel size of 48 nm. And fig 4.2b is a high resolution SEM image of one of the nanolines featuring a dimension of  $90 \text{ nm} \times 220 \text{ nm}$  in width and height respectively. This straight nano pattern was firstly used for DNA analysis. After PDMS casting, DNA molecules were brought into the PDMS channels and buffer was exchanged through the same channel. The buffer exchanging process was found to affect the stability of a DNA molecule inside the channel. In a later experiment, cross nanolines were introduced for change buffers.

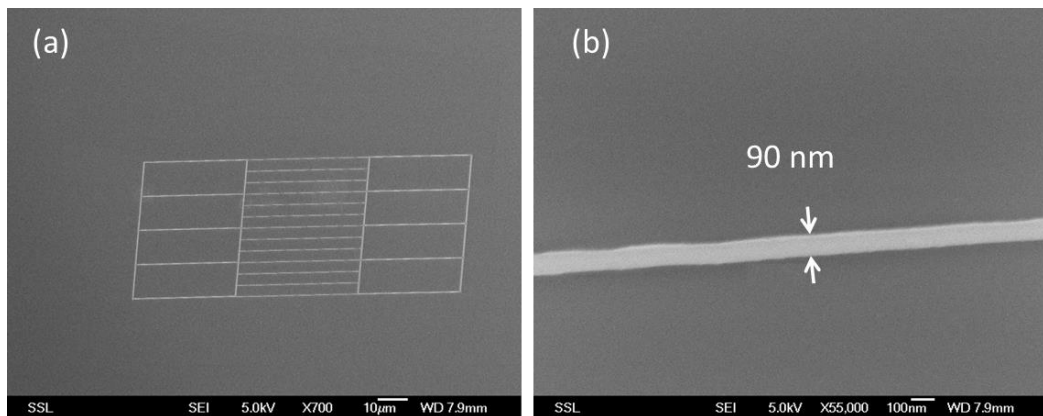


Figure 4. 2 (a) Straight design nanolines fabricated on HSQ (Fox 17/MIBK at the ratio of 1:3); (b) Higher magnification of the Straight nanolines with  $90 \text{ nm} \times 220 \text{ nm}$

In a second experiment, different proton doses were administered using a fresh HSQ resist ( XR 1541, 6%) sample. Figure 4.3 shows the fabrication results for dosage of 50, 100, 150, and 200  $\text{nC/mm}^2$  using 2 MeV proton ( $100 \text{ nm} \times 250 \text{ nm}$ ) in 10 degree beam line. Each line is a single pixel line with a pixel size of 48 nm.

We found that  $50 \text{ nC/mm}^2$  proton dose is sufficient to expose this HSQ resist. And the single pixel nanoline slowly increases in width with increasing proton dose because of the gaussian beam profile. Here the nanoline dimension increase from 110 nm to approximately 190 nm for proton dose of  $50 \text{ nC/mm}^2$  to  $200 \text{ nC/mm}^2$ .

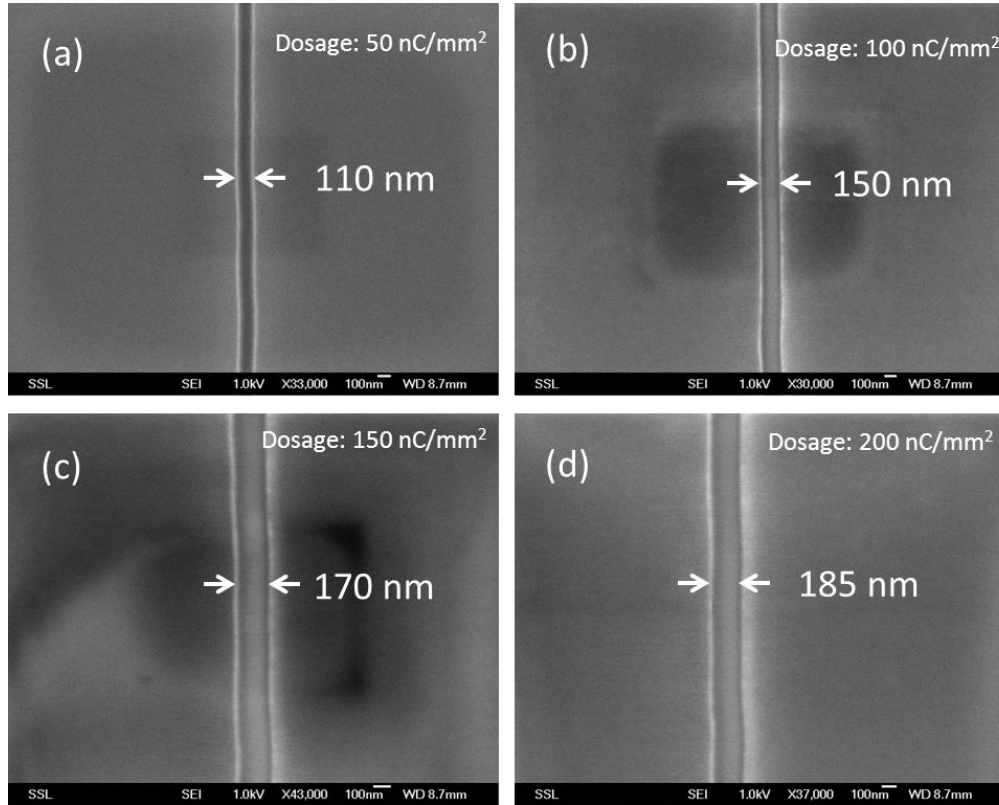


Figure 4.3 XR 1541 nanolines with different dosage (a)  $110 \text{ nm} \times 220 \text{ nm}$  with a dosage of  $50 \text{ nC/mm}^2$ ; (b)  $150 \text{ nm} \times 220 \text{ nm}$  with a dosage of  $100 \text{ nC/mm}^2$ ; (c)  $170 \text{ nm} \times 220 \text{ nm}$  with a dosage of  $150 \text{ nC/mm}^2$ ; (d)  $190 \text{ nm} \times 220 \text{ nm}$  with a dosage of  $200 \text{ nC/mm}^2$

In another experiment, the cross design was fabricated by PBW on HSQ resist. Here two groups of perpendicular nanolines were fabricated so that DNA molecules and buffer solution can be fed from different directions (see fig 4.4). The DNA molecules inside the nanochannels can remain stationary when buffer is

injected. Such a device allows us to isolate, compact and de-compact DNA molecule *in situ*.

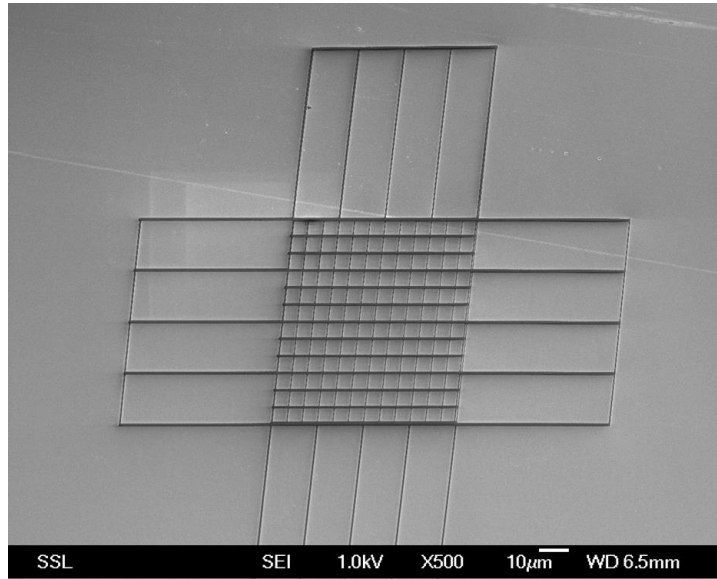


Figure 4. 4 SEM image of cross nanolines fabricated with HSQ (Fox17 dilute with MIBK for 3 times)

A group of crosslines were fabricated with different dimension using different beam lines (see fig 4.5). Fig 4.5a, b and d were fabricated in 10 degree beam line using 220 nm thick HSQ resist (Fox 17: MIBK at the ratio of 1 : 3) with a scan size of 160 μm × 160 μm. All of them are single pixel line in X & Y directions with a pixel size of 78 nm. A 2 MeV proton beam was focused to about 150 nm × 250 nm and fabricated those crosslines. A dose of 600 nC/mm<sup>2</sup> was first tested with HSQ resist and we got a 280 nm × 730 nm crosslines shown in fig 4.5a. We thought that the dose is probably too high for the HSQ resist, because the nanolines are much larger compared to the beam size. So, the proton dose was reduced to 200 nC/mm<sup>2</sup> for the future two experiments. Fig 4.5b and d are the fabrication results with a dimension of 250 nm × 540 nm and 150 nm × 250 nm

respectively. With a similar beam size, fig 4.5b gives a larger nanolines dimension. This could be attributed to few reasons.

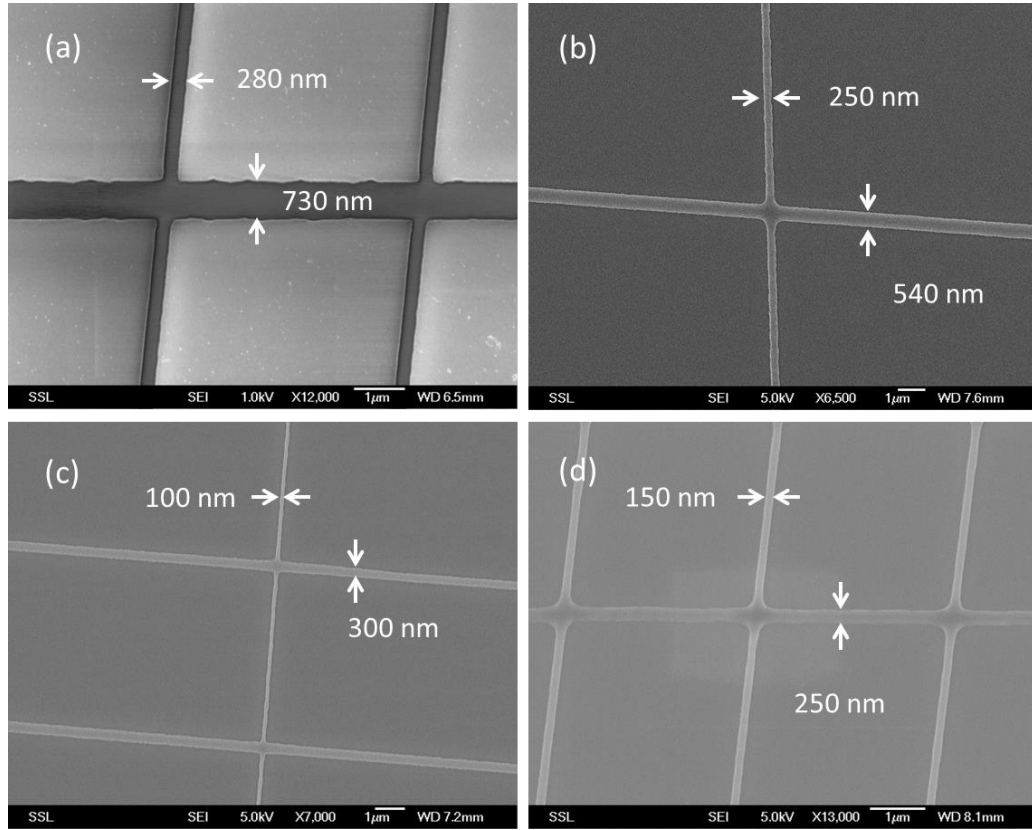


Figure 4. 5 SEM images of cross lines with different Y & X dimension (a) 280 nm  $\times$  730 nm; (b) 250 nm  $\times$  540 nm; (c) 100 nm  $\times$  300 nm; (d) 150 nm  $\times$  250 nm

First reason could be the resist sample is not in the focal plane. As we have discussed in section 3.1, the beam is focused on a nickel grid. Usually resist samples cannot be mounted accurately on the same plane with this nickel grid. So we measure the height difference between the nickel grid and samples using optical microscope. During the fabrication process, the resist sample is brought into the focal plane of the proton beam according to the measurement. This gives an error of (+/-) 10  $\mu$ m. Simulation (Particle Beam Optics Laboratory) result

shows that a height difference of 10  $\mu\text{m}$  will result in a beam increase of 24 nm  $\times$  4 nm in X and Y directions (object slits opening 20  $\mu\text{m} \times$  8  $\mu\text{m}$ , collimator slits opening 200  $\mu\text{m} \times$  200  $\mu\text{m}$ ).

Another reason could be the beam scattering caused by the collimator slits. If the collimator slits are dirty or damaged by the beam, a large scattered beam will also give rise of the features dimension.

The third reason could be that the HSQ resist has a short shelf life time. As we have discussed in section 2.4.3, the contrast and sensitivity of HSQ resist will change over time. For those two experiments, the 150 nm  $\times$  250 nm crosslines were fabricated at June of 2012 and the 250 nm  $\times$  540 nm crosslines were fabricated at October of 2013 with the same bottle of resist. Report shows that the contrast of HSQ will both degrade for PBW and e-beam as the resist ages [143, 178]. The HSQ resist contrast (850 nm thick) drops from 3.2 to 1.7 after 9 month using PBW and it takes almost twice the dose to fully expose the resist, see fig 4.6. The deterioration in the resist contrast will affect the resolution of the written structures.

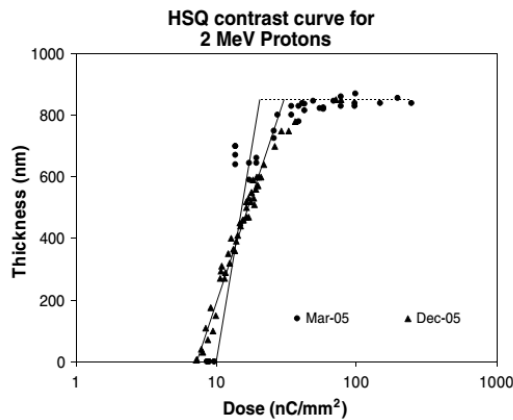


Figure 4. 6 Contrast curve change for a 850 nm thick HSQ, expose with a 2 MeV proton beam

Fig 4.5c shows the crosslines fabricated with 20 degree beam line using another 220 nm thick HSQ resist (XR 1541). A 2 MeV proton beam was focused to about 80 nm × 200 nm and electronically scanned over a size of 100 μm × 100 μm. The crosslines in X and Y directions are single pixel lines with a pixel size of 48 nm. The crosslines carry a dimension of 100 nm × 300 nm which is comparable to the beam size. One more thing we should notice is that the nanolines in X and Y directions are orthogonal using the 20 degree beam line (see fig 4.5c). And the structures fabricated with 10 degree show an obvious tilt. The tilt effect is caused by the misalignment of the magnetic scanning system in X and Y directions. This is not so critical for the nanolines fabrication. However, this tilt effect needs to be considered when we fabricate other structure such as ratchet structure (section 5) using 10 degree beam line. Matlab was used to correct this tilt effect by changing the writing ratchet bmp file.

For the cross nanoline design, the nanolines in X direction were fabricated wider than in Y direction for each of the sample (see fig 4.5). The nanolines in X direction were used for loading DNA molecules after PDMS casting and DNA molecules have a tendency of staying in the wider channel. After PBW, UV (365nm) exposure was performed for aligning microlines with nanolines using SU-8 resist. The fabrication process was discussed in section 3.4.1 for the SU-8 micro structure patterning.

Fig 4.7a shows the line configuration consisting of four microlines and four circular reservoirs. Fig 4.7b shows that the microlines were properly aligned with

nanolines by UV lithography. After PDMS casting and bonding, the micro/nano lines reversed to channels configuration so that DNA and proteins can be injected. A schematic layout of the PDMS device shows in fig 4.7d and DNA molecules were driven into the wider nanochannel by electrophoresis. In the perpendicular direction, a small pressure was used to flush proteins or salt buffer to react with the DNA molecules. One disadvantage for this micro design (see fig 4.7a) is that the pressure applied may affect the DNA molecules inside the nanochannel. So another new microline configuration with two V shape microlines was fabricated to align with nanolines (see fig 4.7c). With this new microline configuration, the proteins can be flushed into the microchannels with a faster speed and with almost no influence on the DNA molecules.

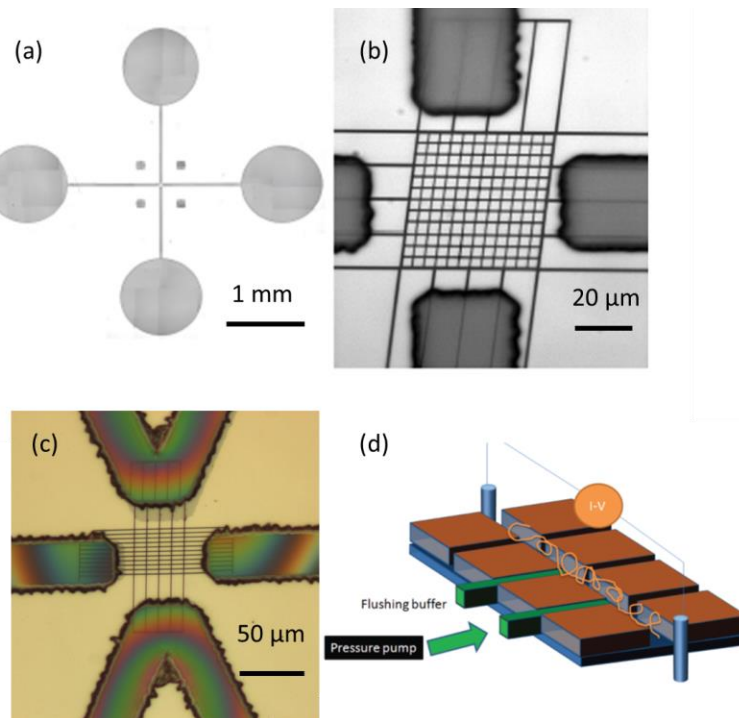


Figure 4. 7 (a) Montage of microlines with reservoirs; (b) Optical image of four microlines aligned with nanolines; (c) Optical image of V shape microlines aligned with nanolines; (d) Schematic layout of how DNA molecules and buffer were brought into PDMS nanochannel

#### **4.1.2 DNA analysis with PDMS cross channels<sup>1</sup>**

Here we demonstrated the study of DNA compaction and de-compaction of pre-compacted DNA, using the 150 nm × 250 nm (height 220 nm) cross channel chip (see fig 4.8b). Protamine was used in the experiment as a compaction agent. That is because protamine is an arginine-rich protein that can bind at multisite with DNA molecules. For the de-compaction experiment, a high ionic strength NaCl was used to unpack DNA molecules because of electrostatic screening effect [19]. T4 GT7 DNA (T4-DNA, 165.65 kbp) molecules at 1 × T buffer (10 mM Tris/HCl, pH 8.5) were investigated in the experiments which were purchased from Nippon Gene, Tokyo. In order to visualize the DNA molecules with fluorescence microscopy it is necessary to stain the DNA molecules with dye. In our experiment, YOYO-1 dye was bought from Invitrogen, Carlsbad, CA. To minimize the affection of DNA molecule in length and charge for bonding with YOYO-1 dye, a low intercalation ratio of 100 base pairs per dye molecule was used [19]. The stained DNA molecules were loaded into two reservoirs connected to the 250 nm wide channels (see fig 4.8a, assume that the two horizontal reservoirs connected with the 250 nm channel). The DNA molecules were subsequently driven into the 250 nm nanochannel by applying a voltage (0.1-10V). Once the DNA molecules are located inside the nanochannels, the electric field was switched off. Protamine or NaCl salt is pipetted into another two vertical reservoirs and exchanged with DNA channels by diffusion (see fig 4.8a).

---

<sup>1</sup> The DNA analysis work was mainly conducted by our collaborator Zhang Ce.

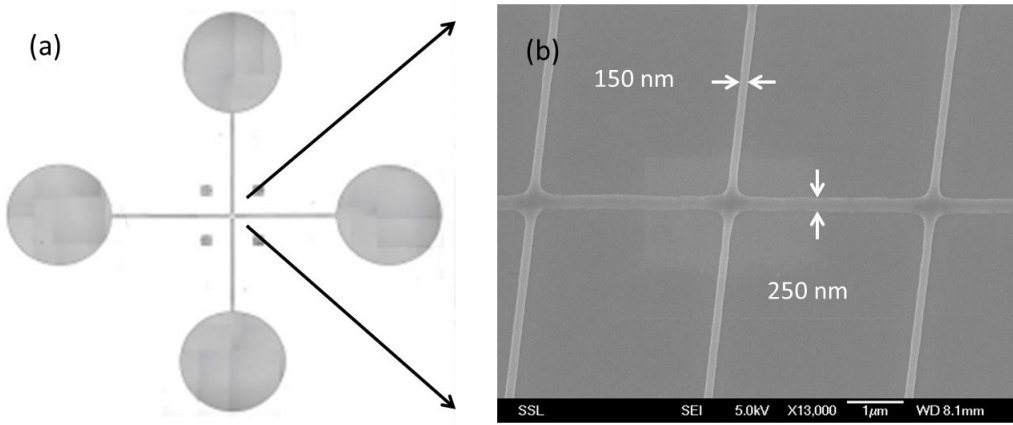


Figure 4.8 (a) Montage of four microlines connect with reservoirs; (b) SEM image of the 150 nm × 250 nm nanolines

Before the DNA compact and de-compact experiment, the protamine diffusion time was studied. In the experiment, the channels and reservoirs were first filled with 1 × T buffer. After this, a buffer containing 1 μM FITC-labelled (fluorescein 5-isothiocyanate, Sigma-Aldrich) protamine was pipetted into the two vertical reservoirs (see fig 4.8a). Fluorescence microscopy was used to monitor the transport of protamine proteins, it takes about 30 s to diffuse through the long microchannel (1.5 mm) to the entrance of nanochannels. With the new V shape microlines (see fig 4.7c), we can get faster and more accurate time control for the release of the buffer admission. Subsequently, protamine proteins were diffused from the 150 nm channels into the wider channels. Fig 4.9 shows integrated fluorescence intensity for an area about 50 μm × 50 μm covering the nanochannels showing increase in fluorescence over time. Result shows that it takes about 3 s for protamine proteins to uniformly diffuse across the nanochannels.

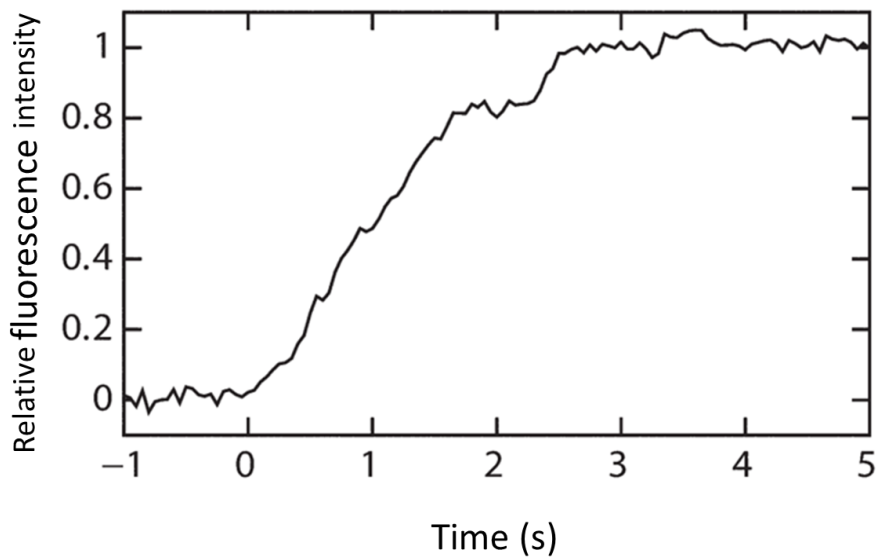


Figure 4.9 Integrated fluorescence intensity as a function of elapsed time

For the first series of experiments, DNA molecules were compacted by 1  $\mu\text{M}$ , 3  $\mu\text{M}$  and 5  $\mu\text{M}$  protamine (fig 4.10). It can be seen that the DNA compaction time depends on protamine concentrations. The final DNA compact size is also related to the concentration of protamine. For 1, 3 and 5  $\mu\text{M}$  protamine the DNA molecules have a final extension of 3, 2 and 0.6  $\mu\text{m}$ , respectively.

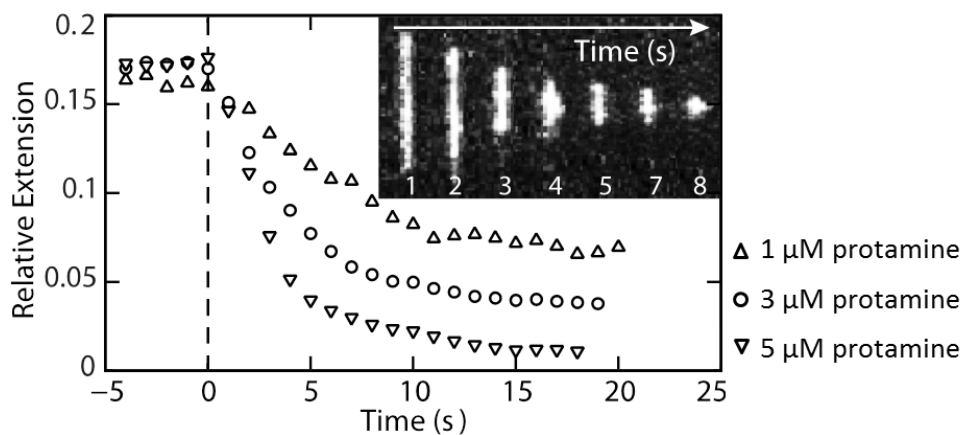


Figure 4.10 T4 DNA/1xT buffer inside 250 nm channel and flushed with 1, 3, 5  $\mu\text{M}$  protamine/1xT from 150 nm channel

In the second series of experiments, DNA molecules were de-compacted by exposing to 100 mM NaCl. DNA was first pre-incubated with 1  $\mu$ M protamine and subsequently brought into the 250 nm nanochannels, following the procedure describe above. The unpacking buffers containing 100 mM NaCl, 1  $\times$  T buffer and different concentrations of protamine were exchanged through the 150 nm channels to interact with DNA molecules. Here three different protamine concentrations (1, 3 and 5  $\mu$ M) were tested for the DNA unpacking. It can be seen that the DNA molecules gradually unfold when exposed to 1, 3  $\mu$ M protamine and 100 mM NaCl buffers (see fig 4.11). In case of 5  $\mu$ M protamine, DNA didn't de-compact within 40 min. Speed of unpacking is also depending on the protamine concentration. The unpack time of 8 and 10 min were observed for 1 and 3  $\mu$ M protamine respectively.

In addition to that, the unpacking time scale is about two orders of magnitude longer compared with the compaction time. The reason may be because of the long incubation time of DNA molecules in protamine. With a longer incubation time, the compact agents will result in more compacted DNA molecules. The extension of the DNA molecules after 24 hours incubation at 1  $\mu$ M protamine is around 1  $\mu$ m. Result shows that the equilibrated extension for compaction inside the channel with the same concentration protamine is around 3  $\mu$ m (see, fig 4.10).

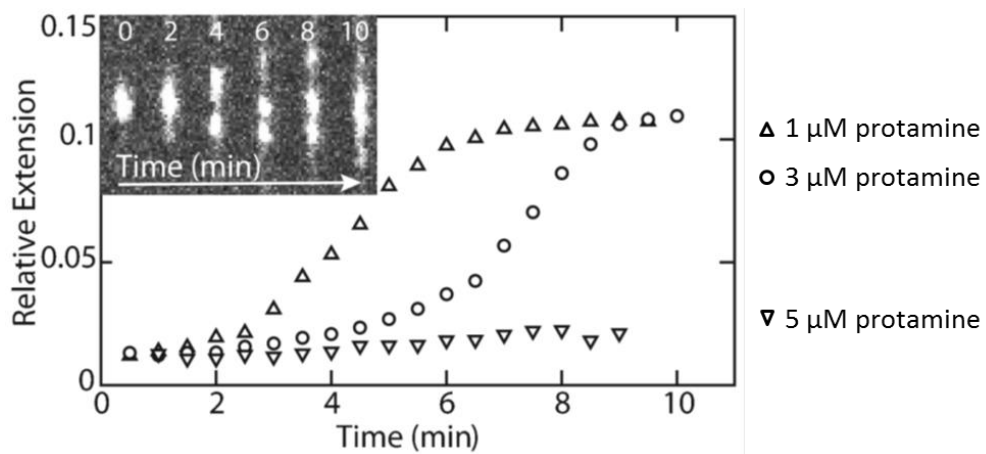


Figure 4. 11 DNA molecules unpacked by flushing 1 mM NaCl/1 × T buffer and different concentration of protamine (1, 3 or 5  $\mu$ M) to the 250 nm DNA channels

## 4.2 OrmoStamp mold and PMMA nanoimprinting

In this section, OrmoStamp molds were fabricated with different type of resists (PMMA, HSQ, SU-8 and SML) by PBW. Following that, OrmoStamp mold was tested by PMMA imprinting for micro/nano fluidic devices fabrication.

### 4.2.1 Thin OrmoStamp mold

For the first PBW experiments, several thin OrmoStamp molds (less than 200 nm) were fabricated with HSQ, PMMA, and SML resists. HSQ, PMMA and SML were spin coated on a silicon substrate with a thickness of 220 nm, 200 nm and 50 nm respectively. Then a 2 MeV proton beam focused down to 30 nm  $\times$  50 nm was used to write lines on the samples with different doses (20 degree beam line). The lines were digitized to 4,096  $\times$  4,096 pixels with a pixels size of 5 nm (using IonScan software) [161], where each line is a single pixel wide in X direction. The line dose of HSQ is  $6.7 \times 10^3$  protons/ $\mu$ m. PMMA and SML have the same

line dose of  $1.9 \times 10^4$  protons/ $\mu\text{m}$ . After exposure, the HSQ sample was developed in a 2.38 % tetramethylammonium hydroxide (TMAH) solution for 60 s, the PMMA and SML samples were developed in an IPA:DI water mixture (7:3 by volume) for 2.5 min. Finally, the samples were rinsed in DI water for 1 min.

Fig 4.12 shows the fabrication results for HSQ, PMMA, and SML resist samples with dimensions (Width  $\times$  Depth) of 30 nm  $\times$  220 nm, 70 nm  $\times$  200 nm, and 60 nm  $\times$  50 nm respectively. Among these three resists, HSQ has the smallest feature size and the line width is the same as the beam size in X direction. The final dimensions of the resists do not only depend on the resolution of the beam, but also depend on other factors like dosage, resist resolution, developer and develop time. These factors will cause the difference in the width of the PBW structures. So the structure size in PMMA and SML are about two times larger than the beam size. With the same dose and same development condition, the width of the SML groove is smaller than in PMMA.

Those three resist molds were then copied with OrmoStamp structures (see fig 4.12 right). The OrmoStamp copies are found to carry almost the same dimension as the resist mold. That means OrmoStamp can transfer structure with high fidelity down to tens of nanometers. For the OrmoStamp structure copy from PMMA, the structure looks a little bit rough (see fig 4.12b right), which could be attributed to the fact that the PMMA resist was probably not developed long enough or got damaged during peeling off the OrmoStamp structure from the PMMA resist.

In the three groups of resist, HSQ shows the best resolution among all of them. So, HSQ is a better candidate for PBW fabrication and OrmoStamp replication, featuring relatively thin structures ( $< 800$  nm). PMMA and SML are positive resist. They are more suitable for Ni molds fabrication which makes them compatible with PBW and Ni electroplating at the sub 100 nm level [138].

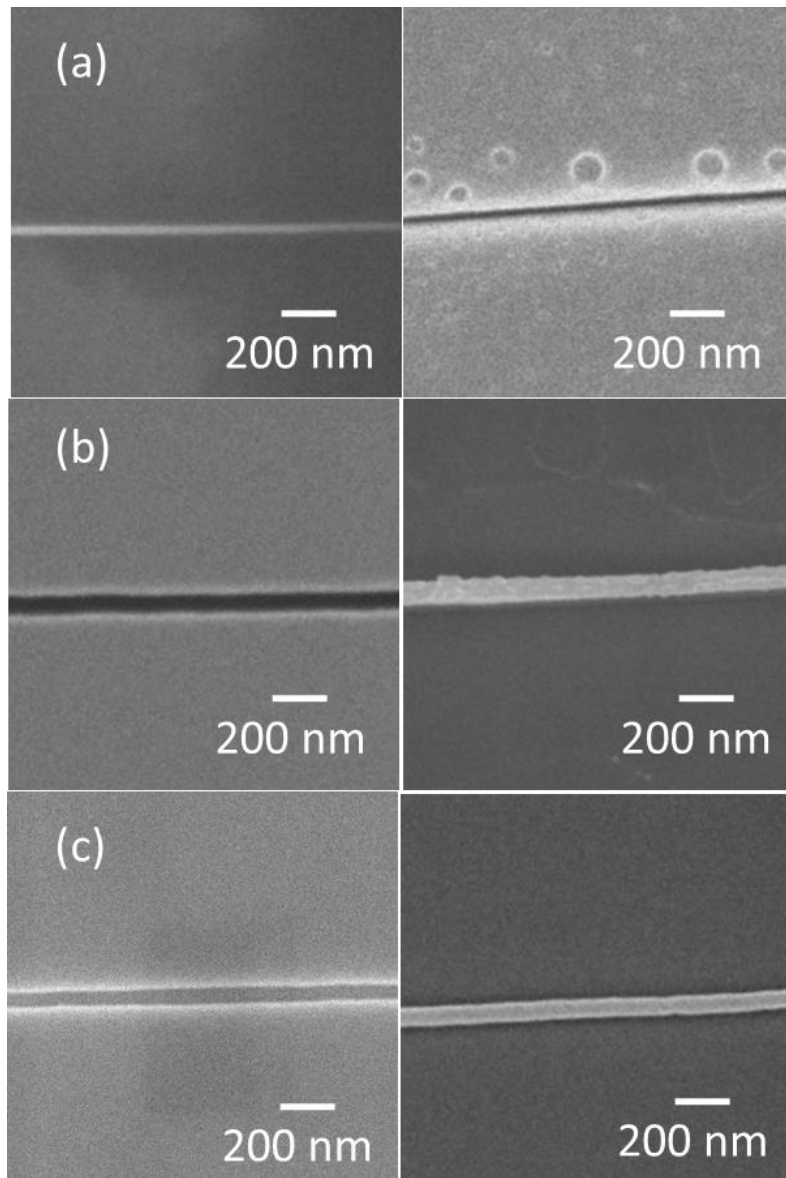


Figure 4. 12 Resist mold and OrmoStamp copy: (a) HSQ ridge (left) and OrmoStamp channel (right); (b) PMMA channel (left) and OrmoStamp ridge (right); (c) SML channel (left) and OrmoStamp ridge (right).

#### **4.2.2 Thick OrmoStamp molds**

To fabricate tall OrmoStamp molds, SU-8 resist (3.8  $\mu\text{m}$ ) and PMMA resist (600 nm thick) were fabricated by PBW. Here, SU-8 (2005) resist was spin coated on a plain silicon wafer at the speed of 6000 rpm and baked for 2 min at 95 °C. PMMA (molecular weight 950k, A4) resist was coated on Au/Cr/Si wafer for two times at the speed of 1000 rpm. Each time after the PMMA coating, the sample was baked at 180 °C for about 90 s. The Au/Cr/Si wafer was prepared by sputtering Cr (chrome) and Au (gold) layer with Ar (argon) plasma based magnetron sputter machine. The system is operated at a high vacuum condition ( $1.9 \times 10^{-6}$  torr) and is used to sputter the Cr and Au layer with a time of 30 s and 60 s respectively. Following that PBW was carried out for the nanostructure fabrication in those samples. These two samples were fabricated at different time while both using a 2 MeV proton beam. The SU-8 structure was first fabricated with 10 degree beam line. Here, a relatively broad beam was focused to pattern the thick SU-8 resist with a beam spot about 300 nm  $\times$  400 nm. The beam was used to scan the single pixel SU-8 lines over an area of 100  $\mu\text{m} \times$  100  $\mu\text{m}$  (pixel size 50 nm and dose 40 nC/mm<sup>2</sup>). After PBW, SU-8 structures were directly developed with SU-8 developer for about 2 min. The fabrication of OrmoStamp structure with SU-8 resist mold follows the discussion in section 3.4.2. The final OrmoStamp structure carries a same geometry with the SU-8 resist mold. Fig 4.13a and b are OrmoStamp ridges copied from SU-8 for two times with dimension of 800 nm  $\times$  3.8  $\mu\text{m}$ . Here we show that the second generation OrmoStamp mold can be copied successfully by coating a thin Teflon film. Proton beam can be used to pattern

thick resist under sub micro resolution. Atomic force microscopy is challenging to perform on these structures. Further characterization need to be carried out in the future for the sidewall roughness of the structures.

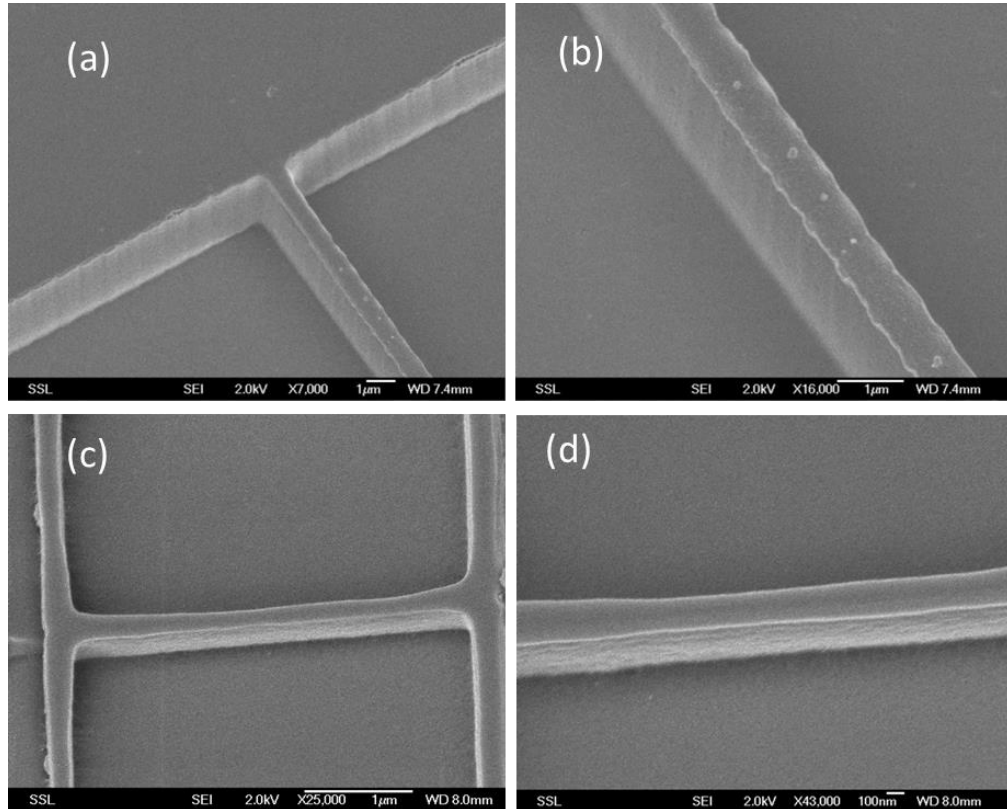


Figure 4. 13 OrmoStamp copy and nickel ridge: (a) and (b) OrmoStamp ridge copy from SU8 after 2 times (c) and (d) OrmoStamp ridge copy from PMMA

For the PMMA structure, the sample was fabricated with 20 degree beam line using a beam focus about  $80\text{ nm} \times 200\text{ nm}$ . A smaller area of  $15\text{ }\mu\text{m} \times 15\text{ }\mu\text{m}$  was scanned for the PMMA single line (pixel size 15 nm). The dose for PMMA structures is  $100\text{ nC/mm}^2$  and developing time is about 1 min using IPA/DI. The OrmoStamp mold was fabricated using PMMA channels through casting. Fig 4.13c and d show an OrmoStamp ridge made from a patterned PMMA. The

dimension of the OrmoStamp is around 200 nm × 630 nm (width × height), corresponding an aspect ratio of 3.

#### **4.2.3 PMMA nanoimprinting with OrmoStamp mold**

PMMA nanoimprinting was tested with an OrmoStamp mold for micro/nano fluidic devices fabrication. All the experiments were done with a commercial nanoimprinter (Obducat Technologies AB, NIL-2-PI 2.5 in. nano imprinter).

In the experiment, the OrmoStamp mold was fabricated via two-time OrmoStamp casting using a HSQ resist mold. A 2 MeV proton beam was used to fabricate this HSQ resist mold with a beam focus around 200 nm × 250 nm (see the HSQ resist mold fabrication in section 4.1). A comparison of the resist mold, OrmoStamp molds and final imprinted PMMA structures are shown in Fig 4.14. The HSQ nanolines (Fig 4.14a) have a dimension of 250 nm × 220 nm (Width × Height). Fig 4.14b and c depict the first and second generation OrmoStamp molds. The second generation OrmoStamp mold was then used for PMMA nanoimprinting. The imprinting temperature and pressure were optimized to 150 °C and 6 bars respectively for 300s. A SEM image of the imprinted PMMA nanochannels is shown in Fig. 14d. We didn't notice obvious OrmoStamp mold deterioration after a dozen imprints, confirmed by optical microscopy observation. The results indicate that OrmoStamp is suitable for PMMA nanoimprinting.

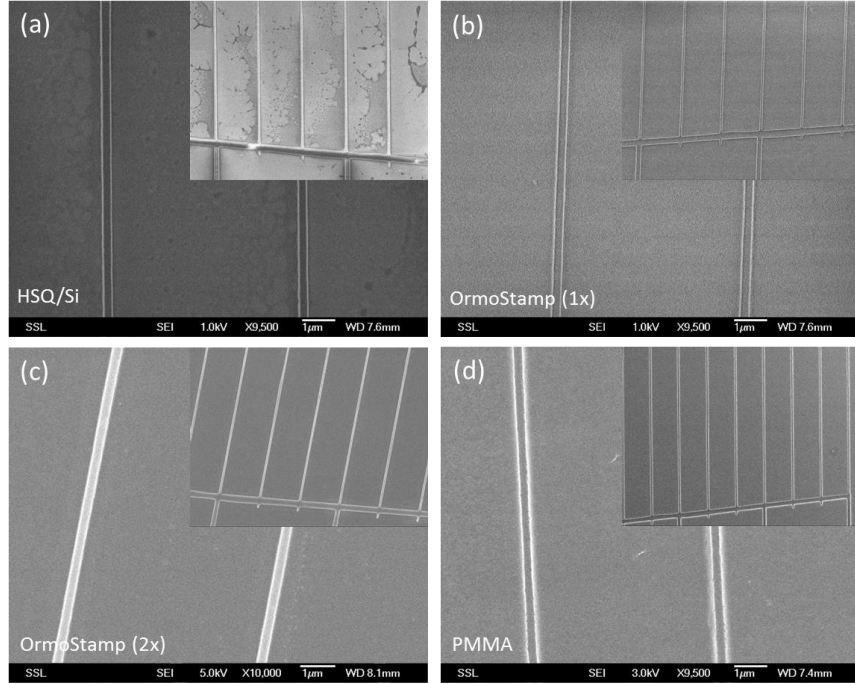


Figure 4.14 (a) SEM image of a 220 nm thick HSQ master, patterned with a 2 MeV proton beam; (b) 1st generation OrmoStamp copied from the HSQ mold; (c) 2<sup>nd</sup> generation OrmoStamp copy; (d) PMMA imprint obtained using the 2<sup>nd</sup> generation OrmoStamp from (c).

After PMMA imprinting, PMMA channels were bonded with another 2 μm layer of PMMA to form enclosed PMMA nanochannels [179]. Fig 4.15a and b show the optical images of the bonded channels. The bonding results show that the channels are not collapsed. Further investigation of the channel dimension will be carried out using technology such as FIB cutting. Different bonding temperatures have been investigated to get optimized bonding. For high bonding temperature (105 ~120 °C), only microchannels survived after the bonding process. The nanochannels were fully collapsed during the bonding caused by the deformation of PMMA material at the temperature over glass temperature. While for the low bonding temperature (80 ~95 °C), we found that the bonding layer easily peels off

since not all the areas are properly bonded. The final bonding temperature and pressure we optimized are 100 °C and 6 bars respectively.

Not only the temperature, but also the sample cleanliness and flatness play a very important role in the bonding process. One of our result shows that a clean and flat PMMA film could be bonded at 80 °C. In our experiment, we failed to maintain a clean sample surface during the fabrication process, so the higher bonding temperature serves as a compromise.

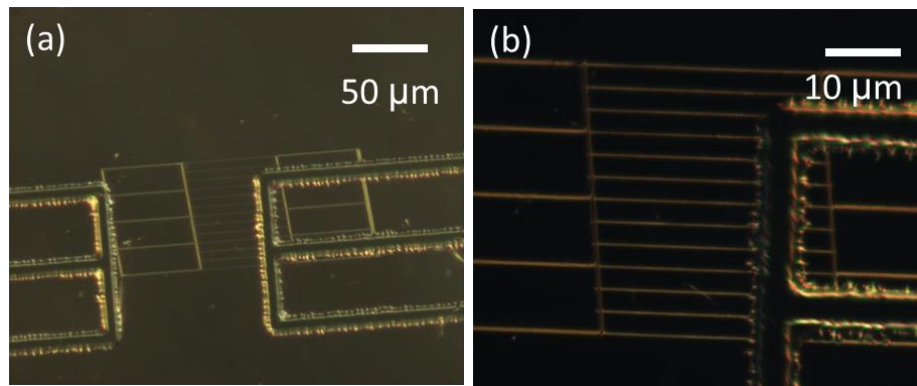


Figure 4. 15 (a) Micro/nano PMMA bonded channels (b) Higher magnification of the bonded channel

#### 4.3 Nickel mold and PMMA imprinting

Apart from resist and OrmoStamp molds, nickel molds were also fabricated for PDMS casting and PMMA nanoimprinting. The advantage of nickel mold is that nickel mold is much stronger compared with the other two types of molds. In our experiment, ma-N 2401 and ma-N2410 were both used for the straight nanolines fabrication.

#### 4.3.1 Nickel mold fabrication results

The results of nickel mold fabricated with ma-N 2410 (600 nm thick) and ma-P 1240 (4  $\mu\text{m}$  thick) resist are discussed in this section. Fig 4.16a shows a scanning electron micrograph (SEM) image of the nano ma-N 2410 lines (PBW) and aligned with micro ma-P 1240 lines (UV lithography). Fig 4.16b is the high magnification SEM of one of the nanolines which indicates a vertical, straight side-wall.

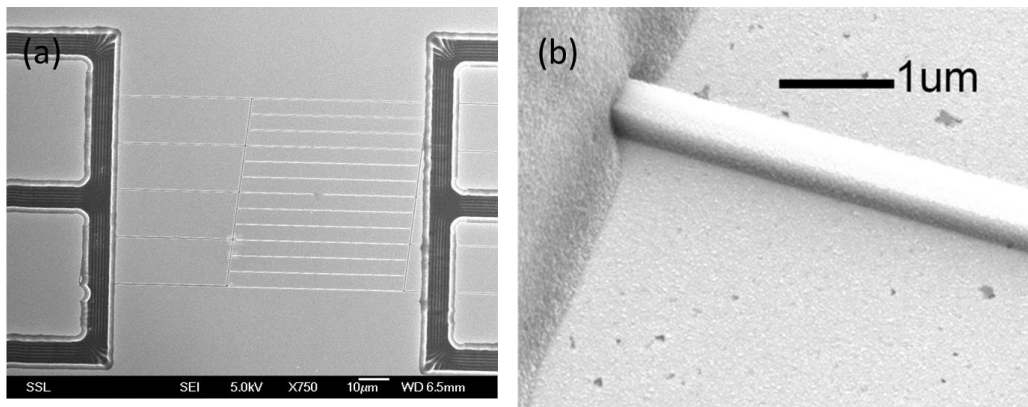


Figure 4. 16 (a) Resist mold nanolines (ma-N 2410) connected with microlines (ma-P1240); (b) ma-N 2410 nanoline

After first time plating, resist inside the Ni stamp is clearly removed by ultrasonic agitation in acetone (see fig 4.17). This suggests that the ma-N 2410 and ma-P 1240 are very promising resists for the combination of electroplating and PBW. Before we employed the second time plating, the Ni stamp should be oxidized by 30% of hydrogen peroxide for about 90 s (see section 3.4.3).

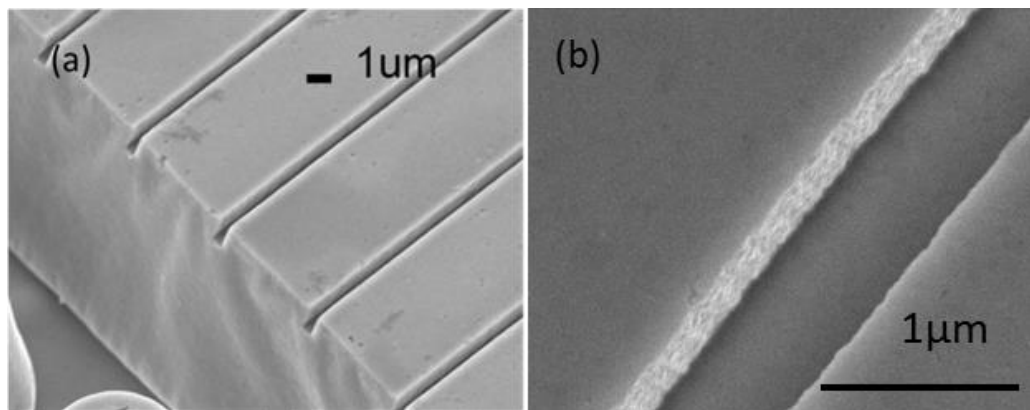


Figure 4.17 (a) and (b) are reverse Ni molds after first time plating

We can then delaminate the final Ni stamp from the first Ni stamp mechanically.

Fig 4.18 shows the SEM images of Ni stamp after re-electroplating with a dimension of  $600 \text{ nm} \times 600 \text{ nm}^2$ . We can see from the image that the top surface is quite smooth while the sidewall is a little bit rough.

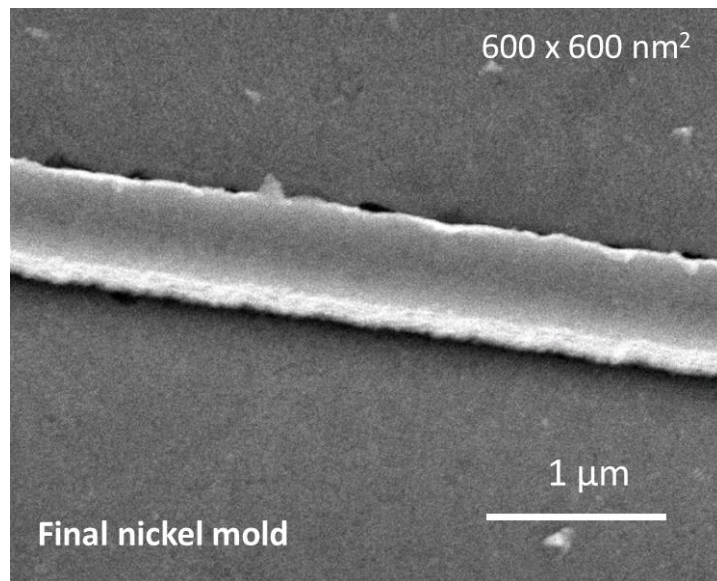


Figure 4.18 Final nickel mold after re-electroplating (tilt 20 °)

Several reasons can cause the roughness. The first reason is the resist mold is rough after PBW. This could be observed from the ma-N 2410 resist mold (see fig

4.19). The second reason could be the plating process. Report shows that electroplating will have little deterioration (4 nm) to the nickel sidewall roughness using our plating system [180].

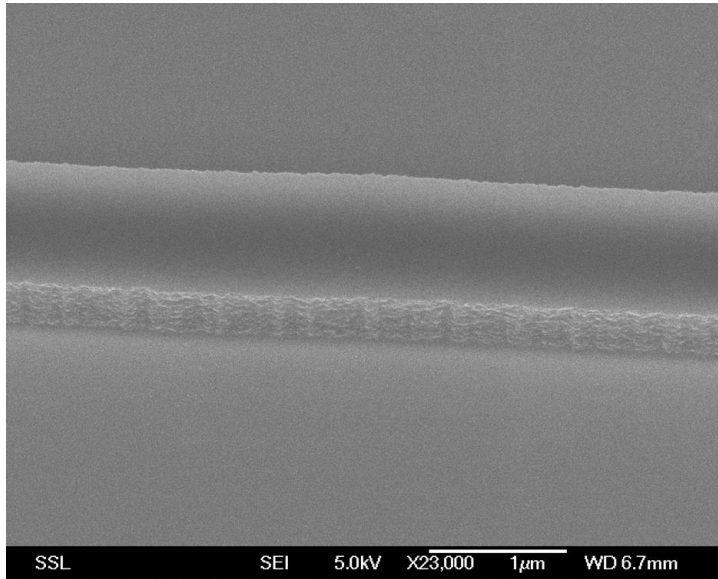


Figure 4. 19 SEM image of ma-N 2410 resist nanolines (tilt 30°)

The third reason could be the deterioration of reverse nickel stamp during oxidization with hydrogen peroxide. The SEM images of the reverse Ni molds (before and after oxidation, after plating) are shown in fig 4.20. Comparing the reverse nickel mold before and after plating (fig 4.20a and b), there is not much difference observed from the SEM images. So, the oxidation process has little or minor damage on the reverse nickel mold. In the future, further characterization with atomic force microscope (AFM) for nickel surface roughness deterioration will be carried out.

In our experiment, a two-time plating process was conducted for the nickel mold fabrication. This means the reverse nickel mold was used to plate another nickel

mold. The main reason for two-time plating is the reverse nickel mold can be reused for several times. Fig 4.20c shows the reverse nickel mold after nickel plating. The SEM image shows that there is almost no damage on the mold except at the channel edge. This damage is most likely caused by the process of separation those two nickel molds. Another reason for two-time plating process is it gives more flexibility in PBW to use either positive or negative resist for desired nano structures.

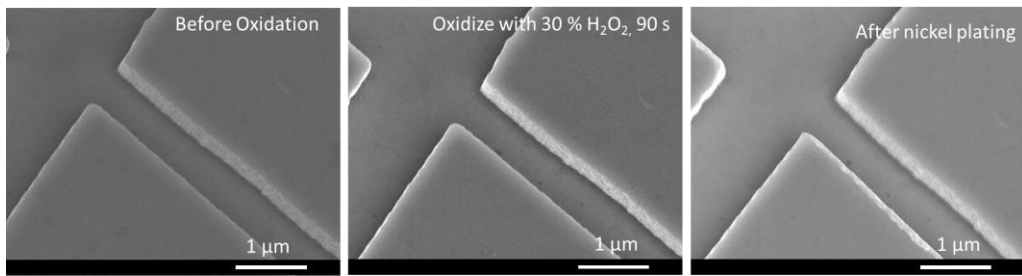


Figure 4. 20 SEM image of reverse Ni molds (a) Before oxidation with hydrogen peroxide; (b) After the oxidation process; (c) After plating process

To fabricate nickel with smaller dimension, ma-N 2401 was used in our experiment. Fig 4.21 shows the PBW result of ma-N 2401 resist with dimension of  $180 \text{ nm} \times 100 \text{ nm}$  (width  $\times$  height). Electroplating and re-electroplating was conducted with this resist mold. Fig 4.22 shows the final nickel mold with disconnected nickel lines. This is because ma-N 2401 resist is difficult to remove at such a small dimension [181]. ma-N resist was remained inside the reverse nickel nanochannel after first time plating. Several methods have been tried to clean the reverse nickel mold. We found that ultra-sonication with acetone or resist remover cannot fully clean the remaining resist. Other test with  $\text{Ar}^+$  plasma (100 W, 10 mins) can remove the resist but will also damage the nickel mold. One

more disadvantage for ma-N 2401 resist is that the side wall is rough, which can be seen from fig 4.23.

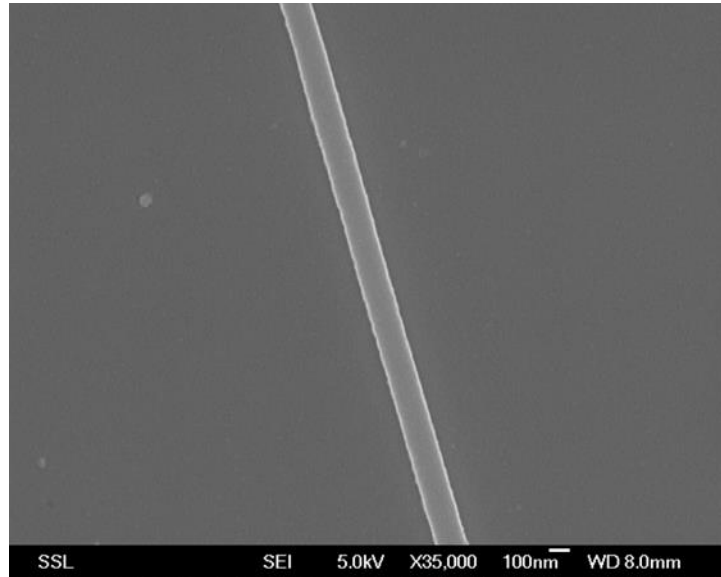


Figure 4. 21 Resist nanoline fabricated with ma-N 2401, 180 nm × 100 nm (width × depth)

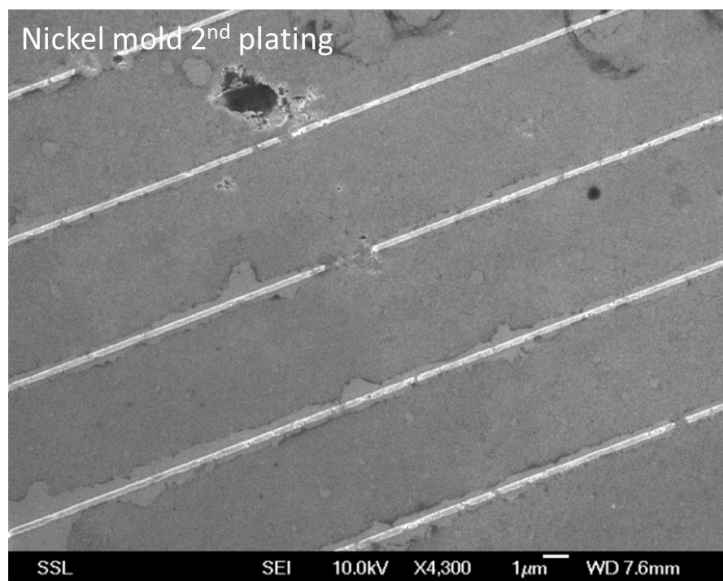


Figure 4. 22 Final nickel mold after two time plating with ma-N 2401

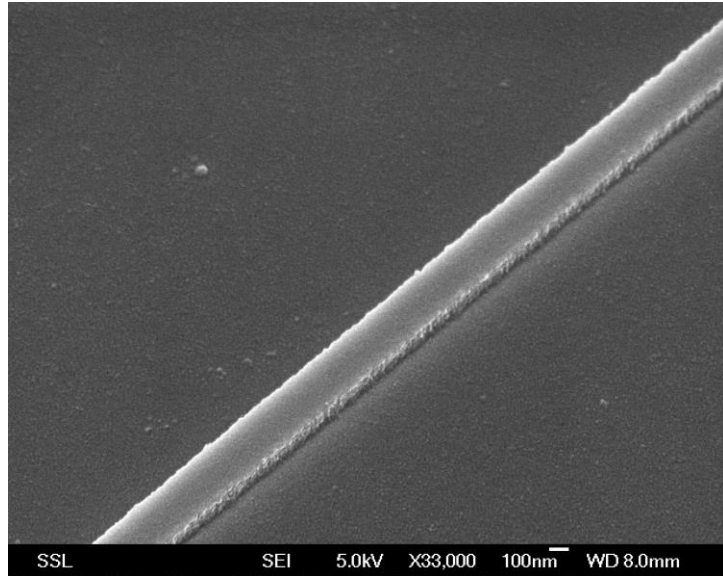


Figure 4. 23 SEM image of ma-N 2401 resist nanolines (tilt 30°)

With PBW, ma-N 2401 can be fabricated down to 60 nm in feature size [181]. However, difficult to remove makes it less attractive for sub 100 nm nickel mold fabrication. To fabricate high resolution nickel mold, we should consider with other resist like PMMA and SML. As discussed in section 2.4, PMMA and SML are two of the candidates with sub 100 nm resolutions as well as easy to be removed after Ni electroplating [182]. Sub 100 nm structures have been achieved successfully by using PBW in our lab for both of them [138]. One more advantage of PMMA resist is that the sidewall roughness was measured to be less than 3 nm after PBW [183]. So, SML and PMMA will be used for the nano nickel mold fabrication with two times nickel plating in future experiments.

#### **4.3.2 PMMA nanoimprinting with nickel mold**

The final nickel mold ( $600\text{ nm} \times 600\text{nm}$ , see fig 4.18) fabricated with ma-N 2410 resist was tested for PMMA nanoimprinting ( $150\text{ }^{\circ}\text{C}$ , 6 bar). After imprinting, PMMA channels were bonded to another  $2\text{ }\mu\text{m}$  PMMA film. Fig 4.24a is an optical image (dark field) of the bonded PMMA channels. The result shows that nanochannels were uniformly bonded.

To demonstrate the suitability of producing functional PMMA nanochannels, T4 DNA molecules were inserted inside one of the PMMA bonded channels, see Fig 4.24b. T4-DNA at  $1\times\text{TE}$  buffer (10 mM Tris, 1 mM EDTA and HCl, PH 8.0) was stained with YOYO at a ratio of 24 base-pairs per dye. Fluorescence microscope was used to observe the T4-DNA molecules inside the nanochannels. Result shows that DNA molecules can be successfully injected into those nanochannels. The T4-DNA molecule inside the nanochannel shows an extension approximately  $54.5\text{ }\mu\text{m}$  which is almost equal to the total contour length of T4 DNA molecule ( $57\text{ }\mu\text{m}$ ). It is most likely that a few DNA molecules are entangled with each other. So there is more than one molecule inside the relatively large nanochannel.

One problem for this bonded chip is that PMMA is hydrophobic. This makes it difficult to drive the fluidic buffer into the nanochannels. Special treatment for PMMA surface is needed to make the channel hydrophilic. In our experiment, PMMA nanochannels and the  $2\text{ }\mu\text{m}$  PMMA film were treated with plasma for 30 s before the bonding process. The plasma treatment will not only increase the bonding strength but also make the PMMA surface hydrophilic. One disadvantage

is that the hydrophilic property of a PMMA surface will disappear in about an hour, so DNA imaging needs to be conducted immediately after the bonding process. In the future, some other chemical treatment will be investigated to optimize the hydrophobicity of PMMA.

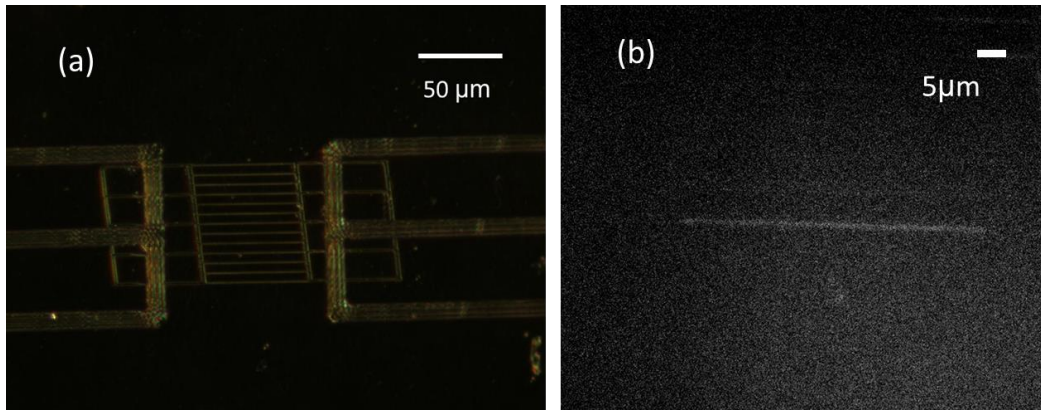


Figure 4. 24 (a) Optical image (dark field) of PMMA bonded nanochannels imprinted with nickel mold (b) Fluorescence image T4 DNA molecules inside the PMMA nanochannels

#### 4.4 Summary and future work of the nanochannel fabrication

Table 4. 1 Summary of three types of fabricated molds

	<b>HSQ/SU-8</b>	<b>OrmoStamp</b>	<b>Nickel</b>
PDMS casting	√	√	√
PMMA imprinting	✗	√	√
Other materials (such as COC)	✗	Tg < 105°C	√

We have successfully fabricated three different types of molds and applied in nanofluidic applications. All of those molds show very high resolution, below 100

nm can be achieved at our lab. We have also realized two-time fabrication using OrmoStamp and nickel molds which allows us to simplify the mold fabrication process. Lastly, we have optimized the PMMA bonding process for PMMA lab on chip devices fabrication and this will serve as an alternative for PDMS fluidic devices.

In the future, firstly we would like to test PMMA and SML resist for high resolution nickel mold fabrication. Secondly, we will characterize the PMMA bonded channel cross section and size by using FIB milling and DNA analysis. Lastly, we want to test the OrmoStamp mold for other materials ( $T_g < 105^{\circ}\text{C}$ , such as COC).

## **Chapter 5. Ratchet fabrication and separation of magnetic particles**

In this chapter, a novel Brownian ratchet system will be introduced, which can be used for separation of superparamagnetic particles. In such a system, the Brownian motion of colloidal particles was rectified by a periodical potential with spatial asymmetry. Firstly, a brief description of the history and the principle of Brownian ratchet, as well as the compact ratchet design itself will be described. Following that, the fabrication and characterization results of the design will be presented.

### **5.1 Introduction to Brownian ratchet**

Historically, the ratchet effect did not get much attention before it was discussed by Feynman in his famous thought experiment on ratchet and pawl [184]. This system consists of a rotational ratchet system which is connected to a wheel with paddles (fig 5.1). The ratchet system is controlled by an elastic pawl such that it can only rotate in one direction (anticlockwise in this system). The whole system is surrounded by thermal equilibrium gas at temperature  $T$ . The idea is to generate work from a heat reservoir with everything at the same temperature. However, the motion of this system is such that every once in a while the pawl lifts itself over the sawtooth and the Brownian motion on the paddle will try to turn the axle backward [185].

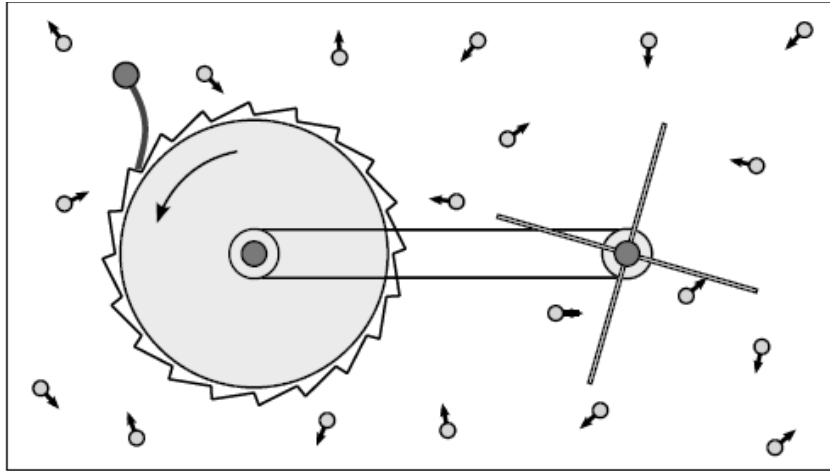


Figure 5. 1 Schematic depiction ratchet and pawl system: ratchet controlled by a soft elastic pawl (left) and connected to wheel paddles (right)

The first ratchet model was introduced by Ajdari *et al* [186] and Magnasco *et al* [187] independently at almost the same time. Their ratchet model consists of a group of sawtooth potential that can be switched on and off periodically. In such a system, the equilibrium of Brownian motion is broken by spatial asymmetry of the sawtooth and the switching of the potential. Thus, colloidal particles in such a system will move towards a certain direction decided by the asymmetry of the potential. The first experimental demonstration of the ratchet effect was described by Rousselet *et al* [188]. Rousselet showed that particles subjected to an asymmetric periodic potential can display a net motion. The authors also mentioned that the speed of motion depends on the particle dimension, suggesting possible applications in particle or biomolecule separation. The first design for particle sieving was proposed by Duke *et al* [189]. Later the separation was realized by Chou *et al* [90] for DNA molecules, see fig 5.2.

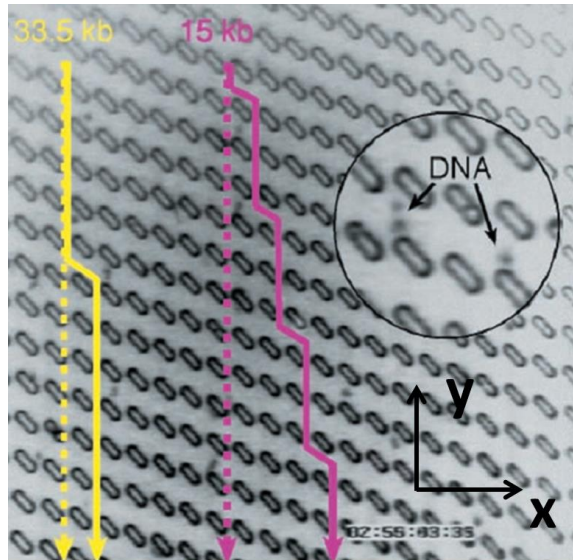


Figure 5. 2 DNA molecules separate by ratchet structure

In their experiment, a group of obstacles were fabricated on silicon nitride ( $\text{Si}_3\text{N}_4$ ) with a dimension of  $1.5 \mu\text{m} \times 6 \mu\text{m}$ . Two types of DNA molecules (15 kbp and 33.5 kbp) were injected inside the chip and driven by electrophoresis force to interact with the obstacles (see fig 5.2). When DNA molecules interacted with the obstacles, the ratchet obstacles would induce a mean displacement in X direction caused by the asymmetric of sawtooth. For different sizes of DNA molecules, the diffusion speeds are also different which allows molecule separation to occur. Compared with conventional technologies, like gel electrophoresis, Brownian ratchets offer some advantages. One of the advantages is that the ratchet separator can operate in a continuous mode. Furthermore, the total chip dimension is also smaller ( $3 \text{ cm} \times 4 \text{ cm}$ ). Continuous separation and smaller chip dimension make it more convenient to integrate the ratchet based separator to lab on chip devices.

## 5.2 Brownian motion

In 19<sup>th</sup> century, Brownian motion had already been observed i.e. particles suspended in a fluid perform random motions. This is caused by the collision of particles with most energetic surrounding fluid molecules.

Here, we only consider Brownian motion in x direction and define  $P(x, t)$  as the probability to find a particle at position  $x$  and time  $t$ . For the case with no external force but only Brownian diffusion,  $P(x, t)$  is described by diffusion equation:

$$\frac{\partial P(x,t)}{\partial t} = D \frac{\partial^2}{\partial x^2} P(x,t) \quad (5.1)$$

And

$$D = k_b T / 6\pi\eta R \quad (5.2)$$

which is the Stokes-Einstein equation for the diffusion coefficient of the particles.

Here,  $k_b$ ,  $T$ ,  $\eta$ , and  $R$  are Boltzmann constant, absolute temperature, viscosity of fluid, and diameter of the particle respectively.

The fundamental solution of the diffusion equation is:

$$P(x, t) = \frac{1}{\sqrt{4\pi Dt}} \exp\left(-\frac{x^2}{4Dt}\right) \quad (5.3)$$

Here, the solution shows that the probability density  $P(x, t_1)$  of a particle at certain time  $t_1$  follows a Gaussian distribution.

Here we consider a single particle in an asymmetric sawtooth structure (with a spatial period  $L$ ), and an external force is switched periodically in y direction to drive the particle, see fig 5.3.

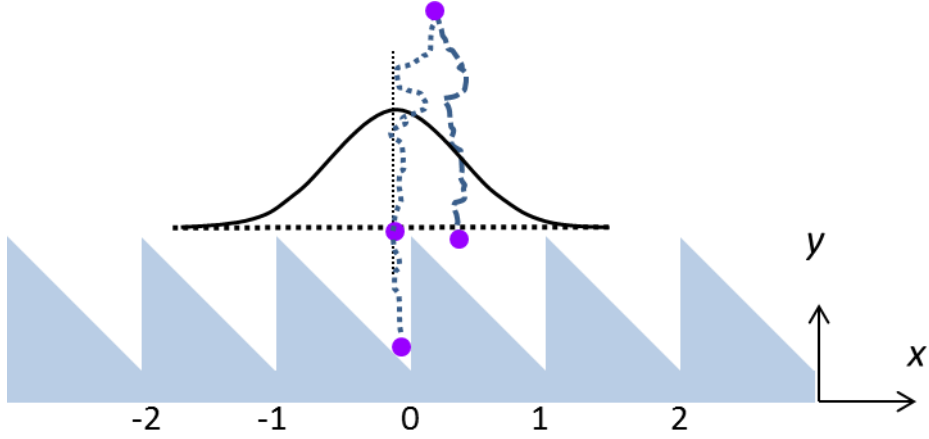


Figure 5. 3 Schematic depiction of Brownian particle driven by a periodical sawtooth potential

In the first place, a particle is trapped at 0 position when applying a force in  $-y$  direction. When switching the force to the  $+y$  direction, a particle will move up along the ratchet. In this region, a particle is affected by the sawtooth structure so that it cannot diffuse freely in  $x$  direction. Above the ratchet, a particle will diffuse freely in  $x$  direction for a time period  $t$  and the probability density follows the Gaussian distribution. When the particle is driven back, the particle can not only exist at the original position 0 but also at the neighboring positions  $+/-1$ . Due to the asymmetry of the sawtooth structure, the probability at position  $+1$  is larger than at position  $-1$ . As a result, there is a net probability flow towards the right. This probability can be calculated by using the following equation.

$$P(+1) = \int_0^1 P(x, t) \, dx \quad (5.8)$$

Therefore, the probability at point  $+1$  is related to the diffusion time  $t$ , diffusion coefficient  $D$  and geometry of the sawtooth. By applying a periodical external force continuously, the particle will diffuse with an average speed directed

towards the  $+x$  direction.

### 5.3 Compact Brownian ratchet

Integration of different functional elements is the ultimate goal of lab on chip devices. To achieve a lab on chip device with smaller overall dimension, a separator with compact dimension is preferred. A separator with channel configuration was introduced by Simon *et al* [91]. This design is almost one order smaller compared to the previous Brownian ratchet separator (see fig 5.2). A schematic illustration of this design is shown in fig 5.4. The separator consists of a single channel made up of two opposing sawtooth walls. The size of the larger sawtooth is designed to be twice of the smaller sawtooth in  $x$  direction and maintained the same size in  $y$  direction. A periodic external force  $F$  is applied to drive the particle (red spot) back and forth to interact with sawtooths.

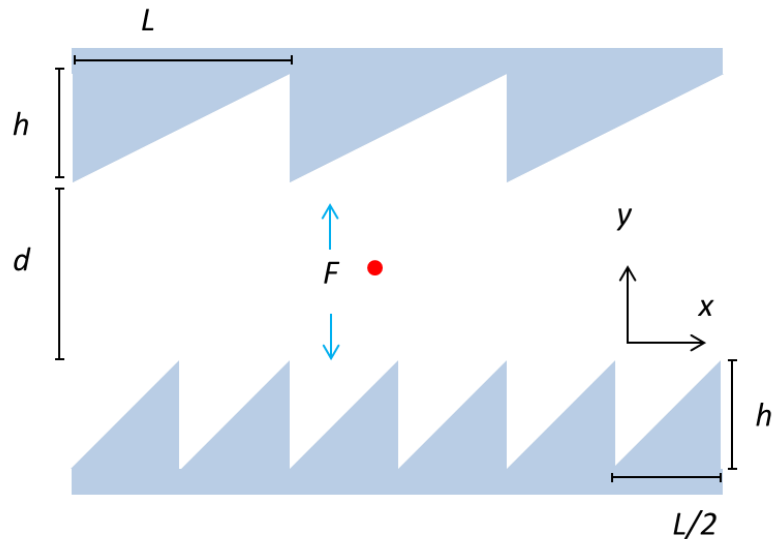


Figure 5. 4 Schematic illustration of the channel separator

The movement of particle inside this separation channel is the superposition of Brownian motion and movement in y direction caused by external force.

A simple explanation of the separation process is as follows. Here, two particles with different movement speed in y direction are discussed. When a periodic external force is applied to drive the particles in y direction, the particles will interact with the small and large sawtooths. When the particles reach either side of the sawtooth wall, they will slide along the walls. The lateral displacement in x direction is either  $-L/2$  (to the left) or  $+L$  (to the right) for the small sawtooth or the large sawtooth respectively. For two particles with different moving speed in y direction, we can control that the slow particle will only interact with the small sawtooth and the fast particle will interact with both sawtooths. As a result, the slow particle will have a lateral displacement of  $-L/2$  while the fast particle will have a lateral displacement of first  $-L/2$  and then  $+L$ . So, those two different speed particles will move in opposing directions in x direction.

## 5.4 Ratchet fabrication

In our experiment, this single ratchet channel was fabricated by PBW for particle separation. The large sawtooth was fabricated with a dimension of  $10 \mu\text{m} \times 20 \mu\text{m}$  ( $h \times L$ ) and a distance of  $40 \mu\text{m}$  ( $d$ ). Here, electromagnets were used to drive superparamagnetic particles in y direction. Magnetic components have been widely used in microfluidics for trapping and moving paramagnetic particles [190, 191]. Two electrode channels were fabricated beside this ratchet channel and later were injected with solder electrodes to supply with a current (discussed in section

5.4.1). The electrodes were fabricated with a dimension of  $27 \text{ } \mu\text{m} \times 100 \text{ } \mu\text{m}$  (height  $\times$  width) and with a length of 8 mm. Moreover, the gap between the electrode and separation channel was controlled to be around 20  $\mu\text{m}$ . Therefore, we can simply assume that the magnetic field  $\mathbf{B}$  (T) generated by the current is determined by the right-hand-rule [192]. The equation is described as a function of the distance  $y$  from the axial center of the electrode wire. Here, we only consider the particle movement in  $y$  direction.

$$B = \mu_0 \frac{I_{\text{wire}}}{2\pi y} \quad (5.9)$$

$I_{\text{wire}}$  is the current passing through the electrode,  $\mu_0$  is the permeability of free space and  $y$  is the vertical distance from the center of the electrode to particle. Next, the force  $\mathbf{F}$  (N) on a superparamagnetic bead is determined by the magnetic field gradient [193].

$$\mathbf{F} = \frac{V\chi}{\mu_0} \nabla(\mathbf{B}^2) \quad (5.10)$$

Here,  $V$  is the volume of the particle,  $\chi$  is the magnetic susceptibility of the magnetic particle. Combining these two equations, we can get the value of  $\mathbf{F}$  (N) described by the current and the distance  $y$ .

$$\mathbf{F} = V\chi\mu_0 \frac{I_{\text{wire}}^2}{2\pi^2 y^3} \quad (5.11)$$

Here, the direction of the  $\mathbf{F}$  (N) is towards the axial center of the electrode. From this equation, we can see that the force applied on the particle can be increased either by increasing the current  $I_{\text{wire}}$  or decreasing the distance  $y$ . To get a better control of the particles, the separation channel should be fabricated as close as

possible to the electrode channels. Furthermore, the microelectrodes should be wide enough to pass through a relatively high current.

#### **5.4.1 Fabrication process**

Here PBW was used to fabricate this compact ratchet for particle separation. The procedure is as follows. Firstly, a Si wafer was cleaned and baked at 150 °C for 10 min. In the experiment, SU-8 2025 was spin coated at a speed of 3000 rpm for 30 s (approximately 27 µm thick). The sample was then baked at 65 °C for 3 min and 95 °C for 5 min respectively on a hotplate. After this, proton beam writing (2 MeV proton using 10 degree beam line) was carried out to fabricate the compact ratchet design (see fig 5.5a, using ‘bmp’ file) over a size of 320 µm × 320 µm. A SRIM simulation result shows that half of the lateral spread for 2 MeV protons penetrating 27 µm SU-8 is around 0.6 µm. We have discussed about the tilt effect for 10 degree beam line in chapter 4. It is not important for the nanoline fabrication because we don’t care much about the angle of those perpendicular nanolines. In the ratchet experiment, the shape of fabricated structure will affect the separation result. So, the tilt effect was corrected using Matlab software. Fig 5.5b shows the Matlab generated ‘bmp’ file which was tilt for 6.5 degree toward y direction.

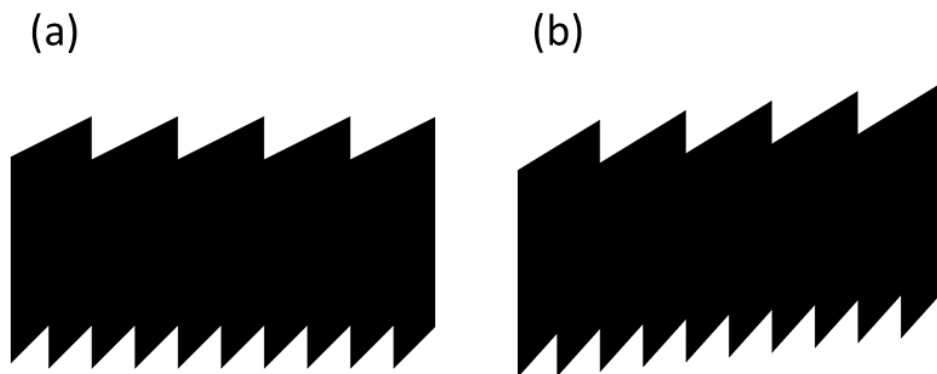


Figure 5. 5 (a) Ratchet ‘bmp’ file before tilt correction (b) Ratchet ‘bmp’ file after tilt correction

Following that, linescan was also conducted to fabricate two long feeding channels and electrode channels. The linescan is referred to that the proton beam is magnetically scanned in one of the directions while stage is moved at a designed speed in the perpendicular direction. By defining the starting and finishing point of the stage movement, a centimeter long micro/nano line can be fabricated. The feeding channels are connected to the left and right of the ratchet channel which is used for guiding fluid and particles into the ratchet channel (see fig 5.6, red: ratchet channel). Two electrode channels were fabricated just next to the ratchet channel (purple: electrode channel).

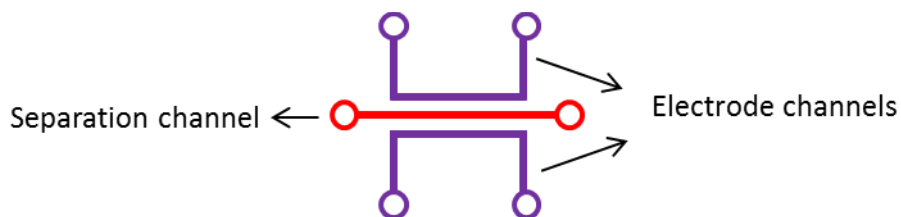


Figure 5. 6 Schematic illustration of the separation device with separation channel and two electrode channels (purple: electrode channel; red: ratchet channel)

After PBW, the SU-8 sample was developed using SU-8 developer for about 5 min. Teflon was spin coated on this SU-8 mold to protect the stamp and baked at 120 °C for overnight. After PDMS casting and plasma bonding with a glass slide, solder electrodes were injected by our collaborator from chemistry department. The fabrication process for the solder electrodes follows a procedure reported by Whitesides *et al* [194]. A solution of 0.1 M 3-mercaptopropyltrimethoxysilane in acetonitrile was first injected into the electrode channels to increase the continuity of the solder electrode. Wait until the electrode channels were dry at room temperature (~25°C). A slab of solder (52% Indium, 48% Tin, The Indium Corporation of America) was put on the top of the electrode channels inlet and baked in oven for 15 min at 130 °C (to melt the solder into liquid). After that, a pre-heated glass syringe (Cadence Science, Micro-Mate 20 cc with metal luer lock tip) was used to push the liquid solder into the channels. Fig 5.7 shows the fabrication result for one of the SU-8 mold and PDMS device with two electrodes.

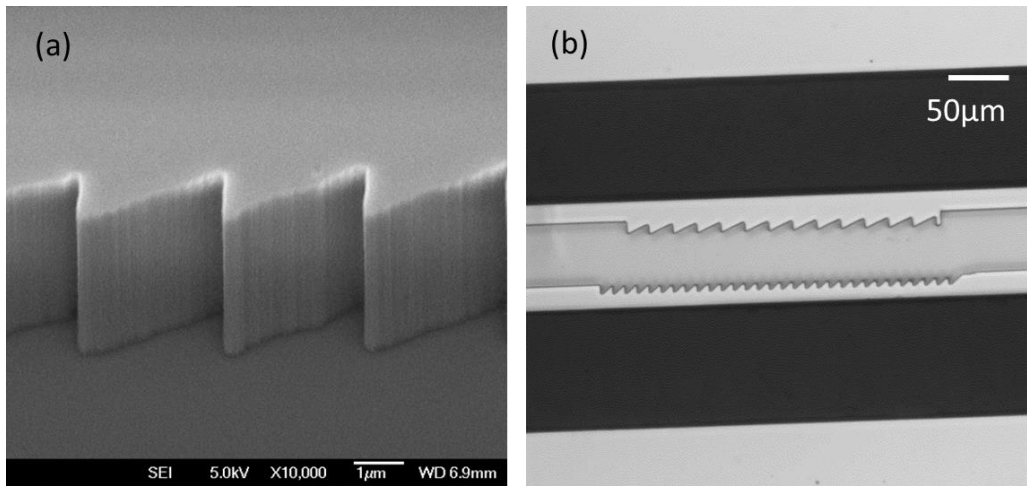


Figure 5. 7 (a) SEM image a 10  $\mu\text{m}$  tall ratchet mold fabricated with PBW, (b) Optical image of PDMS device with solder electrodes (top view)

For ratchet separation, polymer based particles (2.6  $\mu\text{m}$  COMPEL MAG microspheres, Bangs Laboratories) and  $\text{SiO}_2$  based particles (1.51  $\mu\text{m}$   $\text{SiO}_2$  MAG, MicroParticles GmbH) were chosen to test this ratchet design. The polymer based magnetic particles are composed of polymer matrix with nanometer-sized iron oxides. They have a density close to polymer ( $\sim 1.1\text{-}1.2 \text{ g/cm}^3$ ) and can respond to magnetic field rapidly and efficiently. For the smaller particles, silica particles were used. The silica particles have a higher density ( $>2.4 \text{ g/cm}^3$ ) compared to the polymer beads. The particle matrix consists of silica with homogeneously incorporated nanometer-sized iron oxides. Both of them are superparamagnetic particles. In the absence of external magnetic field, the magnetization of nanometer-sized iron oxides can randomly flip direction under the influence of temperature. The average magnetization of a particle appears to be zero. While the particle is under magnetic field, the magnetization of iron oxides can be aligned. The reason we used superparamagnetic particles instead of magnetite particles is to avoid unnecessary aggregation caused by magnetization. Superparamagnetic particle will aggregate under relative strong magnetic field (around 100 mT or above) [195]. In our experiment, the estimated magnetic field is around 1 mT (according equation 5.9) which is small enough to avoid aggregation.

## 5.5 Estimation of the magnetic force

According to equation 5.11, there are two factors which will affect the force experienced by magnetic particles. They are the current  $I_{\text{wire}}$  that passes through

the electrode and the distance  $y$ . In our ratchet design, the distance ranges approximately from 70  $\mu\text{m}$  to 110  $\mu\text{m}$ . According to our tests, the solder electrodes can carry a maximum current about 0.6 A. Therefore, the safe currents of 0.4 A and 0.5 A were usually used for the experimental tests.

The magnetic susceptibility of the polymer based particle is around 0.36. An estimate of the maximum magnetic force experienced by these polymer particles is around 0.15 pN. Our experiments show that the 2.6  $\mu\text{m}$  polymer particle can respond quickly to this magnetic force. However, for the smaller silica particle (1.51  $\mu\text{m}$ ), the force is less and it is subjected to more Brownian motion resulting in a slower movement in  $y$  direction. This is because of the smaller volume and the higher density of the silica particle. One problem for this is that for even smaller size particles, such as submicron particles, the magnetic force is probably not enough to drive the particles. Experiments show that, the magnetic force applied on the 0.9  $\mu\text{m}$  magnetic particle is just comparable to the Brownian motion force. In that case, the Brownian motion of a particle is large enough to cross the smaller sawtooth, and this will result in the failure of the ratchet effect. To separate particles at submicrometer dimension using the ratchet design, one possible way is to use particle with higher magnetic susceptibility such as ferromagnetic particles (iron or nickel), such that the magnetic force can be increased by 3 or 4 orders of magnitude. The disadvantage is this may induce aggregation discussed above. Another possible way is to scale down the total chip dimension that will reduce the distance  $y$ .

## 5.6 Experimental result

During the particle separation, the current needs to be switched between the two electrodes periodically to drive the particles (see fig 5.8).

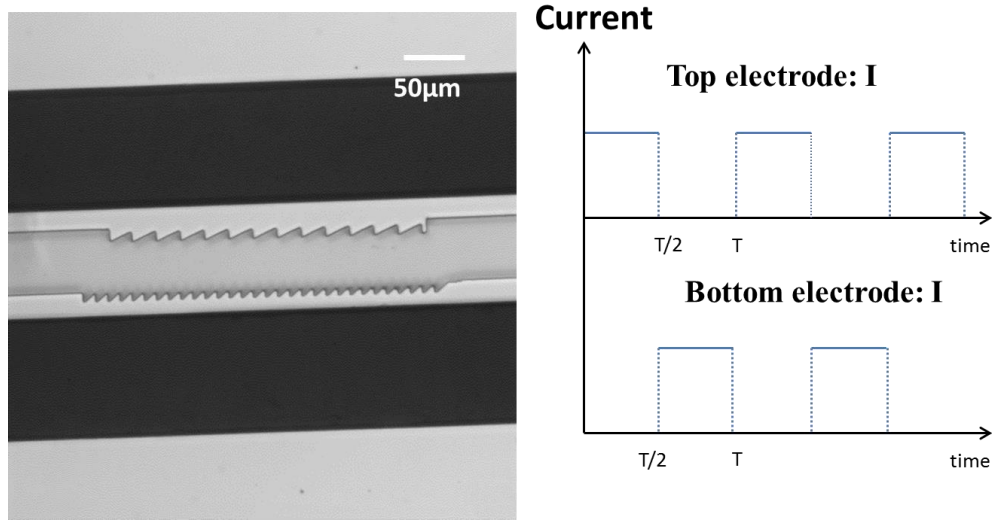


Figure 5. 8 (a) Optical image of the PDMS chip (b) Current applied to these two electrodes

For the first half of the cycle ( $0 \sim T/2$ ), the current was applied to the top electrode. For the second half of the cycle ( $T/2 \sim T$ ), the current was applied to the bottom electrode. A system was built to control and switch the current automatically (see fig 5.9). The system consists of a Hi-speed USB Carrier (NI USB-9162), a relay (Type 6012), a power supply and a voltage amplifier. The power supply can provide current with an output range of  $0 \sim 2$  A. This is sufficient for our separation device with a maximum current of 0.5 A. An on/off square profile voltage controlled by labview program was generated by the computer, USB Carrier, and voltage amplifier to control the relay switch. When a voltage (around 200 V) is applied to this relay, the power supply has an access to for example left electrode (see fig 5.9). On the contrary, when no switch voltage

is applied to the relay, the power supply has an access to the right electrode. The switch voltage has a period time of  $T$  and time interval of  $T/2$  for the on and off voltage respectively. The time period and interval can be easily adjusted in the labview program.

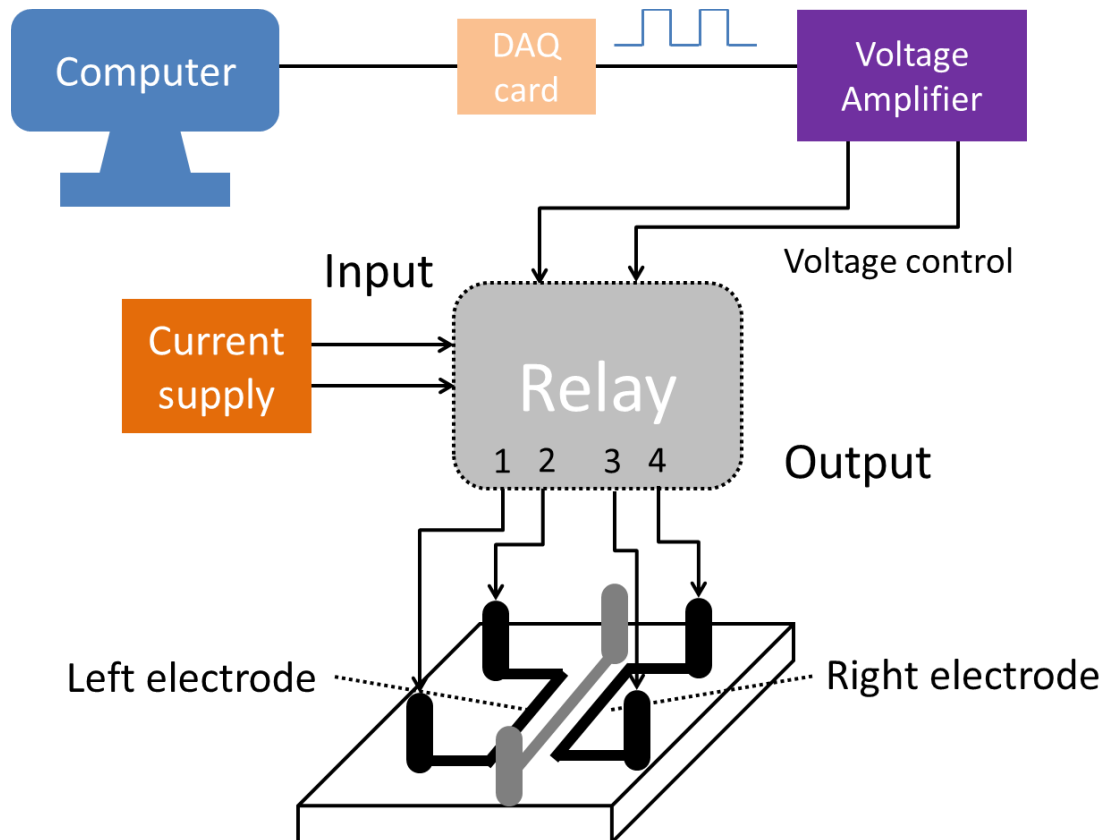


Figure 5. 9 Current control system used to control and switch the current

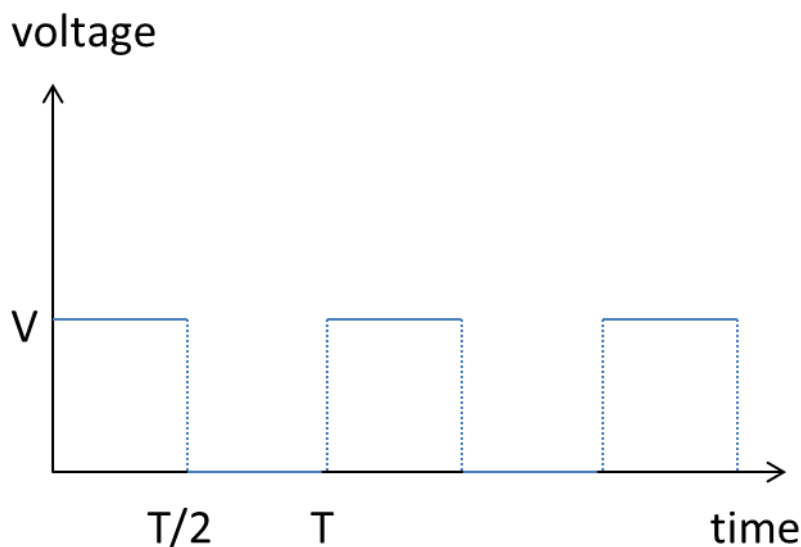


Figure 5. 10 On/off voltage profile control by the labview program

During the test of the ratchet devices, several major problems affected the experimental test. Here, we will give a brief discussion of how we solved these problems.

First problem was how to connect the micro electrodes to the power supply. Previously, silver paint was used to stick the two micro electrodes to the electric wires directly. However, the connection of electrodes and electric wires were found to be fragile. Most of the time, the sample could only be used for a few times or only once. To solve this problem, four Cr/Au electrodes (sputter for 30 s /120 s) were sputtered to the glass slide before bonding with PDMS chip (see fig 5.11). After injecting with solder electrodes, the Cr/Au electrodes were then connected to electric wires by using silver paint.

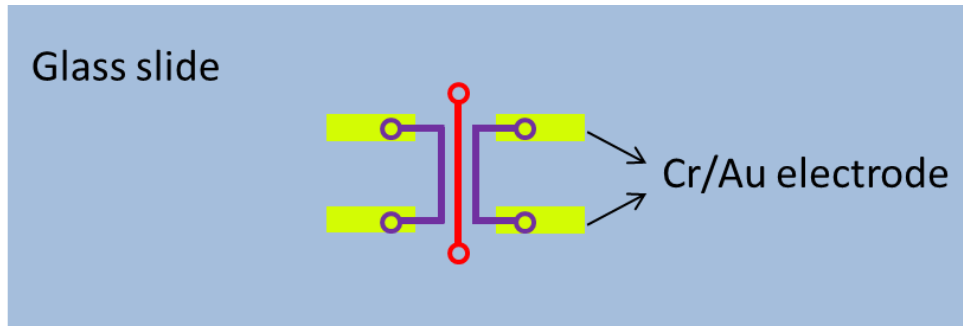


Figure 5. 11 Illustration of glass slide sputtered with four Cr/Au electrodes and bonded with PDMS channels (purple: electrode channel; red: ratchet channel)

The second problem was that the fluid in the separation channel was always flowing. The ratchet effect will be affected if fluid has a net movement. To stop the movement, another channel on top of the PDMS chip was made to connect the separation channel (see fig 5.12). When the separation channel and the top PDMS channel were both filled with fluid, it works like a communicating vessel and there would be no fluid flow. The top PDMS channel was fabricated with a flat PDMS and the channel was cut by knife with a width about 1 to 2 mm. When doing experiments, this PDMS channel was put on top of the PDMS chip and filled with DI water. With this device, the fluid could maintain motionless for more than half an hour.

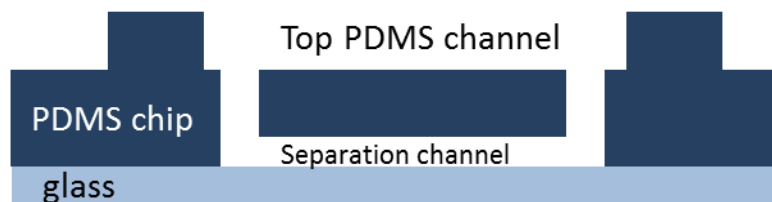


Figure 5. 12 Schematic figure of PDMS chip with one extra top PDMS channel connected with the separation channel

Third problem was particle aggregation and sticking to glass. For polymer based magnetic particles, they tend to aggregate together in either DI water or biological buffer (TE, PBS buffer). This is probably because the polymer particles are hydrophobic. Therefore, the aggregation can reduce the surface area of the particles and reduce the surface energy as a result. We could not find a way to completely eliminate particle aggregation. One compromised solution was to dilute the polymer particles so that they would not have a chance to meet together, but as a result, the throughput will also be compromised. For the silica particles, there is no obvious aggregation. The problem is silica particles would stick to the glass floor inside the separation channel. In our experiment, soapy water was used and we found that this could help in the release of silica particles.

In the separation process, silica and polymer particles were mixed evenly with soapy water with a dilution of 1 : 200 and 1 : 100 respectively. Several groups of experiments were conducted with different time periods and currents. The experiments were observed and video was taken using a microscope (Olympus IX71 inverted microscope).

For the first experiment, a period of 50 s and a current of 0.4 A were used. When applying the current to either one of the electrodes, polymer and silica particles will move in y direction (see fig 5.13). The movement speeds were measured to be approximately 3.5  $\mu\text{m/s}$  and 1.3  $\mu\text{m/s}$  for the polymer and silica particles respectively. When the polymer and silica particles interact with the smaller sawtooth, we found that the particles tend to get stuck to the smaller sawtooth. It takes some time to pull the particles out especially for the silica particles (around

15 s). This is because the magnetic force on the silica particles is relatively weak. Therefore, a relative long time period (50 s) was first tested. Here, the polymer particles could interact with both the small and large sawtooths which will result in a positive displacement in x direction. For the silica particles, they could only interact with the small sawtooth which will result in a negative displacement in x direction (see fig 5.13).

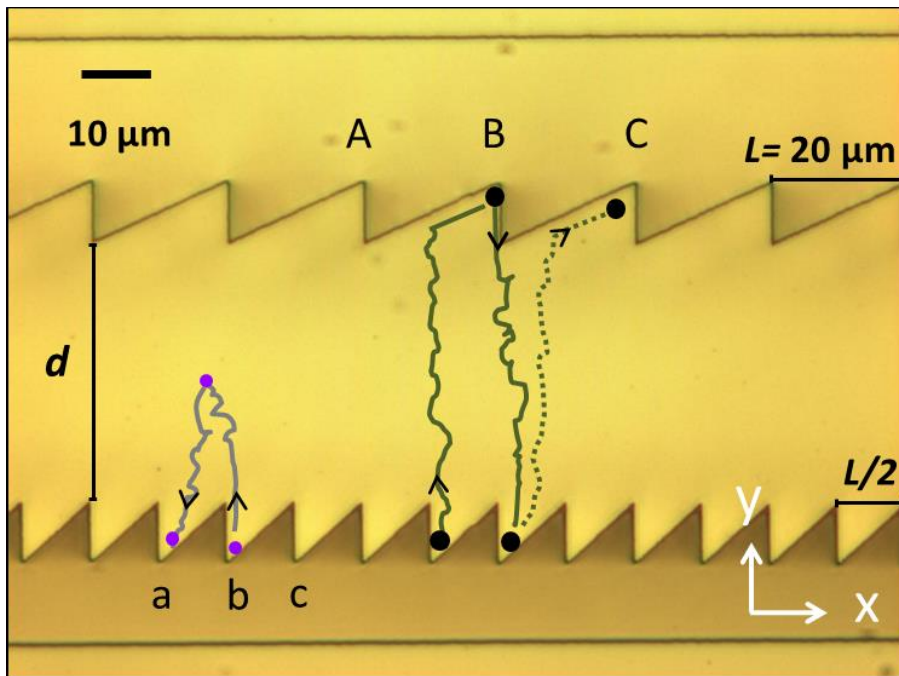


Figure 5. 13 Schematic describe of polymer and silica particles movement in one cycle of experiment

A simple explanation of the movement in x direction is as follows. The mean square displacement for a free diffusion particle is related to the diffusion coefficient and time.

$$\Delta x^2 = 2Dt \quad (5.9)$$

This can give an estimate of diffusion distance over time. In our experiment, the diffusion coefficient can be calculated by  $D=kT/6\pi\eta R$ . Here  $\eta$  is viscosity of water (about  $0.001 \text{ Pa} \cdot \text{s}$  at  $20^\circ\text{C}$ ). The diffusion coefficient of the polymer beads and the silica beads are  $0.165 \mu\text{m}^2/\text{s}$  and  $0.286 \mu\text{m}^2/\text{s}$  respectively. When applied with  $0.4 \text{ A}$  current, the diffusion time for polymer and silica particles would be around  $11 \text{ s}$  and  $20 \text{ s}$  respectively. An estimate of the diffusion distance for polymer and silica particles are around  $1.9 \mu\text{m}$  and  $3.4 \mu\text{m}$  respectively. The diffusion distance is relative small compared to the size of the large or small sawtooth ( $20 \mu\text{m}$ ,  $10 \mu\text{m}$ ). This means that the silica particle starting at origin position **b** will most likely go to either position **b** or **a** after one cycle (see fig 5.13). Same case for the polymer particle, a particle starting at position **B** will most likely go to either **B** or **C** after one cycle. These can be further proved by the experimental results.

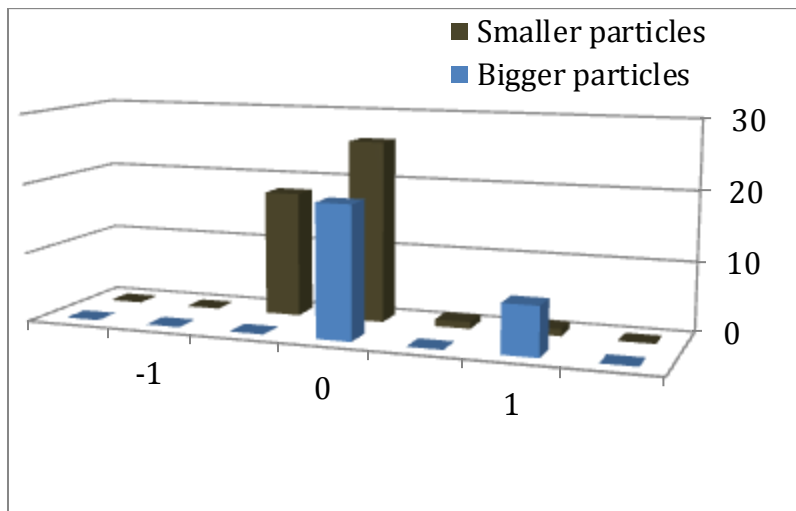


Figure 5. 14 Displacement of polymer particles and silica particles under  $T = 50 \text{ s}$ ,  $I = 0.4 \text{ A}$

For the first experiment, the displacement of all polymer and all silica particles were counted. Here one cycle of particle movement is shown in fig 5.13. The

experimental results for all big polymer particle displacements in x direction are shown in fig 5.14. We found that polymer particles have a total of 7 steps ( $+L$ , 20  $\mu\text{m}$ ) of displacement for 26 of individual cycles.

As we have discussed in section 5.2, the Gaussian probability distribution is determined by diffusion time for certain buffer and particle size. For the second experiment, a period of 63 s and a current of 0.4 A were tested. For the longer period, the diffusion time of the silica particles will be increased while for polymer particles the diffusion time should be almost the same. The reason is because polymer particles can fully cross the ratchet channel and experiencing the same magnetic force. In this experiment, the mean displacements were measured to be 0.17 L/cycle and  $-0.05$  L/cycle for polymer and silica particles respectively (see fig 5.15).

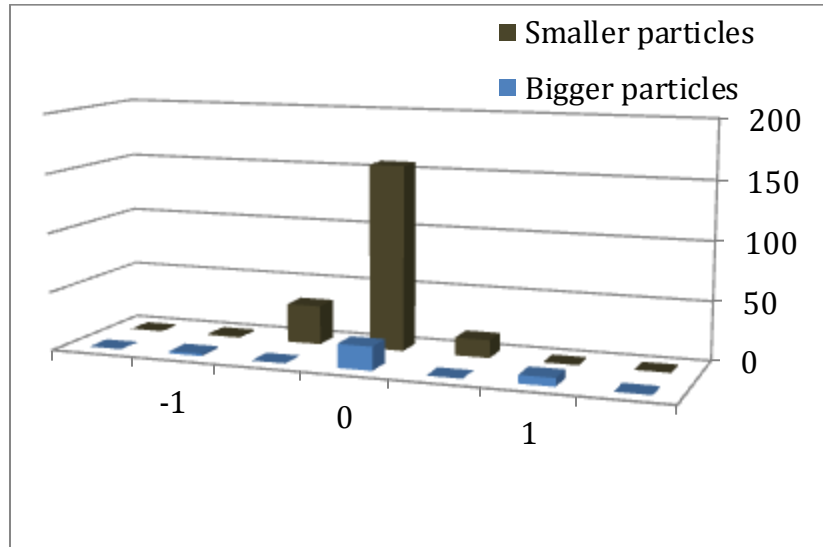


Figure 5.15 Displacement of polymer and silica particles under  $T = 63$  s,  $I = 0.4$  A

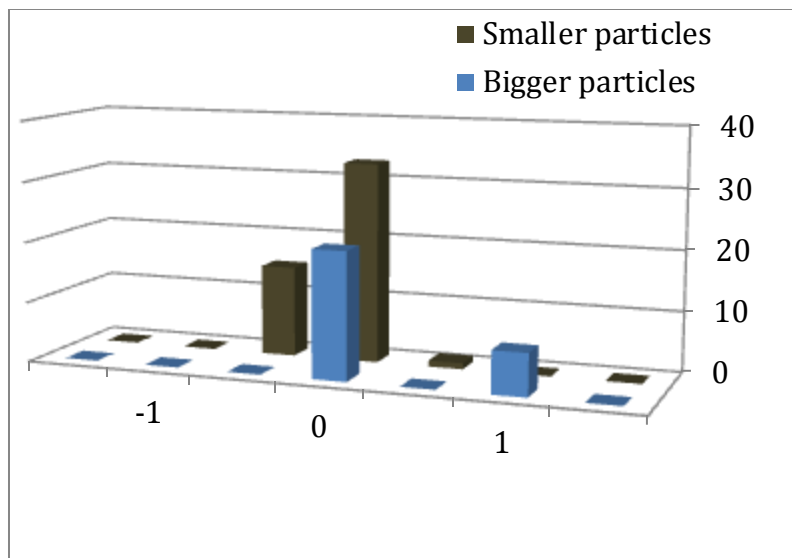


Figure 5. 16 Displacement of polymer and silica particles under  $T = 50$  s,  $I = 0.5$  A

In the third experiment, a period of 50 s and current of 0.5 A were used. With a larger current, the magnetic force will also increase (see equation 5.11). The moving speeds in y direction were measured to be approximately 4.4  $\mu\text{m/s}$  and 2.6  $\mu\text{m/s}$  for the polymer and silica particles respectively. Here, we observed that diffusion time was smaller for polymer beads compare to the current of 0.4 A. The mean displacements were calculated to be 0.3 L/cycle and -0.13 L/cycle for polymer and silica particles respectively. Figure 5.16 shows the displacement of polymer and silica particles.

In the last experiment, a period of 63 s and a current of 0.5 A were tested. Compared to first experiment, the polymer and silica particles have a shorter and longer diffusion time respectively. Results show that the polymer particle has a mean displacement of 0.73 L/step and the silica particle have a mean displacement of -0.05 L/cycle. The mean displacement for polymer particles is

quite different from previous three experiments. We found it is caused by a very small positive fluid drift during the experiment.

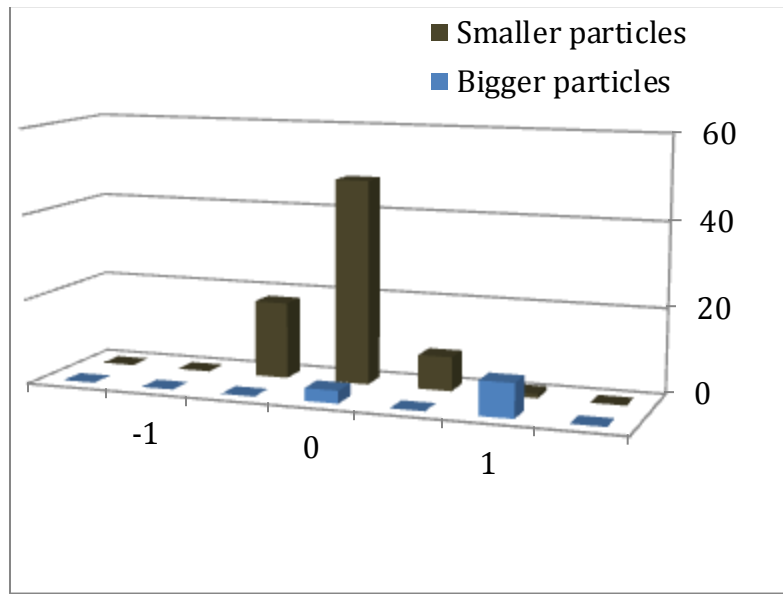


Figure 5. 17 Displacement of polymer and silica particles under  $T = 63$  s,  $I = 0.5$  A

Apart from the above four experiments, few more experiments were tested under different conditions. Fig 5.18 shows a summary of mean displacement for different experiment parameters with 90% confidence level. The confident level here means that with 90% confidence of the true population mean is in this interval. Number 2 and 4 are two independent tests under the same experimental conditions. The mean displacements for polymer particles show close results which are 0.15 L/cycle and 0.17 L/cycle respectively. While for silica particles, the results are a little bit different from each other but match within the error (-0.15L/cycle, -0.05L/cycle). The mismatch is caused by different interaction of silica particles with the smaller sawtooth. A more elaborate discussion will be

given later. Number 7 is another experiment using silica for both small and big particles ( $1.51 \mu\text{m}$ ,  $2.47 \mu\text{m}$ ).

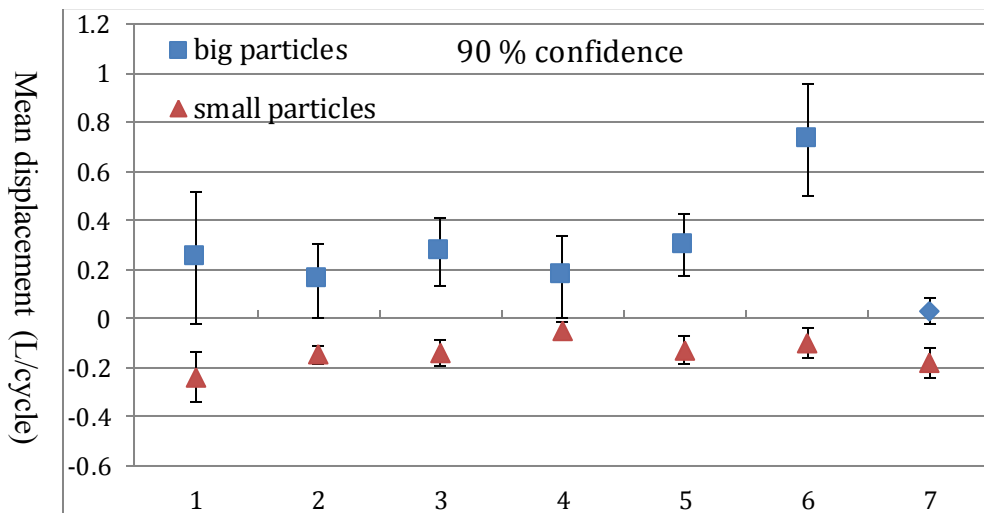


Figure 5.18 Summary of mean displacement under different experiment conditions, from left to right (current, period): (0.34 A, 83 s); (0.4 A, 63 s); (0.4 A, 50 s); (0.4 A, 63 s); (0.5 A, 50 s); (0.5 A, 63 s); (0.5 A, 63 s)

According to equation 5.3 and 5.8, the mean displacement can be theoretically calculated if we know the diffusion time and diffusion coefficient. The diffusion coefficients for polymer and silica particles are  $0.165 \mu\text{m}^2/\text{s}$  and  $0.286 \mu\text{m}^2/\text{s}$  respectively ( $20^\circ\text{C}$ , water). Here the diffusion time is different from the time period. The value was measured for an average value in each experiment for polymer and silica particles respectively. An integration of equation 5.8 will give the result of diffusion speed. Fig 5.19 shows a comparison of experimental and theoretical values.

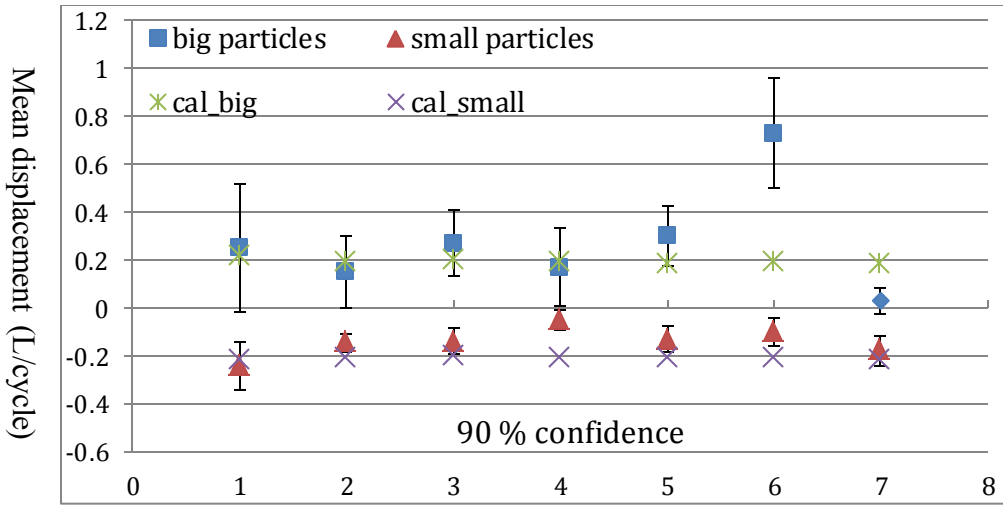


Figure 5.19 Comparison of the mean displacement between experimental results and calculated values

Results show that the calculated results are close or within the estimated confidence range of our experimental results for most of the experiments. The mismatch for some of the results (number 4 for silica particle or number 6 and 7 for polymer and silica particle respectively) is caused by the following reasons. First reason is we found a very small fluid drift during some of the experiments (number 6 experiment). The drift of fluid can enhance or reduce the ratchet separation effect. Some of our fluid drift results will be discussed later. Another reason is the movement of silica particles were largely affected by the sidewall of small sawtooth. When a positive magnetic force is applied, silica particles were driven toward positive direction. The particle tends to slide along the small sawtooth firstly, see fig 5.20b. The probability distribution will shift in x direction which will largely affect the mean displacement.

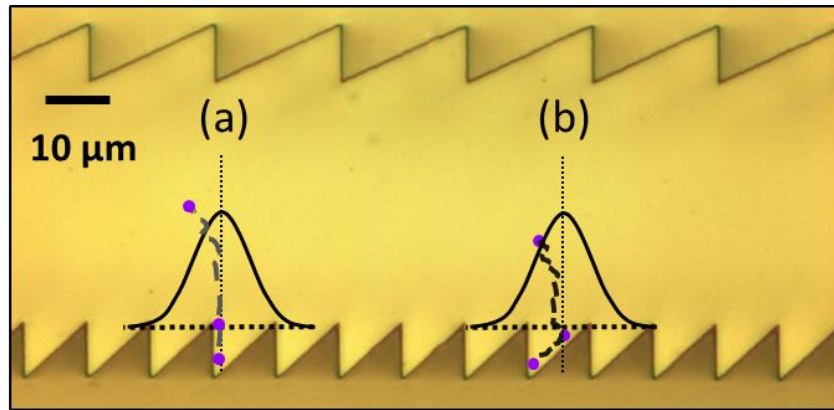


Figure 5. 20 (a) Probability distribution of silica particle without the affection of sawtooth, (b) Probability distribution of silica particle slide along the sawtooth

During some of the experiments, the fluid has a small drift in x direction. The drift here we discussed is relatively big compared to previous experiment, see fig 5.19 (number 6 experiment). For a positive fluid drift, both small and big particles can have a positive displacement, see fig 5.21 (number 1 experiment). Results show that the mean displacement speeds for those two types of particles are also different. The case is similar for negative fluid drift (experiment 2, 3 and 4, fig. 5.21).

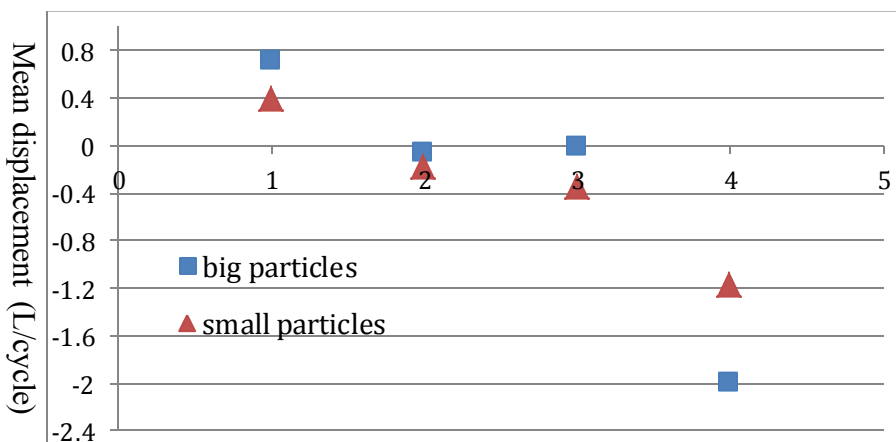


Figure 5. 21 Mean displacement of silica and polymer particles under a fluid drift under conditions (current, period): (0.4 A, 63 s); (0.4 A, 50 s); (0.4 A, 66 s); (0.4 A, 63 s)

## 5.7 Summary and comparison of ratchet separation

Here we have demonstrated a compacted ratchet separator and used it for particle separation. A comparison with the gravity based particle separator is shown in Table 5.1. The result shows that it is more than 10 times faster than the gravity separator due to the smaller channel dimension and larger Brownian motion. The particles we separated here are almost half of the size compared with gravity separation. What is more, the gravity separation is not compatible with small/light particles. Magnetic force estimation from equation 5.11 shows that the force is related to the volume of particle and the cubic distance to the electrode. So we propose here that a 3 time smaller design using magnetic force is realizable in future for sub-micron particle separation. The separation time is also very promising to be around 20 min according to a downscaled estimation [91].

Table 5. 1 Comparison of gravity and magnetic force based separation

	Gravity	Magnetic force
Time	26 hours	2 hours
Chip dimension	0.12 mm <sup>2</sup>	0.08 mm <sup>2</sup>
Particles separated	4.3 μm, 3 μm	2.6 μm, 1.51 μm

Compared with other types of microfluidic based separation techniques, such as pinched flow fractionation (PFF), inertial spiral microchannels and deterministic lateral displacement (DLD), Brownian separator has strong advantage in small total chip dimension [196, 197, 198]. While the Brownian based separation didn't seem very attractive for micro particle separation in terms of separation time and

throughput. When the size range goes down to sub-micron and Brownian motion starts to be dominant, our device is expected to show much higher efficiency.

## **Chapter 6. Conclusion and future work**

In this PhD thesis, we studied the fabrication of different molds by proton beam writing (PBW) for PDMS soft lithography and PMMA nano imprint lithography.

We have successfully fabricated three different types of molds and applied for nanofluidic applications. All of those molds show very high resolution, below 100 nm have been achieved in our work. Resist mold featuring micro/nano lines were successfully fabricated with HSQ and SU-8 resists. Straight and cross nanolines with different dimension were achieved. The smallest straight nanolines that were achieved is around 90 nm × 220 nm (width × height) with XR1541 resist. Cross nanolines with a dimension of 150 nm × 250 nm (with a thickness of 220 nm) were fabricated and tested for DNA analysis. By applying these molds with PDMS soft lithography, functional fluidic chip can be easily fabricated with low cost. The PDMS fluidic chips were used for single molecule study. DNA molecules compaction and de-compaction within the 250 nm × 220 nm (width × depth) channels were observed by flushing protamine and high concentration NaCl solutions respectively. This nano technology allows us to manipulate and linearize DNA molecule in an equilibrium conformation. The interaction of DNA molecules with protamine and salt were successfully investigated. This will gain a better understanding of the behavior DNA molecules during spermatogenesis process.

Furthermore, high resolution OrmoStamp molds were fabricated successfully with different resists. HSQ gives the best result among all of them with dimension as small as 30 nm. The OrmoStamp structures fabricated from the HSQ resist feature

an aspect ratio up to 7. A new SML resist was optimized for PBW with dimension of 60 nm, and it has great potential for Ni mold fabrication in combination with PBW since it is a positive resist. The 2<sup>nd</sup> OrmoStamp copy was fabricated successfully using the 1<sup>st</sup> OrmoStamp copy with the help of a Teflon coating. This gives more flexibility in PBW to use either positive or negative resist for desired nanostructures. Apart from this, the 1<sup>st</sup> generation OrmoStamp can be reused to copy OrmoStamp structures. This is very useful for new mold fabrication without the need of PBW and UV lithography. PMMA imprinting test with OrmoStamp mold was carried out successfully. Results show that PMMA nanochannels with a dimension of 250 nm × 270 nm were imprinted with high accuracy. OrmoStamp mold fabrication and test with PMMA imprinting give us another choice for thermal NIL mold beside nickel mold. What is more, it is easier to fabricate an OrmoStamp mold with various resists than nickel mold. Because the sacrificing resist need to be carefully chosen for nickel mold fabrication.

The PMMA bonding process was optimized with previous imprinted channel. Optical imaging shows that the nanochannels were bonded successfully. PMMA has a higher Young's modulus compared with PDMS material and this allows us to fabricate a low cost nanochannel at sub 50 nm dimension. In the future, the channel dimension needs to be further characterized with FIB milling and sub 50 nm PMMA nanochannels will be optimized. It should be pointed out that PMMA is a hydrophobic polymer. Injection of fluids into the nanochannel is a major problem for nanofluidic applications. In our experiments, the PMMA sample was treated with plasma to make the channel hydrophilic. One disadvantage for

plasma treatment is the fact that the hydrophilic property won't last for long time (typically about an hour). So, extra chemical modification of the PMMA surface is required to make it hydrophilic in the future.

Nickel molds were also fabricated by PBW with ma-N 2410 photoresist in combination with electroplating. After Ni plating and re-electroplating, we get a nickel stamp with almost the same fidelity ( $600\text{nm} \times 600\text{nm}$ ) as the original resist mold. PMMA lab-on-chip devices were imprinted with the nickel mold and bonded with another PMMA film for DNA test. The result shows that DNA molecules can be injected into the nanochannels successfully. A smaller nickel mold on ma-N 2401 was also fabricated by electroplating. It was found that ma-N 2401 resist cannot be fully removed by acetone or remover. In the future, other resists (PMMA and SML) will be tested for sub 50 nm nickel mold fabrication.

In the present contribution, the fluidic channel used for DNA analysis are in the range of  $150\text{ nm} \sim 700\text{ nm}$  which is larger than typical persistence length of DNA molecules [19]. Success in OrmoStamp mold, nickel mold and PMMA nanochannel fabrication makes it possible in the future for high-resolution structure manufacturing. An outlook of sub 50 nm PMMA channel is realistic in combination with all these techniques. At the sub 50 nm size ranges, the channel diameter is smaller than the persistence length of DNA molecules. A DNA molecule will be aligned along the channel and takes a highly extended conformation [199]. Applications can be used for large scale genome mapping or even single strand DNA sequencing in the future [37, 200].

Apart from the nanochannel fabrication, we also studied a ratchet structure used for particle separation. The ratchet structure was fabricated successfully and tested for particle separation. Separation tests show that particles with different size ( $2.6 \mu\text{m}$ ,  $1.5 \mu\text{m}$ ) diffuse in opposite directions as predicted. The ratchet design shows very compact form ( $320 \mu\text{m} \times 280 \mu\text{m}$ ), which can be easily integrated to LOC device. Two micro electrodes were integrated with this ratchet channel successfully that can carry a current as much as  $0.5\text{ A}$ , and guarantee a relatively strong magnetic force. It should be noted that the ratchet device in its current form is not suitable for large amount of sample separation. To make it a workable separation device in the future, new inlet/outlet channel need to be properly designed, see one of our idea in fig 6.1. Outlet 1 will be used for collecting small particle and outlet 2 for big particle. The separated particles can be driven out through outlets by injecting new particle from inlet.

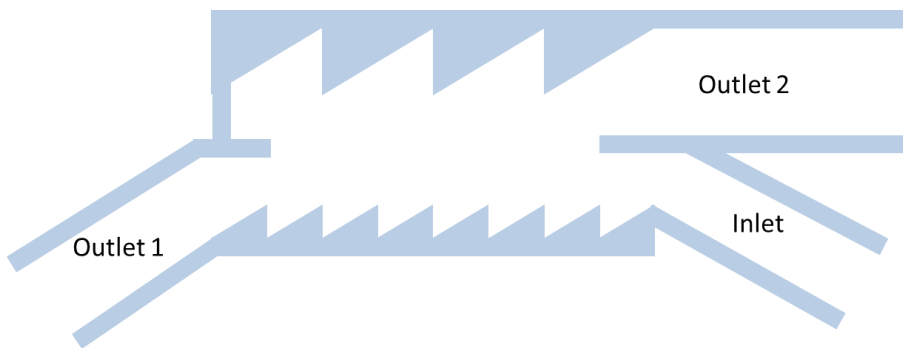


Figure 6.1 Illustration of the new design for continuous separation

We will also try to apply this design for biomolecules separation such as DNA, proteins or cells. One possible way to separate is through attaching biomolecules to those particles [201]. The magnetic particles for binding are widely available

from different companies such as Dynal, Bangs laboratories, and Polysciences. Another possible way to drive the nonmagnetic biomolecules is through the using of paramagnetic buffer ( $MnCl_2$ ,  $Gd \cdot DTPA$ ). Report shows that driving of cells (human blood cell, yeast, and algae) has been realized in various paramagnetic buffer [202, 203].

## Bibliography

---

- [1] Feynman, R. P., There's Plenty of Room at the bottom, *Reinhold Publishing, New York*, 1961
- [2] Varadan V. K., Jiang Xiaoning, Varadan V. V. Microstereolithography and other fabrication techniques for 3D MEMS, *John Wiley & Sons*, 2001
- [3] S. Nakagawa, S. Shoji and M. Esashi, *Micro System Technology, Springer-Verlag, Berlin*, **90** (1990) 799
- [4] E.W.K. Young, E. Berthier and D.J. Beebe, *Analytical Chememistry* **85** (2013) 44-49
- [5] L.M. Fu, J.C. Leong, C.F. Lin, C.H. Tai, and C.H. Tsai, *Biomedical Microdevices* **3** (2007) 405-412
- [6] H. Kimura, T. Yamamoto, H. Sakai, Y. Sakai and T. Fujii, *Lab on a Chip* **8** (2008) 741-746
- [7] E. Berthier, J. Warrick, and B. Casavant, *Lab on a Chip* **11** (2011) 2060-2065
- [8] K.T. Kotz and Mehmet Toner, *et al.*, *Nature Medicine* **16** (2010) 1042-1047
- [9] Lifeng Kang, Bong Geun Chung, Robert Langer, and Ali Khademhosseini, *Drug Discovery Today* **13** (2008) 1-13
- [10] Jan C. T. Eijkel, Albert van den Berg, *Microfluid Nanofluid*, **1** (2005) 249-267
- [11] Figeys D. and Pinto D., *Anal. Chem.* **72A** (2000) 330-335
- [12] Young E.W.K., Berthier E. and Beebe D.J., *Anal. Chem.* **85**, (2013) 44-49
- [13] Kimura H., Yamamoto T., Sakai H., Sakai Y. and Fujii T. *Lab on a Chip* **8** (2008) 741-746
- [14] Berthier E., Warrick J., and Casavant B. *Lab on a Chip* **11** (2011) 2060-2065
- [15] Kotz K.T. *et al.* *Nature Med.* **16** (2010) 1042-1047
- [16] Patrick Abgrall, Nam Trung Nguyen. *Ana. Chem.* **80** (2008): 2326-2341.
- [17] Fu L. M. , Leong J. C. , Lin C. F. Tai C. H., and Tsai C.H., *Biomed Microdevices* **3** (2007) 405-412
- [18] Lifeng Kang, Bong Geun Chung, Robert Langer, and Ali Khademhosseini. *Drug Discovery Today* **13** (2008) 1-13

- 
- [19] Ce Zhang, Fang Zhang, Jeroen A. van Kan, and Johan R.C. van der Maarel. *The Journal of Chemical Physics* **128** (2008) 225109
- [20] Tian, W.-C. and E. Finehout. *Introduction to Microfluidics*. 2009.
- [21] Soon-Eng Ong, Sam Zhang, Hejun Du, Yongqing Fu. *Frontiers in Bioscience* **13** (2008) 2757-2773.
- [22] Frank White. *Viscous Fluid Flow*. Boston: McGraw-Hill. 2nd ed, 1991.
- [23] J.P. Brody, P. Yager, R. E. Goldstein, and R. H. Austin., *Biophysics Journal* **71** (1996) 3430–3441.
- [24] Brody J, Yager P, *Sens. Actuators A* **A58** (1997) 13-18
- [25] Hatch A, Kamholz A, Hawkin K, Munson M, Schilling E, Bernhard H and Paul Yager, *Nat. Biotechnol.* **19** (2001) 461-465
- [26] Brody J, Yager P, Goldstein R, Austin R. *Biophys. J.* **71** (1996) 3430-3441
- [27] David J. Beebe, Glennys A. Mensing, and Glenn M. Walker, *Annu. Rev. Biomed. Eng.* **4** (2002) 261-286
- [28] A. D. Stroock, S. K. W. Dertinger, A. Ajdari, I. Mezic, H. A. Stone, and G. M. Whitesides, *Science*, **295** (2002) 647-651
- [29] E. Samson, J. Marchand, and K. A. Snyder, *Materials and Structures*, **36** (2003) 156-165
- [30] G.K. Batchelor, An introduction to fluid dynamics, *Cambridge University Press* (1967)
- [31] George M. Whitesides, *Nature*, **442** (2006) 368-373
- [32] Angela D. Norbeck, Matthew E. Monroe, Joshua N. Adkins, and Richard D. Smith, *J Am Soc Mass Spectrom.*, **8** (2005) 1239-1249
- [33] Curtis D. Chin, Vincent Linder and Samuel K. Sia, *Lab on a Chip*, **12** (2012) 2118-2134
- [34] D.J. Lockhart, and E.A. Winzeler, *Nature*, **405** (2000):827–836
- [35] Hochmuth R.M., *J. Biomech*, **33** (2000) 15-22
- [36] Bambardekar K, Dharmadhikari A.K., Dharmadhikari J.A., Mathur D and Sharma S, *J. Biomed. Opt.*, **13** (2008) 064021

- 
- [37] Ce Zhang, Armando H. G., Kai Jiang, Zongying Gong, Durgarao G., Siow Yee Ng, P.P. Malar, J.A. van Kan, Liang Dai, P.S. Doyle, Renko de Vries and J.R.C van der Maarel, *Nucleic Acids Research*, **41** (2013) e189
- [38] Hoyong Yun, Kisoo Kim, and Wongu Lee, *Biofabrication*, **5** (2013) 022001
- [39] Jonas O, Tegenfeldt, Christelle Prinz, Han Cao, Richard L. Huang, Robert H, Austin, Stephen Y, Chou Edward C. Cox, James C. Sturm; *Anal. Bioanal. Chem.* **378** (2004): 1678–1692
- [40] Wang X, Chen S, Kong M, Wang Z, Costa KD, Li R A, Sun D, *Lab Chip*,**11** (2011) 3656
- [41] Miltenyi S, Muller W, Weichel W, and Radbruch A, *Cytometry* **11** (1990): 231-8
- [42] Vahey M and Voldman J, *Anal. Chem.* **80** (2008) 3135-43
- [43] An J, Lee J, Lee S H, Park Jand Kim B, *Anal. Bioanal. Chem.* **394** (2009): 801-9
- [44] Eriksson E, Enger J, Nordlander B, Erjavec N, Ramser K, Goksor M, Hohmann S, Nystrom T and Hanstorp D, *Lab Chip*, **7** (2007):771–6
- [45] Jonas O, Tegenfeldt, Christelle Prinz, Han Cao, Richard L. Huang, Robert H, Austin, Stephen Y, Chou Edward C. Cox, James C. Sturm; *Anal Bioanal Chem* **378** (2004): 1678–1692
- [46] Dekker C., *Nature nanotechnology*, **2** ( 2007): 209-215
- [47] ZhiJian Jia, Qun Fang, and Zhao lun Fang, *Anal. Chem.* **76** (2004) 5597-5602
- [48] Sayah A., Solignac D., Cueni T., and Gijs M.A.M, *Sens. Actuators A* **84** (2000) 103
- [49] Jang W., Choi C., Lee M., Jun C., and Kim Y., *Journal of Micromechanics and Microengineering* **12** (2002) 297-306
- [50] Han Cao, Zhangning Yu, Jian Wang, Jonas O. Tegenfeldt, Robert H. Austin, Erli Chen, Wei Wu, and Stephen Y. Chou, *Applied Physics Letters*, **81**, 174 (2002)
- [51] QiangFei Xia, Keith J. Morton, Robert H. Austin, and Stephen Y.C., *Nano Letters* **8** (2008) 3830-3833

- 
- [52] Younan Xia and Grerge M. Whitesides, *Annu. Rev. Mater. Sci.* **28**, (1998) 153-184
- [53] Hongkai Wu, Bo Huang and Richard N. Zare, *Lab on a chip*, **5** (2005) 1393-1398
- [54] James Friend and Leslie Yeo, *Biomicrofluidics* **2** (2010) 026502
- [55] Piruska A., Nikcevic L., Lee S. H., Ahn C. Heineman W. R., Limbach P. A., and Seliskar C. J. , *Lab on a Chip* **5** (2005) 1348-1354
- [56] Marc A. Unger et al, *Science*, **288** (2000): 113
- [ 57 ] J.A. van Kan, C. Zhang, P. Malar and J.R.C. van der Maarel, *Biomicrofluidics*, **6** (2012) 036502-1
- [58] Andrea Cattoni, E. Cambril, D. Decanini, G. Faini, and A.M. Haghiri-Gosnet, *Microelectronic Engineering*, **87** (2010) 1015-1018
- [59] Chia-Wen Tsao, and Don L. DeVoe, *Microfluid Nanofluid*, **6** (2009): 1–16
- [60] J.A. van Kan, P.G. Shao, Y.H. Wang, *Microsystem Technologies*, **17** (2011) 1519-1527
- [61]C. Lu, L.J. Lee, and Y.J. Juang, *Electrophoresis*, **29** (2008): 1407–1414
- [62] Dang F, Shinohara S, Tabata O, Yamaoka Y, Kurokawa M, Shinohara Y, Ishikawa M, and Baba Y, *Lab on a chip*, **4** (2005) 472-478
- [63] Lu C, Lee LJ, and Juang YJ, *Electrophoresis*, **7** (2008) 1404-1414
- [64] Klank H, Kutter JP, and Geschke O, *Lab on a Chip*, **2** (2002): 242–246
- [65] Huang F-C, Chen Y-F, and Lee G-B, *Electrophoresis* **28** (2007):1130–1137
- [66] Li Y, Buch JS, Rosenberger F, DeVoe DL, and Lee CS, *Anal. Chem.*, **76** (2004) 742–748
- [67] Laurie Brown, Terry Koerner, J. Hugh Horton and Richard D. Oleschuk, *Lab on a Chip* **6** (2006) 66-73
- [68] Park DSW, Hupert ML, Witek MA, You BH, Datta P, Guy J, Lee JB, Soper SA, Nikitopoulos DE, Murphy MC (2008)
- [69] Chen ZF, Gao YH, Su RG, Li CW, and Lin JM, *Electrophoresis*, **24** (2003): 3246–3252

- 
- [70] Arroyo MT, Fernandez LJ, Agirregabiria M, Ibanez N, Aurrekoetxea J, and Blanco FJ, *J Micromech Microeng*, **17** (2007) 1289–1298
- [71] Riegger L, Grumann M, Steigert J, Lutz S, Steinert CP, Mueller C, Viertel J, Prucker O, Ruhe J, Zengerle R, Ducree J, *Biomed Microdevices* **9** (2007): 795–799
- [72] Sun Y, Kwok YC, and Nguyen NT, *J Micromech Microeng*, **8** (2006) 1681–1688
- [73] Lasse H Thamdrup *et al*, *Nanotechnology* **19**, 125301, (2008)
- [74] P. G. Shao, J.A. van Kan, L.P. Wang, K. Ansari, A.A. Bettoli, F. Watt, *Applied Physics Letters* **88** (2006) 093515
- [75] Xiaoqiao Hu, Qiaohong he, Xiangbo Zhang and Hengwu Chen, *Microfluid Nanofluid*, **10** (2011) 1223-1232
- [76] Eddings MA, Johnson MA, and Gale BK, *J Micromech Microeng*, **18** (2008) 067001
- [77] Bo-lennart Johansson, Anders Larsson, Anette Ocklind, and Ake Ohrlund, *Journal of Applied Polymer Science*, **86** (2002) 2618-2625
- [78] Tsao CW, Hromada L, Liu J, Kumar P, DeVoe DL, *Lab Chip* **7** (2007): 499–505
- [79] Abgrall P, Low LN, Nguyen NT, *Lab on a Chip*, **7** (2007):520–522
- [80] Ahn CH, Choi JW, Beaucage G, Nevin JH, Lee JB, Puntambekar A, and Lee JY, *Proc IEEE*, **92** (2004) 154-173
- [81] Wang YR, Chen HW, He QH, Soper SA, *Electrophoresis*, **29** (2008) 1881–1888
- [82] Bhattacharyya A and Klapperich CM, *Lab Chip*, **7** (2007): 876-882
- [83] Truckenmuller R, Henzi P, Herrmann D, Saile V, Schomburg WK, *Microsystem Technologies*, **10** (2004): 372-374
- [84] Jean Louis Viovy, *Rev. Mod. Phys.*, **72** (2000) 3
- [85] Bachvaroff R, and McMaster PRB, *Science*, **143** (1964) 1177-1179
- [86] Richards EG, Coll JA, and Gratzer WB, *Anal Biochem*, **12** (1965) 452-471
- [87] Aaij C, and Borst P, *Biochim Biophys Acta*, **269** (1972) 192-200

- 
- [88] L. R. Huang, J. O. Tegenfeldt, J. J. Kraeft, J. C. Sturm, R. H. Austin and E. C. Cox, *Nat. Biotechnol.*, **20** (2002) 1048
- [89] J. Rousselet, L. Salome, A. Ajdari, and J. Prost, *Nature*, **370** (1994) 446
- [90] Chou CF, Bakajin O, Turner SWP et al, *Proc Natl Acad Sci USA*, **96** (1999) 13762–13765
- [91] Simon Verleger, Andrej Grimm, Christian Kreuter, Huei Ming Tan, Jeroen A. van Kan, Artur Erbe, Elke Scheera and Johan R. C. van der Maarel, *Lab on a Chip*, **12** (2012) 1238-1241
- [92] J. A. van Kan, P. Malar, and Armin Baysic de Vera, *Review of scientific instruments* **83** (2012) 02B902
- [93] J. A. van Kan, A.A Bettoli, K. Ansari, E.J. Teo, T.C. Sum and F. Watt, *International Journal Nanotechnology* **1** (2004) 464
- [94] M. Rothschild, T.M. Bloomstein, N. Efremow Jr., T.H. Fedynyshyn, M. Fritze, I. Pottebaum, and M. Switkes, *MRS bulletin*, **30** (2005) 942-946
- [95] Joseph C. Weingartner, B.T. Draine, David K. Barr, *Astrophysical Journal*, **645** (2006) 1188-1197
- [96] Jain, K. Excimer Laser Lithography. *SPIE press, Bellingham, WA*, 1990
- [97] La Fontaine B., *Lasers and Moore's Law*, SPIE Professional, 2010 p. 20
- [98] A. Grenville, V. Liberman, M. Rothschild, J.H.C. Sedlacek, R.H. French, R.C. Wheland, X. Zhang, and J. Gordon, *Proc, SPIE* **4691** (2002) 1644
- [99] R. French, R.C. Wheland, W. Qiu, M.F. Lemon G.S. Blackman, E. Zhang, J. Gordon, V. Liberman, A. Grenville, R.R. Kunz, and M. Rothschild, *Proc. SPIE* **4691** (2000) 459
- [100] J.H. Burnett, Z.H. Levine, *Phys. Rev. B*, **64** (2001)
- [101] J.H. Burnett, and S.G. Kaplan, *J. Microlith. Microfab. Microsyst.*, **3** (2004) 68
- [102] J. Yang, B. Cord, K. Berggren, J. Klingfus, S. Nam, K. Kim and M. Rooks, *Journal of Vacuum Science & Technology B*, **27** (2009) 2622-2627
- [103] Joan Vila-Comamala, Sergey Gorelick, Vitaliy A Guzenko, Elina Farm, Mikko Ritala, and Christian David, *Nanotechnology*, **21** (2010) 285305

- 
- [104] S. Lewis, D. Jeanmaire, V. Haynes, P. McGovern and L. Piccirillo, *NSTI-Nanotech*, **2** (2010) 195-198
  - [105] Raith GmbH, Dortmund, [www.raith.com](http://www.raith.com)
  - [106] Vistec electron beam GmbH, Jena, [www.vistec-semi.com](http://www.vistec-semi.com)
  - [107] C. Udalagama, A. A. Bettoli, and F. Watt, *Physical Review B*, **80** (2009) 224107
  - [108] Lloyd R. Harriott, *J. Vac. Sci. Technol. B*, **15** (1997) 2130-2135
  - [109] H. C. Pfeiffer, *Proc. SPIE*, **1671** (1992) 100-110
  - [110] J. A. Liddle, M. I. Blakey, C.S. Knurek, M. M. Mkrtchyan, A. E. Novembre, L. Ocola, T. Saunder and W. K. Waskiewicz, *Microelectronic Engineering*, **41/42** (1998) 155-158
  - [111] Ampere A. Tseng, Kuan Chen, Chii D. Chen, and Kung J. Ma, *IEEE Transactions on Electronics Packaging Manufacturing*, **26** (2003) 141-149
  - [112] Akio Yamada and Yoshihisa Ooae, *Proc. SPIE*, **7823** (2010) 78231H-1
  - [113] Elmar Platzgummer, *Proc. SPIE*, **7637** (2010) 763703
  - [114] M. J. Wieland, H. Derks, H. Gupta, T. van de Peut, F. M. Postma, A. H. V. van Veen, Y. Zhang, *Proc. SPIE Vol 7673* (2010) 76371Z-1
  - [115] Burn J. Lin, *Proc. SPIE*, **8323** (2012) 832302-1
  - [116] Christof Klein, Jan Klikovits, Hans Loeschner, and Elmar Platzgummer, *Proc. SPIE*, **7970** (2011) 797011
  - [117] Steve Reyntjens and Robert Puers, *Journal of Micromechanics and microengineering*, **01** (2001) 18940-0
  - [118] P. R. Munroe, *Materials Characterization*, **60** (2009) 2-13
  - [119] Orloff J, Utlaut L, Swanson M. W. High resolution focused ion beams, *Kluwer Academic Publishers*, 2003
  - [120] R. L. Kubena, J. W. Ward, F. P. Stratton, R. J. Joyce and G. M. Atkinson, *J. Vac. Sci Technol.*, **9** (1991): 3079
  - [121] V. Sidorkin, E. van Veldhoven, E. vander Drift, P. Alkemade, H. Salemink, D. Mass, *J. Vac. Sci. Technol.*, **27** (2009): 18-20
  - [122] Abramo et al, *Int. Symp.*, **20** (1994) 439

- 
- [123] B. I. Prentitzer et al., *Microsc. Microanal.*, **6** (2000) 502
- [124] F. Watt, A. A. Bettoli, J. A. Van kan , E. J. Teo, and M. B. H. Breese, *International Journal of Nanoscience*, **4** (2005): 269-286
- [125] Yound R.J., Cleaver J.R.A., and Ahmed H., *J. Vac. Sci. Technol. B*, **11** (1993) 234-241
- [126] Tao Tao, William Wilkinson, and John Melngailis, *J. Vac. Sci. Technol. B*, **9** (1991) 162
- [127] Matsui S, et al. *J. Vac. Sci. Technol.*, **4** (1986): 845
- [128] H. Ryssel, K. Haberger, and H. Kranz. *J. Vac. Sci. Technol.*, **19** (1981) 1358
- [129] J. A. van Kan, A. A. Bettoli and Frank Watt. *Nano Letters*, **6** (2006) 579-582
- [130] Ziegler J.F. The Stopping and Range of Ions in Matter, *Oxford*, (1977-1985) 2-6
- [131] C.N.B. Udalagama, A.A. Bettoli and F. Watt, *Nuclear Instruments and Methods in Physics Research B*, **260** (2007) 384-389
- [132] J. A. van Kan, Andrew A. Bettoli, Kambiz Ansari, Ee Jin Teo, Tze Chien Sum and Frank Watt, *Int. J. Nanotechnol.*, **1** (2004): 464
- [133] C. Udalagama, A. A. Bettoli, and F. Watt, *Physical Review B*, **80**, (2009) 224107
- [134] J. A. van Kan, J.L. Sanchez, B. Xu, T. Osipowicz, F. Watt, *Nuclear Instruments and Methods in Physics Research B*, **148** (1999) 1085-1089
- [135] S. J. Moss and A. ledwith, *Chemistry of the Semiconductor Industry* (1987) Page 181
- [136] Huigao Duan, Donald Winston, Joel K. W. Yang, Bryan M. cord, Vitor R. Manfrinato and Karl K. Berggren, *J. Vac. Sci. Technol. B*, **28** (2010): C6C58
- [137] J. A. van Kan, A.A. Bettoli and F. Watt, *Applied Physics Letters*, **83** (2003) 1629-1631
- [138] F. Liu, Y, Yao, J.A. van Kan, *Nuclear Instruments & Methods in Physics Research B*, DOI 10.1016/j.nimb.2015.01.067.

- 
- [139] S. Bolhuis, J.A. van Kan, F. Watt, *Nuclear Instruments and Methods in Physics Research Section B*, **267** (2009) 2302-2305
- [140] Vitor R. Manfrinato, Joel K. W. Yang, Donald Winston, Bryan M. Cord, and Karl K. Berggren, *J. Vac. Sci. Technol. B*, **28** (2010) C6H11
- [141] A.E. Grigorescu, M.C. van der Krog, C.W. Hagen and P. Kruit, *Microelectronic Engineering*, **84** (2007) 822-824
- [142] C.L. Frye, and W.T. Collins, *Journal of the American Chemical Society*, **92** (1970) 5586-5588.
- [143] J. A. van Kan, A.A. Bettoli, F. Watt, *Nucl. Instr. and Meth. B*, **260** (2007) 353
- [144] J. A. van Kan, F. Zhang, C. Zhang, A. A. Bettoli, and F. Watt, *Nuclear Instruments and Methods in Physics Research Section B*, **266** (2008) 1676-1679
- [145] Y.H. Wang, P. Malar, J.A. van Kan, *Microsystem Technologies*, 2014
- [146] [http://www.microchem.com/PDFs\\_MRT/ma-N%202400%20overview.pdf](http://www.microchem.com/PDFs_MRT/ma-N%202400%20overview.pdf)
- [147] <http://www.emresist.com/technology.html>
- [148] Gorelick S, Guzenko VA, Vila-Comamala J, and David C, *Nanotechnology*, **21** (2010) 295303
- [149] J. A. van Kan, P. Malar, Y.H. Wang, *Applied Surface Science*, **310** (2014) 100-111
- [150] Khalil Khanafer, Ambroise Duprey, Marty Schlicht, Ramon Berguer, *Biomed Microdevices*, **11** (2009) 503-508
- [151] [http://www.microresist.de/produkte/ormocer/pdf/ormostamp\\_080821\\_en.pdf](http://www.microresist.de/produkte/ormocer/pdf/ormostamp_080821_en.pdf)
- [152] Iren Fernandez-Cuesta, Anna Laura Palmarelli, Xiaogan Liang, Jingyu Zhang, Scott Dhuey, Deirdre Olynick, and Stefano Cabirni, *Journal of Vacuum Science & Technology B*, **6** (2011) 1071-1023
- [153] F. Watt, J.A. van Kan, T. Osipowicz, *MRS Bulletin*, **25** (2000) 33
- [154] A.A. Bettoli, J.A. van Kan, T.C. Sum, F. Watt, *Nucl. Instr. and Meth. B* **181** (2001) 49
- [155] F. Watt, G.W. Grime, G.D. Blower, J. Takacs, *IEEE Transactions on Nuclear Science* **28** (1981)

- 
- [156] J.A. van Kan, A.A Bettoli and F. Watt, *M Jat. Res. Soc. Symp. Proc.* **777** (2003) T2.1.1
- [157] F. Watt, J. A. van Kan, I. Rajta, A. A. Bettoli, T. F. Choo, M. B. H. Breese and T. Osipowicz, *Nucl. Instrum. Methods Phys. Res. B* **210** (2003) 14-20
- [158] J.A. van Kan, P.G. Shao, P. Molter, M. Saumer, A.A. Bettoli, T. Osipowicz, and F. Watt, *Nuclear Instruments and Methods in Physics Research B*, **231** (2005) 170–175
- [159] Y. Yao, J. A. van Kan, *Nuclear Instruments & Methods in Physics Research B*, To be published. (2014)
- [160]<https://www.clean.cise.columbia.edu/images/stories/sop/muepg101.pdf>
- [161] M. Schlesinger and M. Paunovic, *Modern electroplating*, Prentice Hall, Englewood Cliffs, New Jersey, 1991
- [162] T. Saito, E. Sato, M. Matsuoka, and C. Iwakura, *Journal of Applied electrochemistry*, **28** (1998) 559-563
- [163] A.A. Bettoli, C.N.B. Udalagama, J.A. van Kan, F. Watt, *Nuclear Instruments and Methods in Physics Research Section B*, **231** (2005) 400-406
- [164] J.A. van Kan, P. G. Shao, Y. H. Wang and P. Malar, *Microsyst. Technol.*, **17** (2011) 1519–1527
- [165] Shao Peige, J.A. van Kan, Frank Watt, *Key Engineering Materials Vols.* **447** (2010) 452-455
- [166] M.C. Cheng, A.J. Nijdam, J.A. Garra, A.P. Gadre, T.W. Schneider, R.C. white, M. ParanJape, and J.F. Currie, *7<sup>th</sup> International Conference on Miniaturized Chemical and biochemical Analysis Systems*, California USA, 2003
- [167] J. A. van Kan, P. G. Shao, Y. H. Wang and P. Malar, *Microsyst. Technol.*, **17** (2011) 1519–1527
- [168] Tomi Haatainen, Paivi Majander, Tommi Riekkinen, Jouni Ahopelto *Microelectronic Engineering* **83** (2006) 948-950
- [169] Liu nan nan, Shao Peige, Shripad R. Kulkarni, Zhao Jianhong, and J. A. van Kan, *Key Engineering Materials*, **447-448** (2010) 188-192

- 
- [170] Stephen Y. Chou, Peter R. Krauss, Preston J. Renstrom, *Science*, **272** (1996) 85-87
- [171] Anthony T. Annunziato, *Nature Education*, **1** (2008) 26
- [172] Ce Zhang, Durgarao Guttula, Fan Liu, Piravi P. Malar, Siow Yee Ng, Liang Dai, Patrick S. Doyle, Jeroen A. van Kan, and Johan R. C. van der Maarel, *Soft Matter*, **40** (2013) 9593-9601
- [173] M. de Frutos, E. Raspaud, A. Leforestier, and F. Livolant, *Biophysical*, **2** (2001) 1127-1132
- [174] Ce Zhang, Pei Ge Shao, J. A. van Kan, and Johan R.C. van der Maarel, *PNAS*, **106** (2009) 16651-16656
- [175] M. J. Allen, E. M. Bradbury and R. Balhorn, *Nucleic Acids Res.*, **25** (1997) 2221-2226
- [176] Jason DeRouchey, Brandon Hoover and Donald C. Rau, *Biochemistry*, **52** (2013) 3000-3009
- [177] P. G. de Gennes, *Scaling Concepts in Polymer Physics* , Cornell University Press, *Ithaca, New York*, 1979
- [178] F.C.M.J.M. van Delft, *J. Vac. Sci. Tehcnol. B*, **20** (2002) 2932
- [179] P.G. Shao, J. A. Van Kan, L.P. Wang, K. Ansari, A.A Bettol, F. Watt, *Applied Physics Letters*, **88** (2009) 093515
- [180] K. Ansari, J. A. van Kan, A. A. Bettoli and F. Watt, *Applied Physics Letters*, **85** (2004) 476-478
- [181] Y.H. Wang, P. Malar, and J. A. van Kan, *Microsyst Technol.*, **20** (2014) 2079-2088
- [182] [www.emresist.com](http://www.emresist.com)
- [183] K. A. Mahabadi, I. Rodriguez, S. C. Haur, J. A. van Kan, A. A. Bettoli and F. Watt *J. Micromech. Microeng.*, **16** (2006) 1170
- [184] R.P. Feynman, R.B. Leighton, and M. Sands, the Feynman lectures on physics, vol. 1, Addison-Wesley, Reading, MA, 1966.
- [185] Andrej Grimm, *Separation and collective phenomena of colloidal particles in Brownian ratchets*, PhD thesis

- 
- [186] A. Ajdari, D. Mukamel, L. Peliti, and J. Prost, *Journal de Physique I*, **4** (1994) 1551
- [187] M.O. Magnasco, *Phys Rev Lett*, **71** (1993) 1477
- [188] J. Rousselet, L. Salome, A. Ajdari, and J. Prost, *Nature*, **370** (1994) 446
- [189] T.A.J. Duke and R.H. Ausin, *Phys Rev Lett*, **80** (1998) 1552
- [190] T. Deng, G.M. Whitesides, M. Radhakrishnan, G. Zabow, and M. Prentiss, *Appl. Phys. Lett.*, **78** (2001) 1775-1777
- [191] C.S. Lee, H. Lee, and R.M. Westervelt, *Appl. Phys. Lett.*, **79** (2001) 3308-3310
- [192] M.N.O. Sadiku, *Elements of Electromagnetics*, Saunders, New York, 1989
- [193] Sergey S. Shevkoplyas, Adam C. Siegel, Robert M. Westervelt, Mara G. Prentiss and George M. Whitesides, *Lab on a chip*, **7** (2007) 1294-1302
- [194] A. C. Siegel, S. S. Shevkoplyas, D. B. Weibel, D. A. Bruzewicz, A. W. Martinez and G. M. Whitesides, *Angew. Chem.-Int. Edit.*, **45** (2006) 6877-6882.
- [195] Fernando Martinez-Pedrero, Maria Tirado-Miranda, Artur Schmitt, Jose Callejas-Fernandez, *Colloids and Surfaces A*, **270-271** (2005) 317- 322
- [196] M. Yamada, M. Nakashima and M. Seki, *Anal. Chem.*, **76** (2004) 5465-5471
- [197] Sathyakumar S. K., Ali Asgar S. B., Girsh Kumar and Ian Papautsky, *Lab on a Chip*, **9** (2009) 2973-2980
- [198] L. R. Huang, E.C.Cox, R. H. Austin and J. C. Sturm, *Science*, **304** (2004) 987-990
- [199] T. Odijk, *Macromolecules*, **16** (1983) 1340
- [200] Seung Kyu Min, Woo Youn Kim, Yeonchoo Cho and Kwang S. Kim, *Nature Nanotechnology*, **6** (2011) 162-165
- [201] Nicole Pamme, *Lab on a Chip*, **6** (2006) 24-38
- [202] Hitoshi Watarai, Makoto Namba, *Journal of Chromatography A*, **961** (2002) 3-8
- [203] Adam Winkleman, KatherineL. Gudiksen, Declan Ryan, and George M. Whitesides, *Applied Physics Letters*, **85** (2004) 2410- 2413